SISSA

Scuola Internazionale Superiore di Studi Avanzati

Mathematics Area - PhD course in
Mathematical Analysis, Modelling, and Applications

Transient morphing and optimal shape design of synthetic and natural active structures

Candidate:
Dario Andrini

Advisors:
Prof. Giovanni Noselli
Prof. Alessandro Lucantonio

Academic Year 2021-22

The present dissertation, submitted by Dario Andrini under the supervision of Prof. Giovanni Noselli and Prof. Alessandro Lucantonio, is to fulfill the requirements for the degree of Philosophiæ Doctor in Mathematical Analysis, Modelling, and Applications in SISSA. According to art. 1, paragraph 4 of the SISSA Statute G.U. No. 36 published on 13.02.2012, the aforementioned degree is equivalent to the title of Research Doctorate in Mathematics (Dottore di Ricerca in Matematica).

Trieste, Academic Year 2021-2022.

Contents

Abstract

Living organisms often display shape morphing capabilities allowing them to efficiently perform tasks that are fundamental for survival. Understanding the way biological activity is exploited to perform shape changes has a deep impact both on natural sciences and technology, often through a process of reverse engineering. In this thesis, we examine four instances of shape morphing both in synthetic and natural, active structures. In the first Chapter, we analyze the transient shaping of a linear poroelastic plate and investigate how mechanical parameters, strains, and stresses influence the swelling dynamics. We obtain an approximate analytical solution for the case of stress-free evolutions and investigate the effect of stresses in the case of an axisymmetric plate. We show that compressive stresses promote faster swelling with respect to the stress-free case, and vice-versa. In the the second Chapter, we address the question of devising efficient morphing strategies for the attainment of specific shape changes in active structures. We set up an optimal control problem which selects, among the activation patterns producing a prescribed shape change, the one minimizing an objective functional, designed to quantify the complexity of the activation. We provide analytical insights for the case of affine shape changes and, with the aid of numerics, we explore the outcome of different objective functionals in a more general context. Chapter 3 is devoted to the study of active reconfigurations in axons, slender cylindrical structures of neurons, which are responsible for the transmission of electro-chemical signals. Axons are able to actively regulate their thickness trough a contractile coating, named cortex, surrounding the cytoplasm (axoplasm). Here, we develop a continuum model describing the interplay between the cortex contractility and the axoplasm elastic response inherited by a network of microtubules. The validity of our modelling assumptions are supported by an excellent match between numerical simulations and experiments. Finally, in the last Chapter, we develop a teleological model to interpret leaves morphogenesis by accounting for the simultaneous growth of both the venation pattern and the blade. Inspired by previous works in the relevant literature, we develop a continuum model by which leaves growth is driven by a gradient flow maximizing the net power absorbed by the leaf. The numerical solution of the ensuing equations provides preliminary results showing some qualitative agreement with features of existing leaves.

Introduction

Shape transformations are ubiquitous in nature as they are exploited by living organisms to sustain fundamental aspects of life [Gray, 1953, Childress, 1981, Darwin and Darwin, 1896] . These shape changes are typically driven by the energy that the very special architecture of biological tissues is able to extract from the surroundings. This feature is commonly referred to as *internal activity*, a concept which has recently extended to designate those materials that are capable of drawing non-mechanical energy from the environment, and to convert it into mechanical one. These special properties have been recently exploited to design a new generation of materials whose activity pattern can be programmed in space and time, so that shape changes can be attained in a controllable manner. These properties have implications on the emerging field of soft robotics, where soft active materials are employed in the design of novel actuation and sensing devices, often drawing inspiration from nature [Sareh et al., 2013, Noselli et al., 2019, Ford et al., 2019, Riccobelli et al., 2020, Cicconofri et al., 2020, Liu et al., 2021]. Besides its scientific relevance *per se*, it is then clear that a deeper understanding of how nature exploits activity has a strong impact on technology through a process of reverse engineering. Moreover, understanding the role of activity in the definition of the mechanical properties and morphology of biological tissues has important implications on the study of pathological conditions [Dobyns et al., 1993, Lang et al., 2017, Datar et al., 2019, Riccobelli and Bevilacqua, 2020, Riccobelli, 2021].

In the present thesis, we explore four instances of shape morphing in active structures, namely, the transient shaping of thin hydrogel plates, the optimal morphing of planar shapes, the active regulation of axons configuration, and finally the growth of leaves. For the last topic, the discussion is limited to preliminary results and future perspectives.

Many studies focused on the morphing of thin active plates and shells due to their capability to attain large shape transitions [Klein et al., 2007, Efrati et al., 2009, Ambulo et al., 2017, Aharoni et al., 2018, Agostiniani et al., 2019, Lucantonio and DeSimone, 2020]. While their equilibrium configurations have been extensively explored, very little is known about the transient processes involved in such active reconfigurations, apart from mainly experimental reports that recently appeared [Nojoomi et al., 2018, Guseinov et al., 2020, Damioli et al., 2022] (see Fig. 1). Hence, a deeper understanding of these aspects from the theoretical viewpoint is necessary to enhance shape control in time and to develop novel, bioinspired actuation and sensing strategies. Here, we contribute to this point by focusing on the transient morphing of hydrogel plates (Chapter 1). Hydrogels are among the most commonly used active materials for programming complex shape changes, along with liquid crystal elastomers and electroactive polymers, thanks to their ability to isotropically swell (or shrink) as a consequence of solvent absorption (or release) in response to an external stimulus (a change in the chemical potential of the environmnent). We analyze the transient morphing of a linear poroelastic plate model of Kirchhoff type by showing how mechanical parameters, strains and stresses influence the swelling dynamics. Due to the linearity of the
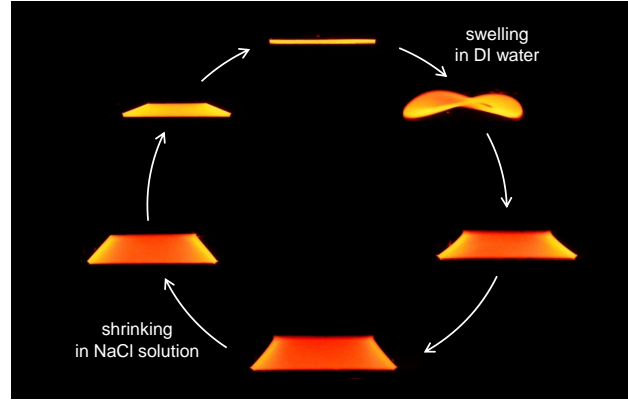
Figure 1: Active hydrogel plates designed to achieve axisymmetric equilibrium configurations exhibit non-axisymmetric transient shapes at early times due to faster swelling at the rims. Lateral solvent fluxes induces compressive stresses that trigger buckling. (adapted from [Damioli et al., 2022])

model, the in-plane strain dynamics is fully decoupled from that of the curvature. In particular, the chemical potential at the top and bottom face of the plate can be chosen so as to select any of the admissible evolutions of in-plane strain and curvature. On the other hand, we show that solvent diffusion cannot be decoupled from strain evolution except from some degenerate cases. For the case of stress-free evolutions, we obtain an approximate analytical solution revealing an exponential decay in time for the in-plane and out-of-plane displacement fields depending on the ratio between the Lamé moduli. As a final step, we investigate the effect of stresses on the swelling dynamics. In particular, we compute a semi-analytical solution for the case of a circular plate loaded with axisymmetric boundary conditions for the chemical potential. We show that compressive stresses promote faster swelling with respect to the stress-free case and vice-versa.

As already mentioned, programming a shape transformation of an active structure requires either the control of the spatial distribution of the material architecture or of the external stimuli triggering the active response [Jeon et al., 2017, Nojoomi et al., 2018, Aharoni et al., 2018, Andrini et al., 2020, Guseinov et al., 2020, Leronni and Bardella, 2021]. For instance, in hydrogels, the amount of swelling can be controlled by locally prescribing the degree of polymerization of the matrix [Hong et al., 2008, Chester and Anand, 2010, Lucantonio et al., 2013]. Regarding liquid crystal elastomers, temperature-driven molecular reorientations cause active strains along mutually orthogonal directions that can be encoded in the material during fabrication [Warner and Terentjev, 2003, Sawa et al., 2010]. In practice, each active material features a specific active mechanism whose convenience in applications strongly depends on the desired shape change. Then, a relevant and timely question is to devise new strategies and tools for identifying the active mechanism that is most efficient for the attainment of a specific shape change. In Chapter 2, we address this question by setting an optimal control problem that selects, among the activation patterns producing a prescribed shape change, the one minimizing an objective functional (see Fig. 2). In the following we will refer to it as the *complexity functional*, since it is designed to quantify the complexity of the activation pattern. As regards the description of activity, differently from previous works on the topic ([Günnel and Herzog, 2016, Lucantonio and DeSimone, 2020, Ortigosa et al., 2021]), we do not restrict the study to a specific material architecture and adopt the target metric [Efrati et al., 2013] as its unifying descriptor. The intent is to develop a design tool that applies to a broad set of materials, and may inspire new efficient morphing strategies. We first focus on the case of shape
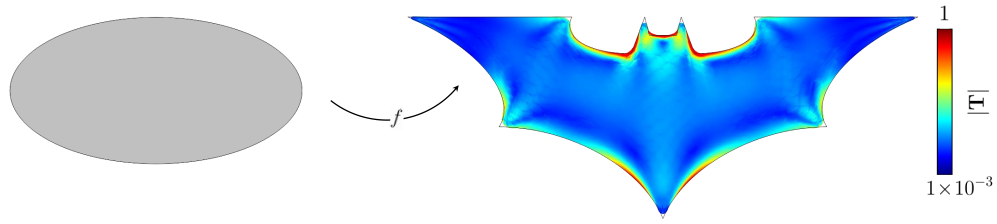
Figure 2: Example of an extreme shape change, result of the optimal control problem

changes attainable through an affine map (*i.e.* affine shape changes), for which we characterize analytically some of the optimal solutions, thus providing insight into the problem. Indeed, affine shape changes always guarantee the existence of a spatially homogeneous activation pattern (*i.e.* a uniform target metric) as an admissible competitor of the optimal control problem. We investigate the optimality of these competitors in Section 2.4 of Chapter 2 and summarize the results in Proposition 3. We test our finding numerically by discretizing the optimal control problem with finite elements, showing perfect agreement with the theoretical predictions. Finally, we discuss non-affine shape changes by investigating the bending of a rectangular block and analyzing the impact on the optimal solutions of different complexity functionals. Some of them are chosen to demonstrate the compatibility of our approach with some classes of existing materials, such as hydrogels and nematic elastomers. Interestingly, the optimal solutions often feature a non-trivial stress pattern, which turns out to be functional to the reduction of the complexity of the activation. In our opinion, the relevance of the presented case study is twofold. On the one hand, it shows that the appropriate choice of a complexity functional leads to the optimal design of target metrics compatible with a specific material class. On the other hand, it highlights that our computational tool may be employed to devise novel morphing strategies or material architectures, where stresses promote a reduction in the complexity of the controls.

As a third instance of morphing in active structures, Chapter 3 focuses on the mechanisms regulating the active reconfigurations of axons, slender cylindrical structures of neurons whose purpose is the transmission of electro-chemical signals to neighbouring cells. Axons comprise a cytoplasmic core, called axoplams, and a surrounding coating named cortex. The axoplasm inherits elastic properties mainly from the presence of a bundle of crosslinked microtules, contributing to the structural integrity of the axon. The cortex, instead, is made of F-actin filaments interconnected by Myosin II molecular motors, whose coordinated activity is able to generate active contractions along the hoop and axial directions. The interplay between the microtubule network and the cortical actomyosin machinery aims at maintaining the cylindrical shape of the axon [Ouyang et al., 2013]. Indeed, microtules disruption or contractility issues in the cortex have shown to lead to degeneration of the axon's shape (such as *axonal beading* see Fig. 3), which is a hallmark of several pathological conditions, such as Alzheimer's and Parkinson's diseases [Stokin et al., 2005, Tagliaferro and Burke, 2016, Riccobelli, 2021]. Moreover, mature axons are capable of adaptively change their diameter to properly enhance signal transmission [Costa et al., 2018]. Therefore, unveiling the mechanism underlying cortical contraction is of the utmost importance to understand how axons maintain their structural stability and to prevent their degeneration. Currently, the compre-
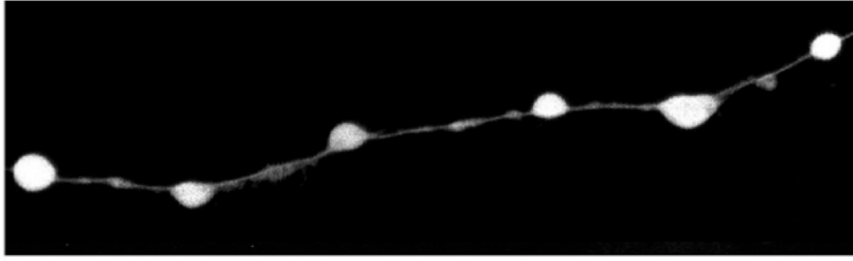
Figure 3: Example of axonal beading (adapted from [Datar et al., 2019])

hension of these mechanisms is still largely unknown. In [Fan et al., 2017], the authors advance the hypothesis of a coupling between active cortical stretches along the hoop and axial directions, whose combined action may produce compression of the axoplasm, thus reducing its diameter. However, the nature of such a coupling and the logic behind active contractility are still unclear. In the present work, we investigate this aspect by proposing a continuum description of the axon. We model active cortical contractility through the multiplicative decomposition of the deformation gradient and, following the approach of [DiCarlo and Quiligotti, 2002], we prescribe an evolution law for the active strains that drives the system toward a homeostatic stress state. Such a stress state is achieved when a suitable linear combination of the components of the Mandel stress is constant. Moreover, differently from previous work in the literature [Dehghany et al., 2020], we propose a coupling of the hoop and axial active stretches through the Mandel stress tensor. Such a coupling spontaneously emerges from the Coleman-Noll procedure that we adopt for deducing a thermodynamically consistent set of equations. We first focus on the stability analysis of axisymmetric solutions, under the simplifying assumption in which both axoplasm and cortex are incompressible. We show the existence of a unique stable equilibrium representing the homeostatic state of the system. We then analyze, with the aid of numerics, a more detailed model in which compressibility of both axoplasm and cortex is accounted for. We calibrate the model parameters to replicate some of the experiments reported in [Fan et al., 2017], where the authors measure changes in the axon's radius as a consequence of an imposed axial stretch and of the delivery of drugs damaging the axoplasm and the cortex. The numerical results show excellent agreement with the experiments. This supports the theoretical assumptions we made for the derivation of the model, namely, the nature of the coupling between hoop and axial active stretches and the existence of a feedback regulation mechanism driving the axon toward a homeostatic stress state.

Unveiling the mechanisms behind growth processes in biological structures is crucial for the understanding of organ morphogenesis and plasticity, the latter intended as the capacity of living organisms to adapt themselves in response to changes of the environmental conditions. In Chapter 4, we focus on the growth of leaves, which are often considered as a prototypical example of solid active tissue. Leaves are complex systems interacting with the environment through the exchange of mass and energy. They are responsible for photosynthetic processes, which allow the plant to synthesize nutrients for sustaining life. Because of their importance, leaves have been subject to intense evolutionary pressures making them highly efficient at carrying out their tasks. We study the growth of leaves following a *teleological* approach (see [Murray, 1926]), according to which natural phenomena are explained in terms of the purpose they serve, rather then the accurate description of the physics behind them. More specifically, we are interested in modelling the growth of the leaf blade and the corresponding venation pattern for sap transport. Such a problem
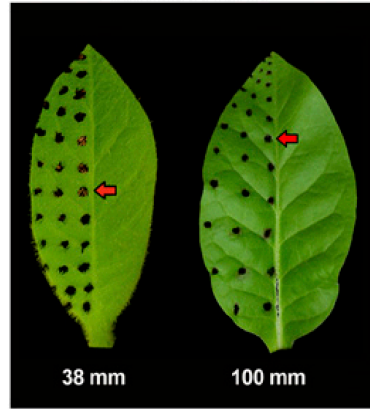
Figure 4: Example of positive allometric growth in a tabacum leaf. The black marker dots in the younger leaf (on the left) do not maintain a uniform distribution in the older leaf (on the right) thus indicating a non uniform growth pattern (the red arrows are there to track the position of a single marker). Moreover growth pattern exhibits a polarity by which, growth rate are more intense at the base of the leaf rather than at its tip. This is an instance of basipetal *growth. (Adapted from [Das Gupta and Nath, 2015])*

was first addressed in [Xia, 2007] using a discrete teleological model, where new leaf's cells are generated only if the revenue they produce through light absorption is greater than transport cost needed to reach them with nutrients. In the present work, we embrace this principle and embed it into a continuum framework as a way to overcome some of the inherent limitations of the model presented in [Xia, 2007], which does not describe the bulk growth pattern leading to the final shape of the leaf. In fact, as reported in [Das Gupta and Nath, 2015], leafs often show an *allometric growth*, namely, the growth rate is non-homogeneous throughout the leaf blade and exhibits spatial polarity. Hence, in order to deal with allometric growth, we develop a continuum model describing the evolution of the leaf blade using a growth map (also referred to as fate map in the biological literature). Moreover, inspired by [Lu and Hu, 2022], we model the formation of veins through a phase field approach based on the introduction of a conductance field. The evolution of the growth map and the conductance is ruled by a gradient flow of the net power absorbed by the leaf. This quantity is given by the difference between the light energy absorbed by the leaf blade and the energy cost for the transport of nutrients. Given the complexity of the gradient flow equations, we solve them using the finite element method. While preliminary, the numerical results show how growth arises as the result of a non-trivial interplay between the expansion of the blade and the formation of the veins. Further developments are discussed in the end of Chapter 4.

Chapter 1

A theoretical study on the transient morphing of linear poroelastic plates

1.1 Introduction

Understanding the way natural systems control and exploit shape changes to achieve biological functions is currently the subject of intense research [Goriely and Ben Amar, 2005, Armon et al., 2011, Arroyo and DeSimone, 2014, Pezzulla et al., 2018, Noselli et al., 2019, Cicconofri et al., 2020]. In material science and technology, this investigation has inspired the realization of synthetic replicas of natural shape morphing mechanisms using smart materials, such as polymer gels, liquid crystal elastomers, shape memory and electroactive polymers. Particular attention has been devoted to slender or thin structures, such as plates and shells, since these can attain large shape transitions as a result of their energetic preference for bending over in-plane stretching. In this context, a general theory explaining how active in-plane strains can induce shape changes was developed by Sharon and coworkers, who first introduced the concept of non-Euclidean plates [Klein et al., 2007, Efrati et al., 2009]. This theory, which is based on the subtle interplay between plate metric and curvature, has often been applied to explore the equilibrium configurations of swelling hydrogels and liquid crystal elastomers [Ambulo et al., 2017, Aharoni et al., 2018, Agostiniani et al., 2019, Lucantonio and DeSimone, 2020]. However, very little is known about the transient processes involved in the morphing of slender structures, apart from mainly experimental reports that have only recently appeared [Nojoomi et al., 2018, Guseinov et al., 2020, Damioli et al., 2022]. Hence, a deeper understanding of these aspects from the theoretical viewpoint is necessary to enhance shape control in time and to develop novel, bioinspired actuation and sensing strategies.

In this work, we focus on the transient shape morphing of poroelastic plates made of swelling gels. Despite geometric non-linearities play a crucial role in determining the configurations of active plates, we employ a linearized theory that is amenable to explicit analytical treatments, thus allowing for deeper insight into the physics of transient morphing. Moreover, we choose to consider a homogeneous plate subject to a prescribed distribution of the chemical potential at the boundary. This problem may be relevant in applications involving thin membranes at the interface between fluids or, more generally, exposed to heterogeneities of the fluid environment. This approach is alternative to considering plates with heterogeneous material properties (in-plane or across the thickness) subject to a homogeneous chemical potential at the boundary.

The Chapter is organized as follows. Section 1.2 is devoted to a short review of the theory of

nonlinear transport in porous media. In Section 1.3, we derive the linear plate model through a formal dimension-reduction procedure and set the initial-boundary value problem corresponding to the free-shaping of a gel plate immersed in a solvent bath. In Section 1.4, we discuss the general properties of the solution to such a problem, namely, uniqueness and dependence on boundary data. In Section 1.5, we analyze a special class of solutions that we refer to as *stress-free*, since they are characterized by null stress resultants along the thickness. In particular, we derive conditions on the boundary chemical potential leading to stress-free evolutions and fully characterize the realizable shapes, both in terms of in-plane strain and curvature. We obtain accurate, explicit formulas for the time courses of these quantities and of chemical potential. Finally, in Section 1.6 we exploit a semi-analytical approach to study the problem in which elasticity and solvent transport are *fully-coupled*. This analysis is carried out with reference to a circular plate, in order to evaluate the effect of stresses on the dynamics of swelling.

1.2   A short review of nonlinear fluid transport in porous media

Following [Lucantonio et al., 2013, Miehe et al., 2015], we consider the solid-fluid mixture as a homogenized medium allowing for a mass flux of the liquid phase (solvent)[1]. The reference configuration of the body is identified with a regular region $\mathcal{B}$ of the Euclidean space $\mathbb{E}^3$, and it is subjected to a motion described by a map $f : \mathcal{B} \times \mathcal{I} \to \mathbb{E}^3$ assigning to each material point $X \in \mathcal{B}$ and time $t \in \mathcal{I}$ a place $x \in \mathbb{E}^3$. We will denote with $\mathcal{B}_t$ the image, trough f, of $\mathcal{B}$ and with $\mathcal{T} = \{(x, t) \text{ such that } x \in \mathcal{B}_t, t \in \mathcal{I}\}$ the trajectory.

Balance laws   Let us first formulate the mass balance for the fluid phase by introducing a spatial field $c_{\mathrm{s}} : \mathcal{T} \to \mathbb{R}^+$ for the concentration of solvent. Specifically, c_{s} assigns to each place x and time t the number of moles per unit current volume. Then, the number of solvent moles in a part of the body $\mathcal{P}_t \subset \mathcal{B}_t$ is given by

$$M(t) = \int_{\mathcal{P}_t} c_s, \qquad \mathcal{P}_t = f(\mathcal{P}, t).$$

In order to formulate a diffusion equation for c_s, we introduce the *spatial* flux $\mathbf{h}_s$ representing the flow rate of solvent moles per unit surface. If we assume that no internal sources are present, the mass balance reads

$$\dot{M}(t) = -\int_{\partial\mathcal{P}_t} \mathbf{h}_s \cdot \mathbf{m}, \tag{1.1}$$

where $\mathbf{m}$ denotes the outward unit normal to $\partial\mathcal{P}_t$. Equation (1.1) can be easily pulled back onto the reference configuration leading to

$$\int_{\mathcal{P}} \dot{c} = -\int_{\partial\mathcal{P}} \mathbf{h} \cdot \mathbf{n}, \tag{1.2}$$

where $c = Jc_m$, $c_m = c_s \circ f$ and $\mathbf{h} = J\mathbf{F}^{-1}\mathbf{h}_m$, $\mathbf{h}_m = \mathbf{h}_s \circ f$ are the material descriptions of the concentration and the solvent flux, respectively. Finally, equation (1.2) can then be localized into

$$\dot{c} = -\mathrm{Div}\,\mathbf{h} \text{ on } \mathcal{B}. \tag{1.3}$$

---

[1]A different approach based on mixture theories is also possible. For a discussion on the differences between the two approaches see [Tomassetti, 2022].

As a next step, we introduce the force balance. Let us denote by $\mathbf{b}(X, t)$ the body forces on $\mathcal{B}$ and by $\mathbf{S}(X, t)$ the first Piola-Kirchhoff stress tensor. Then, according to the standard theory of continuum mechanics (see [Gurtin, 1982]), the force balance reads

$$\mathrm{Div}\, \mathbf{S} = \mathbf{b} \text{ on } \mathcal{B}. \tag{1.4}$$

We remark that, since the times scales of solvent diffusion are much larger than inertial ones, the body forces $\mathbf{b}$ only account for non-inertial loads, namely, we considered an over-damped dynamics.

Constitutive relations   In addition to the balance laws, we need to specify the material response of the body by prescribing the constitutive relations for the stress tensor and the flux. To deduce thermodynamically consistent relations we employ the Coleman-Noll procedure, relying on the dissipation inequality. Following [Gurtin et al., 2010], we write the dissipation inequality by requiring the total free energy rate to be less than or equal to the loads power, $\mathcal{F}$, plus the energy flow due to solvent transport, $\mathcal{Y}$. Consequently, if we denote with Φ the free energy density per unit volume, the dissipation inequality reads

$$\frac{\mathrm{d}}{\mathrm{d}t} \int_{\mathcal{P}} \Phi \leq \mathcal{F} + \mathcal{Y}, \tag{1.5}$$

where, by definition

$$\mathcal{F} = \int_{\mathcal{P}} \mathbf{b} \cdot \dot{f} + \int_{\partial \mathcal{P}} \mathbf{t} \cdot \dot{f},$$

which, thanks to the balance law in Eq. (1.4), can be rewritten as

$$\mathcal{F} = \int_{\mathcal{P}} \mathbf{S} \cdot \dot{\mathbf{F}}. \tag{1.6}$$

On the other hand, the energy flow $\mathcal{Y}$ is assumed to be characterized through the chemical potential $\mu(X, t)$ as

$$\mathcal{Y} = - \int_{\partial \mathcal{P}} \mu \mathbf{h} \cdot \mathbf{n},$$

which, thanks to the balance law in Eq. (1.3), can be rewritten as

$$\mathcal{Y} = \int_{\mathcal{P}} (\mu \dot{c} - \mathbf{h} \cdot \nabla \mu). \tag{1.7}$$

Then, by substituting Eqs. (1.6), (1.7) into Eq. (1.5) and assuming Φ to be a function of $\mathbf{F}$, c, and $\nabla \mu$, we can write the local dissipation inequality as

$$(\partial_{\mathbf{F}} \Phi - \mathbf{S}) \cdot \dot{\mathbf{F}} + \partial_{\nabla \mu} \Phi \cdot \nabla \dot{\mu} + (\partial_c \Phi - \mu) \cdot \dot{c} + \mathbf{h} \cdot \nabla \mu \leq 0. \tag{1.8}$$

Since Eq. (1.8) is assumed to hold for each admissible continuation of the processes, we deduce that the energy density Φ cannot depend on $\nabla \mu$ and that the following constitutive relations hold

$$\mathbf{S} = \partial_{\mathbf{F}} \Phi, \quad \mu = \partial_c \Phi. \tag{1.9}$$

The above equation also implies that both μ and $\mathbf{S}$ depend only on the pair $(\mathbf{F}, c)$. Then, equation (1.8) reduces to $\mathbf{h} \cdot \nabla \mu \leq 0$ namely, to a compatibility condition for the constitutive relations for

h indicating that solvent diffusion is the only irreversible phenomenon of the system. Following [Miehe et al., 2015], an admissible constitutive assumption for **h** is given by

$$\mathbf{h} = \partial_{\nabla\mu}\varphi^*(\mathbf{F}, c, \nabla\mu), \tag{1.10}$$

representing a generalized Darcy's law. The function φ^* is referred to as *(Dual) dissipation potential* and is typically assumed to be convex with respect to $\nabla\mu$ so as to satisfy $\mathbf{h} \cdot \nabla\mu \leq 0$. As a final consideration we remark that, in order to satisfy material indifference both **h** and **S** (and consequently Φ) must depend on **F** trough the Cauchy-green strain tensor **C**.

Summarizing, the set of equations for the fluid transport in porous media is then constituted by Eqs. (1.3), (1.4), (1.9) and (1.10) to be solved with suitable initial conditions and the following boundary conditions

$$\begin{aligned}
\mu &= \mu_* \text{ on } \partial\mathcal{B}_\mu, & \mathbf{h} \cdot \mathbf{n} &= h_* \text{ on } \partial\mathcal{B}_\mathbf{h}, \\
f &= f_* \text{ on } \partial\mathcal{B}_\mathbf{u}, & \mathbf{Sn} &= \mathbf{t}_* \text{on } \partial\mathcal{B}_\mathbf{t}.
\end{aligned} \tag{1.11}$$

1.2.1   Variational principle

The equations for fluid transport in porous media already introduced can be recast in a variational form, specifically, they arise as the Euler equations of a *canonical rate of energy* functional, as shown in the following.

Let us first consider the rate of free energy

$$\mathscr{F}(\dot{f}, \dot{c}) = \int_\mathcal{B} (\partial_\mathbf{F}\Phi \cdot \dot{\mathbf{F}} + \partial_c\Phi \cdot \dot{c}),$$

and rewrite it as a function of f and **h** by means of Eq. (1.3), namely

$$\mathscr{F}(\dot{f}, \mathbf{h}) = \int_\mathcal{B} (\partial_\mathbf{F}\Phi \cdot \dot{\mathbf{F}} - \partial_c\Phi \cdot \text{Div}\,\mathbf{h}). \tag{1.12}$$

We will refer to $\mathscr{F}$ as the *canonical rate of free energy functional*. We remark that Eq. (1.12) is meaningful only when coupled with the mass balance equation (1.3), which thus plays the role of a constraint. In addition, let us define the canonical dissipation density as the Legendre transformation of the dual dissipation potential in Eq. (1.12), namely

$$\varphi(\mathbf{h}; \mathbf{F}, c) = \sup_{\boldsymbol{\xi}}\{\boldsymbol{\xi} \cdot \mathbf{h} - \varphi^*(\boldsymbol{\xi}, \mathbf{F}, x)\}.$$

The *canonical dissipation potential functional* is then defined as

$$\mathscr{D}(\mathbf{h}) = \int_\mathcal{B} \varphi.$$

Finally we define the external load functional as

$$\mathscr{P}^{\text{ext}}(\dot{f}, \mathbf{h}) = \int_\mathcal{B} \mathbf{b} \cdot \dot{f} + \int_{\partial\mathcal{B}_\mathbf{t}} \mathbf{t} \cdot \dot{f} - \int_{\partial\mathcal{B}_\mu} \mu_*\mathbf{h} \cdot \mathbf{n}. \tag{1.13}$$
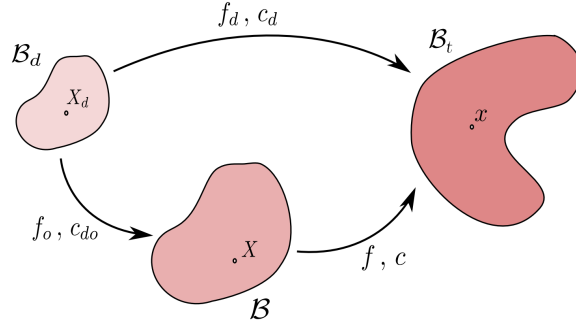
Figure 1.1: Representation of the dry, reference, and actual configurations (Adapted from [Lucantonio et al., 2013])

The set of equations introduced in Section 1.2 can then characterized through a variational problem involving the so called *rate potential*, which is defined as

$$\Pi(\dot{f}, \mathbf{h}) := \mathscr{F}(\dot{f}, \mathbf{h}) + \mathscr{D}(\mathbf{h}) - \mathscr{P}^{\text{ext}}(\dot{f}, \mathbf{h}). \tag{1.14}$$

Specifically, besides the mass balance in Eq. (1.3), the mass flux and the deformation rate at the given state (f, c) are determined as solutions of the following variational problem

$$\min_{\mathbf{u} \in V_{\mathbf{u}} \, \mathbf{h} \in V_{\mathbf{h}}} \Pi(\dot{f}, \mathbf{h}),$$

where

$$V_{\mathbf{u}} = \{\mathbf{u} \in H^1(\mathcal{B}) : \mathbf{u} = 0 \text{ on } \partial\mathcal{B}_{\mathbf{u}}\}, \qquad V_{\mathbf{h}} = \{\mathbf{h} \in H^{\text{div}}(\mathcal{B}) : \mathbf{h} \cdot \mathbf{n} = h_* \text{ on } \partial\mathcal{B}_{\mathbf{h}}\}.$$

1.2.2 Hydrogels

Hydrogels are colloids constituted by a network of cross-linked polymeric filaments dispersed in water. The polymeric network confers the material an elastic behavior, while the migration of the solvent through the network is responsible for the swelling properties of the mixture [Doi, 2009]. Hydrogels can modeled within the framework of fluid transport in porous media and thus can be described through the equations discussed in the previous Subsection. Here, we specialize that theory to the case of hydrogels.

It is generally assumed that both the solid and liquid phase, are separately incompressible. Mathematically, this translates into a *volume constraint* that must be added to the model formulated in the previous Subsection. In order to properly define such a constraint, we first need to define the physical state of the gel corresponding to the reference configuration $\mathcal{B}$. Let us introduce the so called *dry configuration* of the gel, denoted with $\mathcal{B}_{\text{d}}$, characterized by absence of solvent. The reference state $\mathcal{B}$ is then defined as the steady state attained by $\mathcal{B}_{\text{d}}$ through a *free swelling* process described by the map $f_0 : \mathcal{B}_{\text{d}} \to \mathcal{B}$. As regards the notation for fields defined on the configuration $\mathcal{B}_{\text{d}}$, denoting with f a deformation of $\mathcal{B}$, we write: $f_{\text{d}} = f \circ f_0$, $\mathbf{F}_{\text{d}} = \nabla_{\text{d}} f_{\text{d}}$, $J_{\text{d}} = \det \mathbf{F}_{\text{d}}$, $\mathbf{F}_0 = \nabla f_0$, $J_0 = \det \mathbf{F}_0$ and $c_{\text{d}} = J_0 c$, the latter denoting the concentration of solvent per unit dry volume (see Fig. 1.1).

The previously announced volume constraint, arising from the separate incompressibility of the solid and liquid phase, can then be stated as

$$J_{\text{d}} = 1 + \Omega c_{\text{d}}, \tag{1.15}$$

where Ω is the solvent molar volume.

As for the free energy density, we first define it on the dry configuration as the sum of two contributions: the first one regards the solid phase, which is treated as an incompressible *isotropic* rubber, and the second accounts for polymer-solvent interactions, and is known as *mixing energy*. Then, the total free energy density per unit dry volume can be written as

$$\Phi_{\rm d}(\mathbf{F}_{\rm d}, c_{\rm d}) = \frac{1}{2}G_{\rm d}(\mathbf{F}_{\rm d} \cdot \mathbf{F}_{\rm d} - 3) + \frac{\mathcal{R}T}{\Omega}h(c_{\rm d}). \tag{1.16}$$

A common choice for the mixing term h is the Flory-Rehner free energy

$$h(c_{\rm d}) = \Omega c_{\rm d} \log\left(\frac{\Omega c_{\rm d}}{1 + \Omega c_{\rm d}}\right) + \chi(T)\frac{\Omega c_{\rm d}}{1 + \Omega c_{\rm d}},$$

where $G = Nk_BT$ is the shear modulus, N the number of polymeric chains per unit dry volume, k_B the Boltzmann constant, T the temperature, $\mathcal{R}$ the universal gas constant and χ the dimensionless measure of the enthalpy of mixing.

Using kinematic relations, Eq. (1.15) can be rewritten as

$$J = 1 + \Omega c, \tag{1.17}$$

which, substituted into Eq. (1.3) together with the identity $\dot{J} = J\mathbf{F}^{-\mathsf{T}} \cdot \dot{\mathbf{F}}$ for the derivative of J, leads to the following mass balance equation

$$\frac{J\mathbf{F}^{-\mathsf{T}} \cdot \dot{\mathbf{F}}}{\Omega} = -\operatorname{Div}\mathbf{h}. \tag{1.18}$$

Moreover, substitution of Eq. (1.17) into Eq. (1.16) leads to an *effective elastic energy*, $\Phi_{\rm d}^{(0)}(\mathbf{F})$, for the solid skeleton. With the newly defined effective energy, the dissipation inequality (1.5), together with Eq. (1.6), (1.7) and the constraint (1.17), specializes into

$$(\partial_{\mathbf{F}}\Phi^{(0)} - \frac{\mu}{\Omega}J\mathbf{F}^{-\mathsf{T}} - \mathbf{S}) \cdot \dot{\mathbf{F}} - \mathbf{h} \cdot \nabla\mu \leq 0, \tag{1.19}$$

where $\Phi^{(0)} = \Phi_{\rm d}^{(0)}/J_0$ is the effective elastic energy per unit reference volume. The Colemann-Noll procedure applied to Eq. (1.19) produces the following constitutive equation

$$\mathbf{S} = \partial_{\mathbf{F}}\Phi^{(0)} - pJ\mathbf{F}^{-\mathsf{T}}, \tag{1.20}$$

where $p = \mu/\Omega$ is known in literature as the *pore pressure*. Finally, concerning the constitutive assumption for $\mathbf{h}$, it is assumed a standard Fick's law which is trivially compatible with the thermodynamical restriction $\mathbf{h} \cdot \nabla\mu \leq 0$, namely

$$\mathbf{h} = -\mathbf{D}\nabla\mu, \tag{1.21}$$

where $\mathbf{D} = \mathbf{D}(\mathbf{F}, c)$ is a positive semi-definite symmetric tensor known as mobility tensor. Hence the final set of equations for hydrogels is constituted by Eqs. (1.4), (1.18), (1.20), (1.21) together with the boundary conditions in Eq. (1.11).

Similarly to the compressible case, the problem can be recast in a variational form (see [Miehe et al., 2015]). In order to include the incompressibility constraint, the rate potential must by augmented by means of a Lagrange multiplier Λ as follows:

$$\Pi(\dot{f}, \mathbf{h}, \Lambda) := \tilde{\mathscr{F}}(\dot{f}, \Lambda) + \mathscr{D}(\mathbf{h}) - \mathscr{P}^{\rm ext}(\dot{f}, \mathbf{h}), \tag{1.22}$$

where the augmented rate of free energy and the dissipation potential are defined as

$$\tilde{\mathscr{F}}(\dot{f}, \Lambda) = \int_{\mathcal{B}} \left(\partial_{\mathbf{F}} \Phi^{(0)} \cdot \dot{\mathbf{F}} - \Lambda(\Omega^{-1} J \mathbf{F}^{-\mathsf{T}} \cdot \dot{\mathbf{F}} + \mathrm{Div}\, \mathbf{h}) \right), \qquad \varphi(\mathbf{h}) = \frac{\mathbf{D}^{-1}\mathbf{h} \cdot \mathbf{h}}{2},$$

respectively. As before, the stationarity conditions of Eq. (1.22) with respect to $(\dot{f}, \mathbf{h}, \Lambda)$ coincide with Eqs. (1.4), (1.18), (1.20), (1.21) and in addition force the identity $\Lambda = \mu$.

1.2.3 The linearized equations

Here we synthesize the linearization performed in [Lucantonio and Nardinocchi, 2012] on the highly nonlinear equations for hydrogels, derived in the previous section. Such a linearization is made around an equilibrium configuration of the gel. We conveniently assume such an equilibrium to be described by the map f_0 previously introduced, so that $\mathcal{B}$ is the reference configuration. In the case of a hydrogel in absence of external bulk and surface body forces, immersed into a solvent bath, the equilibrium configurations can be shown to be a stress free state featured by a homogeneous spherical deformation gradient $\mathbf{F}_0 = \lambda_0 \mathbf{I}$ and a chemical potential μ_0 homogeneous throughout $\mathcal{B}$. The linearized equations are then

$$\mathrm{div}\, \mathbf{T} = \mathbf{b} \text{ on } \mathcal{B},$$
$$\frac{1}{\Omega} \mathrm{tr} \dot{\mathbf{E}} = -\mathrm{div}\, \mathbf{h} \text{ on } \mathcal{B}, \tag{1.23}$$

where $\mathbf{T}$ is the incremental stress field, $\mathbf{h}$ is the incremental solvent flux and $\mathbf{E} = \mathrm{Sym}\nabla\mathbf{u}$, $\mathbf{u}$ being the displacement field. The above equations are coupled with the boundary conditions

$$\mathbf{T}\mathbf{n} = \mathbf{t}_* \text{ on } \partial\mathcal{B}_{\mathbf{t}}, \quad \mathbf{u} = \mathbf{u}_* \text{ on } \partial\mathcal{B}_{\mathbf{u}},$$
$$-\mathbf{h} \cdot \mathbf{n} = h_* \text{ on } \partial\mathcal{B}_{\mathbf{h}}, \quad \mu = \mu_* \text{ on } \partial\mathcal{B}_\mu.$$

As for the constitutive laws, we get the usual Fick's law for $\mathbf{h}$, namely

$$\mathbf{h} = -\mathbf{D}\nabla\mu, \tag{1.24}$$

where μ denotes the increment of chemical potential with respect to the equilibrium state μ_0. Concerning $\mathbf{T}$, we write following expression

$$\mathbf{T} = 2G\mathbf{E} + \lambda \mathrm{tr}(\mathbf{E})\mathbf{I} - \frac{\mu}{\Omega}\mathbf{I},$$

where

$$G = \frac{G_{\mathrm{d}}}{\lambda_0}, \qquad \lambda = -G + \frac{\mathcal{R}T}{\Omega} \frac{J_0 - 2\chi(J_0 - 1)}{J_0^2(J_0 - 1)},$$

with $J_0 = \lambda_0^3$ denoting the Jacobian of $\mathbf{F}_0$. Similarly to its nonlinear counterpart, the linearized model can be shown to emerge from a variational principle for the minimization of a *mixed* rate potential Π_ℓ often referred to as Rayleighian. The linearized version of Eq. (1.22) then reads

$$\Pi_\ell(\dot{\mathbf{u}}, \mathbf{h}, \Lambda) = \int_{\mathcal{B}} \left[\partial_{\mathbf{E}} \Phi_\ell^{(0)} \cdot \nabla\dot{\mathbf{u}} + \varphi(\mathbf{h}) - \Lambda\left(\frac{\mathrm{tr}\dot{\mathbf{E}}}{\Omega} + \mathrm{div}\, \mathbf{h}\right) \right] + \int_{\partial\mathcal{B}_\mu} \mu_* \mathbf{h} \cdot \mathbf{n}, \tag{1.25}$$
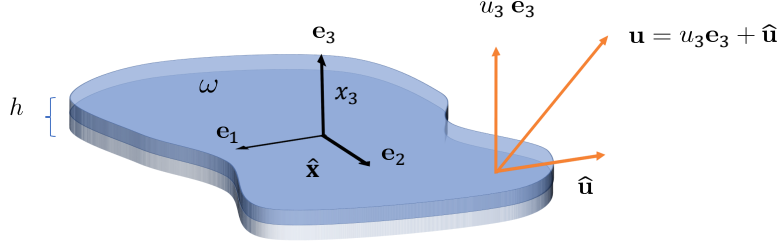
Figure 1.2: Domain $\mathcal{B}$ of a plate. We illustrate the orthonormal reference frame $\{\mathbf{e}_j\}$, the Cartesian coordinates $\hat{\mathbf{x}}$ and x_3 for points in $\mathcal{B}$, and the displacement $\mathbf{u}$ decomposed into the in-plane part, $\hat{\mathbf{u}}$, and the transverse one, u_3.

where $\Phi_\ell^{(0)}$ is the linearized effective free energy density and φ is the dual dissipation potential. They read

$$\Phi_\ell^{(0)}(\mathbf{E}) = 2G|\mathbf{E}|^2 + \lambda(\mathrm{tr}\mathbf{E})^2, \qquad \varphi(\mathbf{h}) = \frac{\mathbf{D}^{-1}\mathbf{h}\cdot\mathbf{h}}{2}.$$

respectively. We finally remark that, the stationarity of the problem (1.25) leads to a *mixed* weak formulation of problem (1.23) and, as for the nonlinear case, to the identification of the Lagrange multiplier Λ with the chemical potential μ.

1.3 Dimensional reduction of linear poroelastic plates

In this Section, we perform a dimensional reduction to derive the isotropic linear poroelastic plate model that we will employ for the study of transient swelling processes. The system of evolution equations for Kirchhoff linear poroelastic plates was first derived by Taber in [Taber, 1992] starting from the three-dimensional setting, see [Biot, 1941], and later justified in [Marciniak-Czochra and Mikelić, 2015, Paroni and Tomassetti, 2018]. Here we propose an alternative derivation, following a formal asymptotic expansion approach inspired by [Miara, 1994].

In the linear approximation, the referential and current configurations merge in to one and consequently they become indistinguishable. We then chose to denote points and vectors by adopting the spatial notation. Let $(\mathbf{e}_1, \mathbf{e}_2, \mathbf{e}_3)$ be an orthonormal base for $\mathbb{R}^3$, and let $\mathcal{B} = \omega \times (-h/2, h/2) \subset \mathbb{R}^3$ be the reference configuration of the plate in its initial equilibrium state. Here, $\omega \subset \mathbb{R}^2$ represents the mid-surface of the plate, whereas h denotes its thickness. We write $(\hat{\mathbf{x}}, x_3) \in \mathcal{B}$ for the position vector of a point of the plate, such that $\hat{\mathbf{x}} = (x_1, x_2) \in \omega$ and $x_3 \in (-h/2, h/2)$ are the in-plane and the transverse Cartesian coordinates, respectively. As for the top and bottom surfaces of the plate, these are denoted by $\omega_+ = \omega \times \{h/2\}$ and by $\omega_- = \omega \times \{-h/2\}$ (see Fig. 1.2).

Let us then consider the system of equations in (1.23), coupled with the Fick's law in Eq. (1.24) with isotropic mobility tensor

$$\mathbf{D} = D\mathbf{I},$$

where $D > 0$. Moreover we assume that no bulk loads are present (*i.e.* $\mathbf{b} = 0$) and equip the system with the following boundary conditions:

$$\begin{cases} \mathbf{u} = 0 & \text{on } \partial\mathcal{B}_{\mathbf{u}} = \partial\omega_{\mathbf{u}} \times \left[-\frac{h}{2}, \frac{h}{2}\right], \\ \mathbf{Tn} = 0 & \text{on } \partial\mathcal{B}_{\mathbf{t}} = \partial\mathcal{B} \setminus \partial\mathcal{B}_{\mathbf{u}}, \\ \mu = \mu_* & \text{on } \partial\mathcal{B}_{\mu} = \partial\mathcal{B}, \end{cases} \tag{1.26}$$

where $\partial\omega_{\mathbf{u}} \subset \partial\omega$. Hence, the plate is supposed to be clamped on a portion of its boundary and subjected to null tractions on the remaining part. Moreover, we assume it to be immersed into a solvent bath and therefore, to be subject to Dirichlet boundary conditions for the chemical potential, namely $\mu = \mu_*$ on $\partial\mathcal{B}$. We remark that clamping the plate is necessary for deriving a set of well posed mathematical equations with a unique solution. However, as usual in mechanical problems, as long as infinitesimal rigid displacements are ruled out, also the traction free problem is well posed, as shown in the following sections.

Finally, we prescribe the following set of initial conditions

$$\mathbf{u}|_{t=0} = 0, \qquad \mathbf{h}|_{t=0} = 0, \qquad \mu|_{t=0} = 0.$$

For the purpose of dimensional reduction, we find it convenient to work with the system of equations (1.23) written in weak form. In particular, we adopt a *mixed* weak formulation which has the advantage of having the Dirichlet boundary conditions for μ directly embedded in the equations and not in the functional spaces. Indeed, as we will see, this allows for an easier handling of the boundary conditions for μ. The mixed weak formulation reads: find $\mathbf{u} \in V_{\mathbf{u}}(\mathcal{B})$, $\mathbf{h} \in V_{\mathbf{h}}(\mathcal{B})$ and $\mu \in V_{\mu}(\mathcal{B})$ such that

$$\begin{cases} \displaystyle\int_{\mathcal{B}} (2G\mathbf{E} + \lambda\mathrm{tr}(\mathbf{E})\mathbf{I}) \cdot \nabla\mathbf{v} - \frac{1}{\Omega} \int_{\mathcal{B}} \mu\mathrm{div}\,(\mathbf{v}) = 0 & \forall \mathbf{v} \in V_{\mathbf{u}}(\mathcal{B}), \\[2ex] \displaystyle\int_{\mathcal{B}} \mu\mathrm{div}\,(\boldsymbol{\psi}) - \int_{\mathcal{B}} N\mathbf{h} \cdot \boldsymbol{\psi} = \int_{\partial\mathcal{B}} \mu_*\boldsymbol{\psi} \cdot \mathbf{n} & \forall \boldsymbol{\psi} \in V_{\mathbf{h}}(\mathcal{B}), \\[2ex] \displaystyle\int_{\mathcal{B}} \partial_t\mathrm{div}\,(\mathbf{u})\phi = \int_{\mathcal{B}} -\Omega\mathrm{div}\,(\mathbf{h})\phi & \forall \phi \in V_{\mu}(\mathcal{B}). \end{cases} \tag{1.27}$$

Due to the formal nature of present dimensional reduction, no attempt is made to rigorously define the functional spaces involved. It is then enough to characterize them as follows:

$$\mathbf{V}_{\mathbf{u}}(\mathcal{B}) = \{\mathbf{v} \text{ smooth s.t } \mathbf{v}|_{\partial\mathcal{B}_{\mathbf{u}}} = 0\}, \qquad \mathbf{V}_{\mathbf{h}}(\mathcal{B}) = \{ \text{ smooth on } \mathcal{B}\}, \qquad V_{\mu}(\mathcal{B}) = \{ \text{ smooth on } \mathcal{B}\}.$$

The purpose of dimensional reduction is to find an asymptotic regime for the problem in Eq. (1.27) in the limit when the thickness of the plate, h, is very small. We notice that, in Eq. (1.27), the domain $\mathcal{B}$ depends on h, which is unsuitable for making calculations. Hence, we nondimensionalize the problem by rescaling it into a fixed domain independent on h. Specifically, we will define the following nondimensional quantities

$$\hat{\mathbf{x}}' = \frac{\hat{\mathbf{x}}}{\ell}, \quad x_3' = \frac{x_3}{h}, \quad t' = \frac{t}{\tau}, \quad \mu' = \frac{\mu}{G\Omega}, \quad \mathbf{u}' = \frac{\mathbf{u}}{\ell}, \quad \mathbf{h}' = \frac{\mathbf{h}}{G\Omega D/\ell},$$

where $\tau = h^2/D\Omega^2(\lambda + 2G)$ and ℓ is a characteristic length of ω. The domain on which the rescaled equations are defined is $\mathcal{B}' = \omega' \times [-\frac{1}{2}, \frac{1}{2}]$ where ω' is the rescaled counterpart of ω, formally

$\omega' = \omega/\ell^2$. Moreover, it will be useful to extend the notation already used for position vectors, and distinguish between in-plane quantities (denoted by a superposed hat) and transverse ones (labeled with a subscript "3"). In particular we define

$$\hat{\mathrm{div}}' = \frac{\partial}{\partial x_1'} + \frac{\partial}{\partial x_2'}, \quad \hat{\Delta}' = \frac{\partial^2}{\partial x_1'^2} + \frac{\partial^2}{\partial x_2'^2}, \quad \hat{\nabla}' = \left(\frac{\partial}{\partial x_1'}, \frac{\partial}{\partial x_2'} \right),$$

and

$$\hat{\mathbf{u}}' = \left(u_1', u_2' \right), \quad \hat{\mathbf{h}}' = \left(h_1', h_2' \right), \quad \hat{\mathbf{E}}(\hat{\mathbf{u}}') = \mathrm{Sym}\hat{\nabla}'\hat{\mathbf{u}}'.$$

To lighten up the notation, we drop the $\hat{}$ symbol so that, from now on, bold symbols will denote in-plane vectors and tensors, and differential operators will refer to their in-plane counterpart. Moreover, unless specified, we will always write the equations in the rescaled domain so that all the primes can be dropped and no confusion should arise.

Then, the equations in (1.27), recast in non-dimensional form, read: find $\mathbf{u} \in \mathbf{V_u}(\mathcal{B})$, $u_3 \in V_\mathbf{u}^3(\mathcal{B})$, $\mathbf{h} \in \mathbf{V_h}(\mathcal{B})$, $h_3 \in V_\mathbf{h}^3(\mathcal{B})$ and $\mu \in V_\mu(\mathcal{B})$ such that

$$\varepsilon \int_\mathcal{B} \eta \nabla u_3 \cdot \nabla v_3 + \int_\mathcal{B} \left(\mathrm{tr}\mathbf{E}(\mathbf{u}) - \eta\mu \right) \partial_3 v_3 + \eta \partial_3 \mathbf{u} \cdot \nabla v_3 + \tag{1.28a}$$

$$+ \frac{1}{\varepsilon} \int_\mathcal{B} (1 + 2\eta) \partial_3 u_3 \partial_3 v_3 = 0 \quad \forall v_3 \in V_\mathbf{u}^3(\mathcal{B}),$$

$$\varepsilon \int_\mathcal{B} \left(\mathrm{tr}\mathbf{E}(\mathbf{u}) - \eta\mu \right) \mathrm{tr}\mathbf{E}(\mathbf{v}) + 2\eta\mathbf{E}(\mathbf{u}) \cdot \mathbf{E}(\mathbf{v}) +$$

$$+ \int_\mathcal{B} \partial_3 u_3 \mathrm{tr}\mathbf{E}(\mathbf{v}) + \eta \nabla u_3 \cdot \partial_3 \mathbf{v} + \frac{1}{\varepsilon} \int_\mathcal{B} \eta \partial_3 \mathbf{u} \cdot \partial_3 \mathbf{v} = 0 \quad \forall \mathbf{v} \in \mathbf{V_u}(\mathcal{B}), \tag{1.28b}$$

$$\frac{1}{\varepsilon^2} \int_\mathcal{B} \frac{1 + 2\eta}{\eta} \phi \partial_t \partial_3 u_3 + \frac{1}{\varepsilon} \int_\mathcal{B} \frac{1 + 2\eta}{\eta} \partial_t \mathrm{tr}\mathbf{E}(\mathbf{u}) \phi +$$

$$- \int_\mathcal{B} \phi \partial_3 h_3 + \varepsilon \int_\mathcal{B} \mathrm{div}\,\mathbf{h} \phi = 0 \quad \forall \phi \in V_\mu(\mathcal{B}), \tag{1.28c}$$

$$\varepsilon \left(\int_\mathcal{B} \mu \mathrm{div}\,\boldsymbol{\psi} - \int_\mathcal{B} \mathbf{h} \cdot \boldsymbol{\psi} - \int_{\partial\mathcal{B}} \mu_* \boldsymbol{\psi} \cdot \mathbf{n} \right) = 0 \quad \forall \boldsymbol{\psi} \in \mathbf{V_h}(\mathcal{B}), \tag{1.28d}$$

$$\int_\mathcal{B} \mu \partial_3 \psi_3 - \varepsilon \int_\mathcal{B} h_3 \psi_3 - \int_{\omega_+ \cup \omega_-} \mu_* \psi_3 n_3 = 0 \quad \forall \psi_3 \in V_\mathbf{h}^3(\mathcal{B}), \tag{1.28e}$$

where we have defined the dimensionless groups

$$\eta = \frac{G}{\lambda}, \quad \varepsilon = \frac{h}{\ell},$$

and the functional spaces

$$V_\mathbf{u}^3(\mathcal{B}) := \{ v_3 \text{ smooth s.t } v_3|_{\partial\mathcal{B}_\mathbf{u}} = 0 \}, \quad \mathbf{V_u}(\mathcal{B}) := \{ \mathbf{v} \text{ smooth s.t } \mathbf{v}|_{\partial\mathcal{B}_\mathbf{u}} = 0 \},$$

$$V_\mathbf{h}^3(\mathcal{B}) := \{ \psi_3 \text{ smooth on } \mathcal{B} \}, \quad \mathbf{V_h}(\mathcal{B}) := \{ \psi_3 \text{ smooth on } \mathcal{B} \}.$$

As a side remark, observe that the third integral in Eq. (1.28e) is performed on $\omega_+ \cup \omega_-$ rather than on $\partial \mathcal{B}$ since $n_3 \equiv 0$ on $\partial \mathcal{B} \setminus (\omega_+ \cup \omega_-)$.

In order to carry out the dimensional reduction, we rely upon the procedure proposed in [Miara, 1994]. First, we expand the unknowns in power of ε, namely

$$\mathbf{u} = \sum_k \varepsilon^k \mathbf{u}^k, \quad \mathbf{h} = \sum_k \varepsilon^k \mathbf{h}^k, \quad u_3 = \sum_k \varepsilon^k u_3^k, \quad h_3 = \sum_k \varepsilon^k h_3^k, \quad \mu = \sum_k \varepsilon^k \mu^k, \qquad (1.29)$$

substitute the expansions into the rescaled equations (1.28a)-(1.28e) and equate equal powers in ε. The procedure then allows to automatically detect the appropriate scalings for the driving forces that governs the evolution of the system. In our case, the are no mechanical loads and so what drives the system out of equilibrium is the presence of a fixed chemical potential on $\partial \mathcal{B}$. Indeed, the role of μ_* as a forcing term has already been established when introducing the loads power $\mathscr{P}_{\text{ext}}$ in Eq. (1.13). Following [Miara, 1994], the proper scalings for the loads are chosen so as to guarantee the solvability of the reduced equations, without any restrictions on the form of the loads themselves. In other words, we start by fixing an order of magnitude for μ_*, namely $\mu_* = \varepsilon^n \mu_*^{(n)}$ and select $n \in \mathbb{Z}$ such that $\mu_*^{(n)}$ appears in system of equations with lowest order in ε. We then check if the solvability conditions for such a system are met without any restrictions on the form of the function $\mu_*^{(n)}$. If the answer is negative, we restart the whole procedure by choosing $\mu_* = \varepsilon^{n+1} \mu_*^{(n+1)}$ and iterate until no restrictions are required for μ_*. As regards essential boundary conditions (in our case, the clamping condition $\mathbf{u} = 0$ on $\partial \mathcal{B}_{\mathbf{u}}$), we impose them on the lowest order term of the expansion in Eq. (1.29) which, according to the asymptotic procedure, is not identically zero. The details of the procedure are reported in the following.

We will frequently make use of the following proposition (see [Miara, 1994]):

Proposition 1. *Let u be a smooth function such that $\int_{\mathcal{B}} u \partial_3 v \, dx = 0 \quad \forall v \in V(\mathcal{B}) = \{v \text{ smooth s.t } v|_{\partial \mathcal{B}_{\mathbf{u}}} = 0\}$, then $u = 0$.*

Step 1 $\mathcal{O}(\frac{1}{\varepsilon^2})$

At this order, the only non trivial equations are Eq. (1.28c) and Eq. (1.28e), namely

$$\int_{\mathcal{B}} \phi \partial_t \partial_3 u_3^0 = 0 \quad \forall \phi \in V_\mu(\mathcal{B}),$$

$$\int_{\omega_+ \cup \omega_-} \mu_*^{(-2)} \psi_3 n_3 = 0 \quad \forall \psi_3 \in V_{\mathbf{h}}^3(\mathcal{B}),$$

from which we get respectively

$$\partial_t \partial_3 u_3^0 = 0, \qquad (1.30)$$

$$\mu_*^{(-2)} = 0 \quad \text{on } \omega_+ \cup \omega_-. \qquad (1.31)$$

Equation (1.31) is to be considered as a *compatibility condition* for the solution of the system, at this order in ε. Indeed, the only way to solve the problem is to choose as boundary conditions $\mu_* = \frac{1}{\varepsilon^2} \mu_*^{(-2)} = 0$. However, our goal, is to build a model whose solvability is independent on the choice of the function μ_*. Hence, we try with a different magnitude for μ_* and redo the whole procedure accordingly. It is evident that choosing $\mu_* = \varepsilon^n \mu_*^{(n)}$ with $n < -2$ would lead to the

same conclusions, requiring null chemical potential on the boundary. Hence we try $\mu_* = \mu_*^{(-1)}$ and observe that, with this new choice, no compatibility issues arise at this order since Eq. (1.31) is trivially satisfied.

Step 2 $\mathcal{O}(\frac{1}{\varepsilon})$

We first remark that, in absence of further information, $\mathbf{u}^0$ and u_3^0 are the first non zero terms of the asymptotic expansion and so, according to the procedure previously illustrated, must be endowed with the clamping conditions $\mathbf{u}^0 \in \mathbf{V_u}(\mathcal{B})$ and $u_3^0 \in V_{\mathbf{u}}^3(\mathcal{B})$.

Equation (1.28a) a this order leads to the following weak problem: find $u_3^0 \in V_{\mathbf{u}}^3(\mathcal{B})$ so that

$$\int_{\mathcal{B}} (1 + 2\eta) \partial_3 u_3^0 \partial_3 v_3 = 0 \quad \forall v_3 \in V_{\mathbf{u}}^3(\mathcal{B}). \tag{1.32}$$

The above equation, thanks to proposition (1), gives $u_3^0(x_1, x_2, x_3) = \bar{u}_3^0(x_1, x_2)$ with $\bar{u}_3^0 \in V_{\mathbf{u}}^3(\mathcal{B})$. Notice that, since u_3^0 is independent on x_3, equation (1.30) becomes automatically satisfied. Here, we seize the opportunity to introduce a useful notation by which, from now on, a superposed bar will designate functions independent on the transverse coordinate x_3.

Similarly, equation (1.28b) at this order amounts to searching for $\mathbf{u}^0 \in \mathbf{V_u}(\mathcal{B})$ so that

$$\int_{\mathcal{B}} \partial_3 \mathbf{u}^0 \cdot \partial_3 \mathbf{v} = 0 \quad \forall \mathbf{v} \in \mathbf{V_u}(\mathcal{B}), \tag{1.33}$$

which again implies $\mathbf{u}^0 = \bar{\mathbf{u}}^0$ for some $\bar{\mathbf{u}}^0 \in \mathbf{V_u}(\mathcal{B})$, independent on x_3. As regards equation (1.28c), we have

$$\int_{\mathcal{B}} \phi \partial_t \left(\partial_3 u_3^1 + \operatorname{tr} \mathbf{E}(\mathbf{u}^0) \right) = 0 \quad \forall \phi \in V_\mu. \tag{1.34}$$

Finally, equation (1.28e) leads to

$$\int_{\omega_+ \cup \omega_-} \mu_*^{(-1)} \psi_3 n_3 = 0 \quad \forall \psi_3 \in V_{\mathbf{h}}^3(\mathcal{B}), \tag{1.35}$$

which again implies the compatibility condition $\mu_*^{(-1)} = 0$ on $\omega_+ \cup \omega_-$. The same considerations made at the previous step are valid and consequently we need to redo the procedure with the new assumption $\mu_* = \mu_*^{(0)}$. We remark that, a physical interpretations can be given to these *compatibility conditions*: a plate of thickness ε can not withstand loads with magnitudes $\mu_* = \frac{1}{\varepsilon^2}\mu_*^{(-2)}$ and $\mu_* = \frac{1}{\varepsilon}\mu_*^{(-1)}$ since, in the limit when $\varepsilon \to 0$, the plate is too thin to react to such loads and reach an equilibrium state.

Step 3 $\mathcal{O}(1)$

By exploiting the information gathered at previous order, we can write the equations for the displacement at $\mathcal{O}(1)$ as follows

$$\int_{\mathcal{B}} (1 + 2\eta) \partial_3 u_3^1 \partial_3 v_3 = - \int_{\mathcal{B}} \left(\operatorname{tr} \mathbf{E}(\bar{\mathbf{u}}^0) - \eta \mu^0 \right) \partial_3 v_3 \quad \forall v_3 \in V_{\mathbf{u}}^3(\mathcal{B}), \tag{1.36}$$

$$\int_{\mathcal{B}} \partial_3 \mathbf{u}^1 \cdot \partial_3 \mathbf{v} = \int_{\mathcal{B}} \nabla \bar{u}_3^0 \cdot \partial_3 \mathbf{v} \quad \forall \mathbf{v} \in \mathbf{V_u}(\mathcal{B}), \tag{1.37}$$

$$\int_{\mathcal{B}} \phi \left(\frac{1+2\eta}{\eta} \partial_t \partial_3 u_3^2 + \frac{1+2\eta}{\eta} \partial_t \mathrm{tr} \mathbf{E}(\mathbf{u}^1) + \partial_3 h_3^0 \right) = 0 \ \ \forall \phi \in V_\mu(\mathcal{B}), \tag{1.38}$$

$$\int_{\mathcal{B}} \mu^0 \partial_3 \psi_3 = \int_{\omega_+ \cup \omega_-} \mu_*^{(0)} \psi_3 n_3 \ \ \forall \psi_3 \in V_{\mathbf{h}}^3(\mathcal{B}). \tag{1.39}$$

In order to derive solvability conditions for the above equations, let us test Eq. (1.39) with $\psi_3 \in C_c^\infty(\mathcal{B})$ and get

$$\int_{\omega_+ \cup \omega_-} \mu^0 \partial_3 \psi_3 = 0 \ \ \forall \psi_3 \in C_c^\infty(\mathcal{B}),$$

which, after integration by parts, implies $\mu^0 = \bar{\mu}^0$ for some $\bar{\mu}^0 \in V_\mu(\mathcal{B})$, independent on x_3. Consequently, Eq. (1.39) leads to

$$\int_{\mathcal{B}} \bar{\mu}^0 \partial_3 \psi_3 = \int_{\omega_+ \cup \omega_-} \mu_*^{(0)} \psi_3 n_3 \ \ \forall \psi_3 \in V_{\mathbf{h}}^3(\mathcal{B}), \tag{1.40}$$

which tested with functions ψ_3 independent on x_3 gives

$$\int_{\omega_+ \cup \omega_-} \mu_*^{(0)} \psi_3 n_3 = 0 \ \ \forall \psi_3 \in \bar{V}_{\mathbf{h}}^3(\mathcal{B}), \tag{1.41}$$

where $\bar{V}_{\mathbf{h}}^3(\mathcal{B}) = \{\psi_3 \in V_{\mathbf{h}}^3(\mathcal{B}) \text{ s.t } \partial_3 \psi_3 = 0\}$. If we denote with μ_*^+ and μ_*^- the values of μ_* on ω^+ and ω^-, respectively, then Eq. (1.41) can be rewritten as

$$\int_{\omega_+} \mu_*^{(0)+} \psi_3 n_3 + \int_{\omega_-} \mu_*^{(0)-} \psi_3 n_3 = 0 \ \ \forall \psi_3 \in \bar{V}_{\mathbf{h}}^3(\mathcal{B}). \tag{1.42}$$

Finally, we observe that Eq. (1.42) can be rewritten as

$$\int_\omega (\mu_*^{(0)+} - \mu_*^{(0)-})\psi_3 = 0 \ \ \forall \psi_3 \in V_{\mathbf{h}}^3(\omega),$$

where $V_{\mathbf{h}}^3(\omega) = \{\psi_3 \text{ smooth on } \omega\}$ and, with a little abuse of notation, $\mu_*^{(0)\pm}$ denotes the values of $\mu_*|_{\omega^\pm}$ projected onto the mid-plane ω. Hence, the above equation implies the following compatibility condition

$$\mu_*^{(0)+} - \mu_*^{(0)-} = 0 \text{ on } \omega. \tag{1.43}$$

As for the physical meaning of the above equation, we notice that, having $\mu_*^{(0)+} \neq \mu_*^{(0)-}$ generates a bending moment deflecting the plate perpendicular to the mid-plane ω. Hence, the condition in Eq. (1.43) assert that, in the limit when $\varepsilon \to 0$, a plate of thickness ε cannot withstand a bending moment with intensity of order ε^0 since it is too thin for contrasting the external loads with some internal reaction. The only way to reach equilibrium is in absence of such external bending moment.

As usual, our aim is to chose an asymptotic regime where no restrictions on the loads are required. So let us try with $\mu_* = \varepsilon \mu_*^{(1)}$. Equation (1.40) becomes

$$\int_{\mathcal{B}} \mu^0 \partial_3 \psi_3 = 0 \ \ \forall \psi_3 \in V_{\mathbf{h}}^3(\mathcal{B}),$$

which trivially implies $\mu^0 = 0$. Hence, equations (1.36) and (1.37) lead to

$$\mathbf{u}^1 = \bar{\mathbf{u}}^1 - x_3 \nabla \bar{u}_3^0, \tag{1.44}$$

$$u_3^1 = \bar{u}_3^1 - x_3 \frac{1}{1+2\eta} \mathrm{tr} \mathbf{E}(\bar{\mathbf{u}}^0), \tag{1.45}$$

reproducing the classical Kirchhoff-Love kinematics for linear plates [Timoshenko et al., 1959]. Finally, Eq. (1.38) trivially localizes into

$$\frac{1+2\eta}{\eta} \left(\partial_t \partial_3 u_3^2 + \partial_t \mathrm{tr} \mathbf{E}(\mathbf{u}^1) \right) + \partial_3 h_3^0 = 0. \tag{1.46}$$

Step 4 $\mathcal{O}(\varepsilon)$

Exploiting the results at previous steps, the equations in (1.28) at order $\mathcal{O}(\varepsilon)$ are:

$$\int_{\mathcal{B}} (1+2\eta) \partial_3 u_3^2 \partial_3 v_3 = -\int_{\mathcal{B}} \left(\mathrm{tr} \mathbf{E}(\mathbf{u}^1) - \eta \mu^1 \right) \partial_3 v_3 \quad \forall v_3 \in V_{\mathbf{u}}^3(\mathcal{B}), \tag{1.47}$$

$$\int_{\mathcal{B}} \eta \partial_3 \mathbf{u}^2 \cdot \partial_3 \mathbf{v} = -\int_{\mathcal{B}} \mathrm{tr} \mathbf{E}(\bar{\mathbf{u}}^0) \mathrm{tr} \mathbf{E}(\mathbf{v}) + 2\eta \mathbf{E}(\bar{\mathbf{u}}^0) \cdot \mathbf{E}(\mathbf{v}) +$$
$$- \int_{\mathcal{B}} \partial_3 u_3^1 \mathrm{tr} \mathbf{E}(\mathbf{v}) + \eta \nabla u_3^1 \cdot \partial_3 \mathbf{v} \quad \forall \mathbf{v} \in \mathbf{V}_{\mathbf{u}}(\mathcal{B}), \tag{1.48}$$

$$\int_{\mathcal{B}} \left(\frac{1+2\eta}{\eta} \partial_t \partial_3 u_3^1 - \partial_3 h_3^1 \right) \phi = -\int_{\mathcal{B}} \left(\frac{1+2\eta}{\eta} \partial_t \mathrm{tr} \mathbf{E}(\bar{\mathbf{u}}^0) - \mathrm{div}\, \mathbf{h}^0 \right) \phi \quad \forall \phi \in V_{\mu}(\mathcal{B}), \tag{1.49}$$

$$\int_{\mathcal{B}} -\mathbf{h}^0 \cdot \boldsymbol{\psi} = 0 \quad \forall \boldsymbol{\psi} \in \mathbf{V}_{\mathbf{h}}(\mathcal{B}). \tag{1.50}$$

$$\int_{\mathcal{B}} -h_3^0 \psi_3 + \mu^1 \partial_3 \psi_3 = \int_{\omega_+ \cup \omega_-} \mu_*^{(1)} \psi_3 n_3 \quad \forall \psi_3 \in V_{\mathbf{h}}^3(\mathcal{B}). \tag{1.51}$$

Notice that we have omitted the equation coming from Eq. (1.28b) and Eq. (1.28c) since they won't play any role in the following considerations.

From Eq. (1.47) we get

$$\partial_3 u_3^2 = -\frac{1}{1+2\eta} \mathrm{tr} \mathbf{E}(\mathbf{u}^1) + \frac{\eta \mu^1}{(1+2\eta)}. \tag{1.52}$$

Moreover, consider equation (1.51), integrate it by parts and obtain the following variational equation

$$\int_{\mathcal{B}} - \left(h_3^0 + \partial_3 \mu^1 \right) \psi_3 = \int_{\omega_+ \cup \omega_-} (\mu_*^{(1)} - \mu^1) \psi_3 n_3 \quad \forall \psi_3 \in V_{\mathbf{h}}^3,$$

which upon localization gives

$$\begin{cases} h_3^0 = -\partial_3 \mu^1 & \text{on } \mathcal{B}, \\ \mu^1 = \mu_*^{(1)} & \text{on } \omega_+ \cup \omega_-. \end{cases} \tag{1.53}$$

If now we plug Eqs. (1.52), (1.53) and (1.44) into Eq. (1.38) we obtain

$$\partial_t \mu^1 - \partial_{33}\mu^1 = -2\left(\partial_t \mathrm{tr}\mathbf{E}(\bar{\mathbf{u}}^1) + x_3\partial_t \mathrm{tr}\mathbf{K}(\bar{u}_3^0)\right), \tag{1.54}$$

where we have defined $\mathbf{K}(v_3) := -\nabla\nabla v_3$ as the linearized curvature of the mid-surface of the plate.

Let us now consider Eq. (1.48) and test it for $\mathbf{v} \in \bar{\mathbf{V}}_{\mathbf{u}}(\mathcal{B}) = \{\mathbf{v} \in \mathbf{V}_{\mathbf{u}}(\mathcal{B}) \text{ s.t } \partial_3\mathbf{v} = 0\}$. We get

$$\int_\mathcal{B} \mathrm{tr}\mathbf{E}(\bar{\mathbf{u}}^0)\mathrm{tr}\mathbf{E}(\mathbf{v}) + 2\eta\mathbf{E}(\bar{\mathbf{u}}^0)\cdot\mathbf{E}(\mathbf{v}) + \partial_3 u_3^1 \mathrm{tr}\mathbf{E}(\mathbf{v}) = 0 \quad \forall\mathbf{v} \in \bar{\mathbf{V}}_{\mathbf{u}}(\mathcal{B}).$$

Then, substitute Eq. (1.45) into the above equation, integrate along x_3 and obtain the following variational problem: find $\bar{\mathbf{u}}^0 \in \mathbf{V}_{\mathbf{u}}(\omega)$ such that

$$\int_\omega \frac{2\eta}{1+2\eta}\mathrm{tr}\mathbf{E}(\bar{\mathbf{u}}^0)\mathrm{tr}\mathbf{E}(\mathbf{v}) + 2\eta\mathbf{E}(\bar{\mathbf{u}}^0)\cdot\mathbf{E}(\mathbf{v}) = 0 \quad \forall\mathbf{v} \in \mathbf{V}_{\mathbf{u}}(\omega),$$

where $\mathbf{V}_{\mathbf{u}}(\omega) := \{\mathbf{v} \text{ smooth on } \omega \text{ s.t } \mathbf{v}|_{\partial\omega_{\mathbf{u}}} = 0\}$. However, by testing with $\mathbf{v} = \bar{\mathbf{u}}^0$, it is immediate to see that the above equation is uniquely solved by the trivial solution $\bar{\mathbf{u}}^0 = 0$. Because of this fact, we deduce from Eq. (1.45) that $u_3^1 = \bar{u}_3^1$ and consequently that Eq. (1.34) gets trivially satisfied. As for Eq. (1.50), we trivially get $\mathbf{h}^0 = 0$.

We finally remark that, as a consequence of the calculations above, $\mathbf{u}^0 = 0$, and hence $\mathbf{u}^1$ becomes the lowest order term in the asymptotic expansion which *a priori* is different from zero. Hence, we impose the clamping conditions $\mathbf{u}^1 \in \mathbf{V}_{\mathbf{u}}(\mathcal{B})$. Notice that, thanks to the condition $u_3^0 \in V_{\mathbf{u}}^3(\mathcal{B})$ and the characterization of $\mathbf{u}^1$ expressed in Eq. (1.44), the boundary conditions on $\mathbf{u}^1$ transfer to $\bar{\mathbf{u}}^1$ and $\bar{u}_3^0$ thus leading to

$$\bar{\mathbf{u}}^1 = 0, \quad \nabla\bar{u}_3^0 \cdot \mathbf{n} = 0 \text{ on } \partial\mathcal{B}_{\mathbf{u}}.$$

The above conditions must then be embedded into the functional spaces as follows

$$\bar{\mathbf{u}}^1 \in \mathbf{V}_{\mathbf{u}}(\mathcal{B}), \quad \bar{u}_3^0 \in \tilde{V}_{\mathbf{u}}^3(\mathcal{B}) := \{v \in V_{\mathbf{u}}^3(\mathcal{B}) \text{ s.t } \nabla v_3 \cdot \mathbf{n}|_{\partial\mathcal{B}_{\mathbf{u}}} = 0\}.$$

Step 5 $\mathcal{O}(\varepsilon^2)$

As it will be clear at the end of the section, the only relevant equations at this order are the ones coming from Eq. (1.28b) and Eq. (1.28d), namely

$$\int_\mathcal{B} \left(\mathrm{tr}\mathbf{E}(\mathbf{u}^1) + \partial_3 u_3^2 - \eta\mu^1\right)\mathrm{tr}\mathbf{E}(\mathbf{v}) + 2\eta\mathbf{E}(\mathbf{u}^1)\cdot\mathbf{E}(\mathbf{v}) + \eta\left(\nabla u_3^2 + \partial_3\mathbf{u}^3\right)\cdot\partial_3\mathbf{v} \quad \forall\mathbf{v} \in \mathbf{V}_{\mathbf{u}}(\mathcal{B}), \tag{1.55}$$

$$\int_\mathcal{B} \mu^1 \mathrm{div}\,\psi - \int_\mathcal{B} \mathbf{h}^1 \cdot \psi = \int_{\partial\mathcal{B}} \mu_*^{(1)}\psi \cdot \mathbf{n} \quad \forall\psi \in \mathbf{V}_{\mathbf{h}}(\mathcal{B}). \tag{1.56}$$

Now, test Eq. (1.55) for $\mathbf{v} \in \bar{\mathbf{V}}_{\mathbf{u}}(\mathcal{B})$ and get

$$\int_\mathcal{B} \left(\mathrm{tr}\mathbf{E}(\mathbf{u}^1) + \partial_3 u_3^2 - \eta\mu^1\right)\mathrm{tr}\mathbf{E}(\mathbf{v}) + 2\eta\mathbf{E}(\mathbf{u}^1)\cdot\mathbf{E}(\mathbf{v}) \quad \forall\mathbf{v} \in \bar{\mathbf{V}}_{\mathbf{u}}(\mathcal{B}).$$

Then, substitute equations (1.52) and (1.44) into the above one and integrate along the variable x_3. We obtain the following variational problem: find $\bar{\mathbf{u}}^1 \in \mathbf{V_u}(\omega)$ such that

$$\int_\omega \left(\frac{2\eta}{1+2\eta} \text{tr}\mathbf{E}(\bar{\mathbf{u}}^1) - \frac{2\eta^2}{1+2\eta} N_\mu^1 \right) \text{tr}\mathbf{E}(\mathbf{v}) + 2\eta\mathbf{E}(\bar{\mathbf{u}}^1) \cdot \mathbf{E}(\mathbf{v}) = 0 \quad \forall \mathbf{v} \in \mathbf{V_u}(\omega), \tag{1.57}$$

where we have defined: $N_\mu^1 = \int_{-1/2}^{1/2} \mu^1 \mathrm{d}x_3$. Then plug Eq. (1.57) into Eq. (1.55) and get the following equation that will be useful in the last step

$$\int_\mathcal{B} \left(-\frac{2\eta}{1+2\eta} \text{tr}\mathbf{E}(\bar{\mathbf{u}}^1) + \frac{2\eta}{1+2\eta} x_3 \text{tr}\mathbf{K}(\bar{u}_3^0) - \frac{2\eta^2}{1+2\eta}(\mu^1 - N_\mu^1) \right) \text{tr}\mathbf{E}(\mathbf{v}) +$$
$$-\eta \left(2\mathbf{E}(\bar{\mathbf{u}}^1) - 2x_3\mathbf{K}(\bar{u}_3^0) \right) \cdot \mathbf{E}(\mathbf{v}) + \eta \left(\nabla u_3^2 + \partial_3\mathbf{u}^3 \right) \cdot \partial_3\mathbf{v} = 0 \quad \forall \mathbf{v} \in \mathbf{V_u}(\mathcal{B}). \tag{1.58}$$

Finally, Eq. (1.56) leads, after integration by parts, to $\mathbf{h}^1 = -\nabla\mu^1$ together with the condition $\mu^1 = \mu_*^{(1)}$ on $\partial\mathcal{B} \setminus (\omega^+ \cup \omega^-)$.

Step 6 $\mathcal{O}(\varepsilon^3)$

Equation (1.28a) leads to

$$\int_\mathcal{B} \left((1+2\eta)\partial_3 u_3^4 + \text{tr}\mathbf{E}(\mathbf{u}^3) - \eta\mu^3 \right) \partial_3 v_3 + \int_\mathcal{B} \eta \left(\nabla u_3^2 + \partial_3\mathbf{u}^3 \right) \cdot \nabla v_3 = 0 \quad \forall v_3 \in V_\mathbf{u}^3(\mathcal{B}), \tag{1.59}$$

which tested upon functions in $\bar{V}_\mathbf{u}^3(\mathcal{B}) = \{v_3 \in V_\mathbf{u}^3(\mathcal{B}) \text{ s.t } \partial_3 v_3 = 0\}$ leads to

$$\int_\mathcal{B} \left(\nabla u_3^2 + \partial_3\mathbf{u}^3 \right) \cdot \nabla v_3 = 0 \quad \forall v_3 \in \bar{V}_\mathbf{u}^3(\mathcal{B}). \tag{1.60}$$

Now plug Eq. (1.60) into Eq. (1.58) and test the resulting equation for functions of the form $\mathbf{v} = -x_3\nabla\eta_3$ with $\eta_3 \in \tilde{V}_\mathbf{u}^3(\mathcal{B}) \cap \bar{V}_\mathbf{u}^3(\mathcal{B})$ (notice that such a $\mathbf{v}$ belongs to $\mathbf{V_u}(\mathcal{B})$). We get

$$\int_\mathcal{B} \left(-\frac{2\eta}{1+2\eta} x_3^2 \text{tr}\mathbf{K}(\bar{u}_3^0) + x_3 \frac{2\eta^2}{1+2\eta}(\mu^1 - N_\mu^1) \right) \text{tr}\mathbf{K}(\eta_3) +$$
$$-2\eta x_3^2 \mathbf{K}(\bar{u}_3^0) \cdot \mathbf{K}(\eta_3) = 0 \quad \forall \eta_3 \in \tilde{V}_\mathbf{u}^3(\mathcal{B}) \cap \bar{V}_\mathbf{u}^3(\mathcal{B}).$$

Finally, integrate the above equation on x_3 and rename η_3 with v_3 to obtain the following variational problem: Find $\bar{u}_3^0 \in V_\mathbf{u}^3(\omega)$ so that

$$\int_\omega \left(\frac{1}{12}\frac{2\eta}{1+2\eta}\text{tr}\mathbf{K}(\bar{u}_3^0) - \frac{2\eta^2}{1+2\eta}M_\mu^1 \right) \text{tr}\mathbf{K}(v_3) + \frac{2\eta}{12}\mathbf{K}(\bar{u}_3^0) \cdot \mathbf{K}(v_3) = 0 \quad \forall v_3 \in V_\mathbf{u}^3(\omega), \tag{1.61}$$

where: $V_\mathbf{u}^3(\omega) := \{v \in \text{ smooth on } \omega \text{ s.t } \nabla v_3|_{\partial\omega_\mathbf{u}} = 0\}$ and $M_\mu^1 = \int_{-1/2}^{1/2} \mu^1 x_3 \,\mathrm{d}x_3$.

In light of the derived equations, we finally remark that the boundary conditions for μ on $\partial\mathcal{B} \setminus (\omega^+ \cup \omega^-)$ cannot in general be met unless some very peculiar μ_* is chosen. The mathematical reason for this can be understood by looking at equations (1.57), (1.61) and (1.54) according to which, boundary conditions on $\omega^+ \cup \omega^-$ are sufficient to uniquely determine μ on $\mathcal{B}$. Physically, we expect the presence a boundary layer on $\partial\mathcal{B} \setminus (\omega^+ \cup \omega^-)$ that our reduced model is not able to capture.

The final equations The set of equations for the Kirchhoff poroelastic plate is composed of Eqs. (1.57), (1.61) and (1.54), expressing the balance of forces, moments and mass, respectively. They can be conveniently recast in a more compact and expressive way as follows. As regards the balance of forces and moments we get, upon localization, the following equations defined on ω:

$$\operatorname{div}\mathbf{N} = 0\,, \qquad \operatorname{div}\operatorname{div}\mathbf{M} = 0\,, \tag{1.62}$$

where the tensors $\mathbf{N}$ and $\mathbf{M}$ are the dimensionless force and moment resultants along the thickness, respectively. They are related to the in-plane strain $\mathbf{E} = \operatorname{Sym}\nabla\mathbf{u}$ and curvature $\mathbf{K} = -\nabla\nabla u_3$ tensors via the constitutive equations[2]

$$\mathbf{N} = \mathbb{C}\mathbf{E} - \frac{\eta}{1+2\eta}N_\mu\,\mathbf{I}\,, \tag{1.63a}$$

$$\mathbf{M} = \varepsilon\,\mathbb{C}\mathbf{K} - \frac{12\eta}{1+2\eta}M_\mu\mathbf{I}\,. \tag{1.63b}$$

where N_μ and M_μ read

$$N_\mu = \int_{-\frac{1}{2}}^{\frac{1}{2}} \mu\,\mathrm{d}x_3\,, \qquad M_\mu = \int_{-\frac{1}{2}}^{\frac{1}{2}} \mu\,x_3\mathrm{d}x_3\,, \tag{1.64}$$

while $\mathbb{C} = \mathbf{I} \boxtimes \mathbf{I} + \frac{1}{1+2\eta}\mathbf{I} \otimes \mathbf{I}$ is the symmetric, positive definite elasticity tensor. In the following Sections we will consider a free standing plate so that no clamping conditions are imposed at the boundary. The traction-free boundary conditions, naturally arising from localization of Eq. (1.57) and Eq. (1.61), can then be written as

$$\mathbf{N}\mathbf{n} = 0\,, \qquad \mathbf{M}\mathbf{n} \cdot \mathbf{n} = 0\,, \qquad \operatorname{div}\mathbf{M} \cdot \mathbf{n} + \nabla\left(\mathbf{M}\mathbf{n} \cdot \mathbf{t}\right) \cdot \mathbf{t} = 0 \ \ \text{on } \omega,$$

where, $\mathbf{n}$ and $\mathbf{t}$ are the unit normal and tangent to $\partial\omega$, respectively. As for the balance of solvent mass, localization of Eq. (1.54) leads to the following equation defined on $\mathcal{B}$

$$\partial_t\mu - \partial_{33}\mu = -2\left(\partial_t\operatorname{tr}\mathbf{E} + x_3\varepsilon\,\partial_t\operatorname{tr}\mathbf{K}\right)\,. \tag{1.65}$$

We will consider a plate immersed into a solvent bath, and so, as already anticipated, Dirichlet boundary conditions are imposed on the top and bottom faces of the plate, namely $\mu = \mu_*^+$ (resp. $\mu = \mu_*^-$) on ω^+ (resp. ω^-). As for the initial conditions, we assume zero chemical potential and displacement. We will refer to the set of equations (1.62)-(1.65) and corresponding initial and boundary conditions as the Fully Coupled Problem (FCP). For later use, we also recast the weak form of the equations in the following way: find $\bar{\mathbf{u}}^1 \in \mathbf{V_u}(\omega)$, $\bar{u}_3^0 \in V_{\mathbf{u}}^3(\omega)$ and $\mu \in V_\mu(\mathcal{B})$ so that

$$\int_\omega \mathbb{C}\mathbf{E}(\mathbf{u}) \cdot \mathbf{E}(\mathbf{v}) = \frac{\eta}{1+2\eta}\int_\omega N_\mu\operatorname{tr}\mathbf{E}(\mathbf{v}) \qquad \forall\mathbf{v} \in \mathbf{V_u}(\omega), \tag{1.66a}$$

$$\varepsilon\int_\omega \mathbb{C}\mathbf{K}(u_3) \cdot \mathbf{K}(v_3) = \frac{12\eta}{1+2\eta}\int_\omega M_\mu\operatorname{tr}\mathbf{K}(v_3) \qquad \forall v_3 \in V_{\mathbf{u}}^3(\omega), \tag{1.66b}$$

$$\int_\omega \partial_t\mu\phi + \partial_3\mu\partial_3\phi = -\int_\omega 2\left(\partial_t\operatorname{tr}\mathbf{E}(\mathbf{u}) + x_3\varepsilon\partial_t\operatorname{tr}\mathbf{K}(u_3)\right)\phi \qquad \forall\mu \in V_\mu^{\mathrm{dir}}(\mathcal{B}), \tag{1.66c}$$

where $V_\mu^{\mathrm{dir}}(\mathcal{B}) = \{\phi \in V_\mu(\mathcal{B}) \text{ s.t. } \phi = 0 \text{ on } \omega^\pm\}$.

---

[2]Recall that, according to the asymptotic expansion in Eq. (1.29), we have the following relations: $\mathbf{u} = \varepsilon\bar{\mathbf{u}}^1$, $u_3 = \bar{u}_3^0$ and $\mu = \varepsilon\mu^1$

1.4 Properties of the solution

In this Section, we discuss the properties of the solution to the FCP. First, it is easy to check that the dimensional reduction illustrated above can be performed, with almost identical steps, even in the case of a free standing plate. The only difference is that the solution of the final equations is unique only up to infinitesimal isometries, as shown in the following

Proposition 2. *Assume a smooth solution* $(\mu, \mathbf{u}, u_3)$ *to (FCP) exists. Then μ is unique, while $\mathbf{u}$ and u_3 are unique up to an infinitesimal rigid displacement (i.e. if $(\mu, \mathbf{u}', u_3')$ is another solution for (FCP) then $(\mathbf{u}', u_3') = (\mathbf{u}, u_3) + a + b \wedge (\mathbf{x}, x_3)$ for some $a, b \in \mathbb{R}^3$).*

Proof. Let $(\mu^{(1)}, \mathbf{u}^{(1)}, u_3^{(1)})$, $(\mu^{(2)}, \mathbf{u}^{(2)}, u_3^{(2)})$ be two solutions of (FCP) and define the new variables $(\mu, \mathbf{u}, u_3) := (\mu^{(1)}, \mathbf{u}^{(1)}, u_3^{(1)}) - (\mu^{(2)}, \mathbf{u}^{(2)}, u_3^{(2)})$. Then by linearity $(\mu, \mathbf{u}, u_3)$ solves again (FCP) with boundary conditions $\mu_*^+ = \mu_*^- = 0$ and everywhere null initial conditions. Consider Eq. (1.65) and integrate it in time:

$$\mu(t) - \int_0^t \partial_{33} \mu(\tau) \mathrm{d}\tau = -2(\mathrm{tr}\mathbf{E} + x_3 \varepsilon \mathrm{tr}\mathbf{K}). \tag{1.67}$$

Multiply Eq. (1.67) by μ and integrate on $\mathcal{B} = \omega \times [-\frac{1}{2}, \frac{1}{2}]$:

$$\int_{\mathcal{B}} \mu(t)^2 - \int_{\mathcal{B}} \left(\mu(t) \int_0^t \partial_{33} \mu(\tau) \mathrm{d}\tau \right) = 2 \int_\omega M_\mu(t) \mathrm{tr}\mathbf{K}(t) + N_\mu(t) \mathrm{tr}\mathbf{E}(t). \tag{1.68}$$

Now observe that

$$\int_{\mathcal{B}} \left(\mu(t) \int_0^t \partial_{33} \mu(\tau) \mathrm{d}\tau \right) = - \int_{\mathcal{B}} \left(\partial_3 \mu(t) \int_0^t \partial_3 \mu(\tau) \mathrm{d}\tau \right) \tag{1.69}$$

$$= - \int_{\mathcal{B}} \frac{1}{2} \frac{\mathrm{d}}{\mathrm{d}t} \left(\int_0^t \partial_3 \mu(\tau) \mathrm{d}\tau \right)^2.$$

Substitute Eq. (1.69) into Eq. (1.68) and integrate in time in the interval $\mathscr{T} = [0, t]$:

$$\int_{\mathcal{B} \times \mathscr{T}} \mu^2 + \int_{\mathcal{B}} \frac{1}{2} \left(\int_0^t \partial_3 \mu(\tau) \mathrm{d}\tau \right)^2 = 2 \int_{\omega \times \mathscr{T}} M_\mu(t) \mathrm{tr}\mathbf{K}(t) + N_\mu(t) \mathrm{tr}\mathbf{E}(t) \geq 0. \tag{1.70}$$

Test Eq. (1.66a) and Eq. (1.66b), on the solutions $\mathbf{u}$ and u_3:

$$\int_\omega \mathbb{C}\mathbf{E} \cdot \mathbf{E} = -\frac{\eta}{1 + 2\eta_1} \int_\omega N_\mu \mathrm{tr}\mathbf{E} \tag{1.71a}$$

$$\frac{\varepsilon}{12} \int_\omega \mathbb{C}\mathbf{K} \cdot \mathbf{K} = -\frac{\eta}{1 + 2\eta_1} \int_\omega M_\mu \mathrm{tr}\mathbf{K}. \tag{1.71b}$$

Finally, sum Eq. (1.71) with Eq. (1.72), integrate over $\mathscr{T}$ and get the chain of inequalities

$$0 \leq \int_{\omega \times \mathscr{T}} \mathbb{C}\mathbf{E} \cdot \mathbf{E} + \frac{\varepsilon}{12} \int_{\omega \times \mathscr{T}} \mathbb{C}\mathbf{K} \cdot \mathbf{K} =$$

$$= -\frac{\eta}{1 + 2\eta_1} \left(\int_{\omega \times \mathscr{T}} M_\mu(t) \mathrm{tr}\mathbf{K}(t) + N_\mu(t) \mathrm{tr}\mathbf{E}(t) \right) \leq 0, \tag{1.72}$$

where the inequality on the right follows from the positive definiteness of $\mathbb{C}$, while the one on the left follows from Eq. (1.70). Hence, Eq. (1.72) becomes an equality and from Eq. (1.70) we deduce that $\mu \equiv 0$. This fact implies that $N_\mu = M_\mu = 0$, which forces the conditions $\mathbf{E} \equiv 0$ and $\mathbf{K} \equiv 0$. Null strain and null curvature imply that the solution $(\mathbf{u}, u_3)$ is an infinitesimal rigid displacement (see [Ciarlet et al., 2008]). □

Let us now consider another property that follows from the linearity of the model. Define $\mu_m = (\mu_\star^+ + \mu_\star^-)/2$ and $\mu_d = (\mu_\star^+ - \mu_\star^-)/2$, then the solution is such that

$$\mathbf{E} = \mathscr{P}[\mu_m], \quad \mathbf{K} = \mathscr{Q}[\mu_d], \tag{1.73}$$

where $\mathscr{P}[\cdot]$ and $\mathscr{Q}[\cdot]$ are two linear operators.

To prove this result, observe that $\mu_\star^+ = \mu_m + \mu_d$ and that $\mu_\star^- = \mu_m - \mu_d$. Hence, by the linearity of the governing equations, the solution $\psi = (\mu, \mathbf{E}, \mathbf{K})$ can be written as the sum of $\psi_e = (\mu_e, \mathbf{E}_e, \mathbf{K}_e)$ and $\psi_o = (\mu_o, \mathbf{E}_o, \mathbf{K}_o)$, which are two solutions of FCP but with boundary conditions for the chemical potential replaced by $\mu_\star^\pm = \mu_m$ and $\mu_\star^\pm = \pm\mu_d$, respectively. We claim that ψ_e is such that $\mathbf{K}_e = 0$ and μ_e is an even function of x_3. Indeed, one may observe that the list $\bar{\psi}_e = (\bar{\mu}_e, \mathbf{E}_e, -\mathbf{K}_e)$, with $\bar{\mu}_e(\mathbf{x}, x_3, t) = \mu_e(\mathbf{x}, -x_3, t)$, is a solution corresponding to $\mu_\star^\pm = \mu_m$. Uniqueness of the solution implies that $\psi_e = \bar{\psi}_e$, so that the claim follows. Likewise, by considering the list $\bar{\psi}_o = (\bar{\mu}_o, -\mathbf{E}_o, \mathbf{K}_o)$, with $\bar{\mu}_o(\mathbf{x}, x_3, t) = -\mu_o(\mathbf{x}, -x_3, t)$, one can prove that ψ_o is such that $\mathbf{E}_o = 0$ and μ_o is an odd function of x_3. Hence, $\mathbf{E} = \mathbf{E}_e + \mathbf{E}_o = \mathbf{E}_e = \mathscr{P}[\mu_m]$ and $\mathbf{K} = \mathbf{K}_e + \mathbf{K}_o = \mathbf{K}_o = \mathscr{Q}[\mu_d]$. The linearity of $\mathscr{P}[\cdot]$ and of $\mathscr{Q}[\cdot]$ follows from that of the governing equations.

The result of Eq. (1.73) reveals that the dynamics of the in-plane strain and curvature can be made independent through a suitable choice of the boundary conditions on the chemical potential. This means that $\mu_\star^+$ and $\mu_\star^-$ can be chosen so as to select any of the admissible evolutions of in-plane strain and curvature corresponding to given values of μ_m and μ_d, respectively. Consequently, there is no mutual influence between strain and curvature dynamics, a feature of interest in the context of the shape control of thin plates. However, we remark that this decoupled response is not expected to occur in the context of non-linear theories. First, metric and curvature are independent entities only in the linear approximation. Indeed it is well known from classical results of the differential geometry of surfaces that, changes in the plate metric may induce changes in curvature. More in general, we observe that the result in Eq. (1.73) strongly rely upon three main ingredients: uniqueness of the solution, linearity and symmetry of the equations. Whenever one of them is missing, such in the case of nonlinear bifurcating mechanical models, we may expect a non trivial interplay between planar and transverse deformations.

Coupling between solvent diffusion and strain We finally discuss how curvature and strains are coupled with the diffusion dynamics. In particular, we investigate whether it is possible to have a non trivial evolution of the chemical potential, which is independent from the one of the strains. According to Eq. (1.65), given the null initial conditions for the displacement field, we have that, the only case where the diffusion process decouples from the deformation of the plate, is when both $\mathrm{tr}\mathbf{E}$ and $\mathrm{tr}\mathbf{K}$ vanishes throughout the evolution. We remark that, the former is the incremental areal increase δA, while latter represents the incremental mean curvature of the plate δH, namely

$$\delta A = \mathrm{tr}\mathbf{E}, \quad \delta H = \mathrm{tr}\mathbf{K}.$$

Hence, the problem reformulates into finding non trivial solutions by which the plate deforms preserving its zero mean curvature and its area. It is easy to show that such solutions do not exists, and the argument leading to that conclusion entirely relies on mechanical considerations. Indeed, consider the weak formulation in equations (1.66a)-(1.66b) and test it on the solution $\mathbf{u}$, u_3

$$\int_\omega \mathbb{C}\mathbf{E} \cdot \mathbf{E} = \frac{\eta}{1 + 2\eta} \int_\omega N_\mu \mathrm{tr}\mathbf{E},$$

$$\varepsilon \int_\omega \mathbb{C}\mathbf{K} \cdot \mathbf{K} = \frac{12\eta}{1 + 2\eta} \int_\omega M_\mu \mathrm{tr}\mathbf{K}.$$

From the above equation we immediately see that if $\mathrm{tr}\mathbf{K} = \mathrm{tr}\mathbf{E} \equiv 0$ then, due to the positive definiteness of $\mathbb{C}$, both $\mathbf{E}$ and $\mathbf{K}$ vanishes and so, up to infinitesimal isometries, $\mathbf{u}$ and u_3 also do. This means that the evolution of μ is necessarily coupled to the curvature and the planar metric of the plate trough δH and δA, respectively. Moreover we have shown that not every shape can be reached by the system, in particular, area-preserving shape changes are forbidden, and the only shapes with zero mean curvature are the flat ones.

Summarizing, we can conclude that, on the one hand, the process of in-plane swelling is totally decoupled from transverse deflection, as we already pointed out the possibility of separately control the evolution of $\mathbf{u}$ and u_3 (at least in the linear approximation). On the other hand, the diffusion process is always coupled with deformations of the plate as we showed that the two phenomena decouples only when $\mathbf{u}$ and u_3 are zero for every time.

1.5   Analysis of the Stress-Free Problem

We now focus on a special class of solutions to the FCP such that $\mathbf{N} = 0$ and $\mathbf{M} = 0$. We will refer to this problem as the Stress Free Problem (SFP). From the constitutive equations (1.63) we obtain

$$\mathbf{E} = \frac{\eta}{3 + 2\eta} N_\mu \mathbf{I}, \qquad \mathbf{K} = \frac{12\eta}{\varepsilon(3 + 2\eta)} M_\mu \mathbf{I}, \tag{1.74}$$

so that in-plane strain and curvature are determined by the thickness resultants of the chemical potential. Along with Eq. (1.65) and the corresponding boundary conditions on the chemical potential, Eq. (1.74) constitute the SFP. Clearly, (1.74) fulfills the boundary conditions on tractions.

Next we derive a general representation for the solution of the SFP. First, we substitute (1.74) into (1.65) to obtain an integro-differential equation for μ

$$\partial_t \mu - \partial_{33}\mu = -\frac{48\eta}{3 + 2\eta} x_3 \int_{-1/2}^{1/2} \partial_t \mu \, z \mathrm{d}z - \frac{4\eta}{3 + 2\eta} \int_{-1/2}^{1/2} \partial_t \mu \, \mathrm{d}z. \tag{1.75}$$

Eq. (1.75) may be solved analytically in the Laplace domain in the case of step chemical potential at the boundary, namely $\mu_\star^\pm = [\bar{\mu}_m(\mathbf{x}) \pm \bar{\mu}_d(\mathbf{x})]H(t)$, with $H(t)$ the Heaviside step function. This approach was also used by Taber [Taber, 1992] and the details of the derivation are reported in Appendix (A). Denoting by a superposed hat the Laplace transform and by s the Laplace complex variable, the solution for generic boundary conditions on the chemical potential reads

$$\hat{\mu}(\mathbf{x}, x_3, s) = s\hat{\mu}_m(\mathbf{x}, s)\hat{\nu}_e(x_3, s) + s\hat{\mu}_d(\mathbf{x}, s)\hat{\nu}_o(x_3, s), \tag{1.76}$$

where $\hat{\nu}_e$ and $\hat{\nu}_o$ are the Laplace transforms of the solutions corresponding to $\hat{\mu}_\star^\pm = 1/s$ and $\hat{\mu}_\star^\pm = \pm 1/s$, respectively, see Eq. (A.6). Consequently, by plugging Eq. (1.76) into the transforms of Eq. (1.74), we obtain

$$\hat{\mathbf{E}}(\mathbf{x}, s) = s\hat{\mu}_m(\mathbf{x}, s)\hat{f}_{\mathbf{E}}(s)\mathbf{I}, \quad \hat{\mathbf{K}}(\mathbf{x}, s) = s\hat{\mu}_d(\mathbf{x}, s)\hat{f}_{\mathbf{K}}(s)\mathbf{I}, \tag{1.77}$$

where

$$\hat{f}_{\mathbf{E}}(s) = \frac{\eta}{3 + 2\eta} \int_{-\frac{1}{2}}^{\frac{1}{2}} \hat{\nu}_e(z, s)\mathrm{d}z = \frac{2\eta}{s\left[3\sqrt{s}(1 + 2\eta)\coth(\sqrt{s}/2) - 8\eta\right]}, \tag{1.78a}$$

$$\hat{f}_{\mathbf{K}}(s) = \frac{12\eta}{\varepsilon(3 + 2\eta)} \int_{-\frac{1}{2}}^{\frac{1}{2}} \hat{\nu}_o(z, t)z\mathrm{d}z = \frac{4\eta\left(\sqrt{s}\coth(\sqrt{s}/2) - 2\right)}{s\,\varepsilon\left[\eta\left(2s - 8\sqrt{s}\coth(\sqrt{s}/2) + 16\right) + s\right]}. \tag{1.78b}$$

Clearly, to recover the displacement fields $\mathbf{u}$ and u_3 by integration of Eqs. (1.77), the following compatibility conditions as given by Ciarlet in [Ciarlet et al., 2008] must be satisfied

$$\partial_{11}\hat{E}_{22} + \partial_{22}\hat{E}_{11} - 2\partial_{12}\hat{E}_{12} = 0, \tag{1.79a}$$

$$\partial_2\hat{K}_{11} - \partial_1\hat{K}_{21} = 0, \tag{1.79b}$$

$$\partial_2\hat{K}_{12} - \partial_1\hat{K}_{22} = 0. \tag{1.79c}$$

These are necessary conditions that become also sufficient in case ω is a simply connected domain. Interestingly, these conditions lead to restrictions on the spatial dependence of the boundary chemical potential, such that $\Delta\mu_m = 0$ and $\nabla\mu_d = 0$. By recalling the definitions of μ_m and μ_d, we readily obtain $\mu_\star^+ = \varphi$ and $\mu_\star^- = \varphi + c$, for some harmonic function φ with c a constant. We notice that, since harmonic functions are C^∞, non-smooth boundary conditions necessarily lead to an evolution in the presence of stress.

In the time domain, Eq. (1.77) gives the following representation formula for the evolution of the strains

$$\mathbf{E} = (\partial_t\mu_m * f_{\mathbf{E}})\,\mathbf{I}, \quad \mathbf{K} = (\partial_t\mu_d * f_{\mathbf{K}})\,\mathbf{I}, \tag{1.80}$$

with '$*$' denoting the time convolution. In contrast with the FCP, from Eq.(1.80) we deduce that an emerging feature of these solutions is the local dependence on boundary conditions. Further since μ_d must be independent of the in-plane coordinates, stress free solutions can only have spatially homogeneous curvature *i.e.* they are spherical caps. Consequently, in the case of time independent boundary conditions $\mathbf{K}(t) = \bar{\mu}_d f_{\mathbf{K}}(t)\mathbf{I}$, such that integration yields the transverse displacement field $u_3(\mathbf{x}, t) = \bar{\mu}_d f_{\mathbf{K}}(t)|\mathbf{x}|^2/2$.

Additionally, stress-free conditions allow to exploit heterogeneous in-plane strains to realize any planar shape for the mid-plane. This result relies on the conformal nature of the plane projection $\mathbf{p} : \mathbf{x} \mapsto \mathbf{x} + \mathbf{u}$ of the immersion of the mid-surface and follows from the *Riemann mapping theorem* [Nehari, 1952]. To show that the map $\mathbf{p}$ is conformal, it is sufficient to notice that the strains in Eq. (1.74) are spherical. Hence, within the context of the present linear theory, the plate may be morphed in any time-dependent family of spherical shapes with given geometry of the mid-plane by superposing swelling induced bending to planar deformations.

1.5.1 Approximate solution for step boundary conditions

In general, we notice that recovering the solution of Eq. (1.76) in the time domain is not feasible, so that a numerical approach is needed. However, in the following we propose an approximate
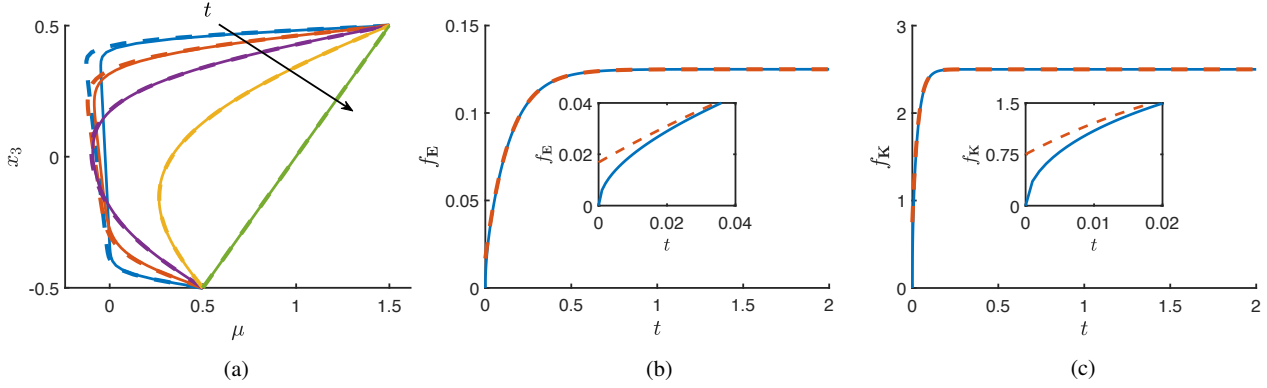
Figure 1.3: *Comparison between approximate expressions (dashed lines) and solutions computed numerically by the inverse Laplace transform (solid lines) for the chemical potential (a) at times $t = \{0.001, 0.005, 0.02, 0.1, 1\}$ for $\bar{\mu}_m = 1$ and $\bar{\mu}_d = 0.5$, the time-dependent components of the strain (b), and of the curvature (c). For all plots, $\eta = 0.5$, 200 spatial eigenfunctions were used to produce the plots in (a), and $\varepsilon = 0.1$ was chosen for the plot in (c).*

$$\alpha_{n,\eta} = \frac{32 A_\eta B_\eta \eta}{\pi^2 (n^2 - B_\eta)(3 + 2\eta)} \qquad \gamma_{n,\eta} = \frac{96 C_\eta D_\eta \eta}{\pi^2 (n^2 - 4D_\eta)(3 + 2\eta)}$$

$$\rho_{n,\eta} = \frac{3\pi^2 (1 + 2\eta)(n^2 - B_\eta) - 32 A_\eta n^2 \eta}{\pi^2 (n^2 - B_\eta)(3 + 2\eta)} \qquad \sigma_{n,\eta} = \frac{3\pi^2 (1 + 2\eta)(n^2 - 4D_\eta) - 24 C_\eta n^2 \eta}{\pi^2 (n^2 - 4D_\eta)(3 + 2\eta)}$$

$$A_\eta = \frac{6\eta + 3}{3 + \eta\,(2 + 32/\pi^2)} \qquad B_\eta = \frac{2\eta + 3}{3 + \eta\,(2 + 32/\pi^2)}$$

$$C_\eta = \frac{6\eta + 3}{3 + \eta\,(2 + 24/\pi^2)} \qquad D_\eta = \frac{2\eta + 3}{3 + \eta\,(2 + 24/\pi^2)}$$

Table 1.1: *Definitions of the coefficients $\alpha_{n,\eta}, \gamma_{n,\eta}, \rho_{n,\eta}, \sigma_{n,\eta}$ and $A_\eta, B_\eta, C_\eta, D_\eta$ for the approximate solutions of (1.82)-(1.83).*

solution that admits an explicit representation in time for the case of step boundary conditions. To this aim, it is crucial to manipulate the terms $\hat{\nu}_e$ and $\hat{\nu}_o$. First, let us observe that the following series expansions hold

$$s^{-3/2} \tanh(\sqrt{s}/2) = \frac{1}{2s} - \sum_{n=1}^{\infty} \frac{4}{\pi^2 (2n-1)^2 [s + \pi^2 (2n-1)^2]}, \qquad (1.81a)$$

$$s^{-3/2} \coth(\sqrt{s}/2) = \frac{1}{6s} + 2s^2 - \sum_{n=1}^{\infty} \frac{4}{4\pi^2 n^2 [s + 4\pi^2 n^2]}. \qquad (1.81b)$$
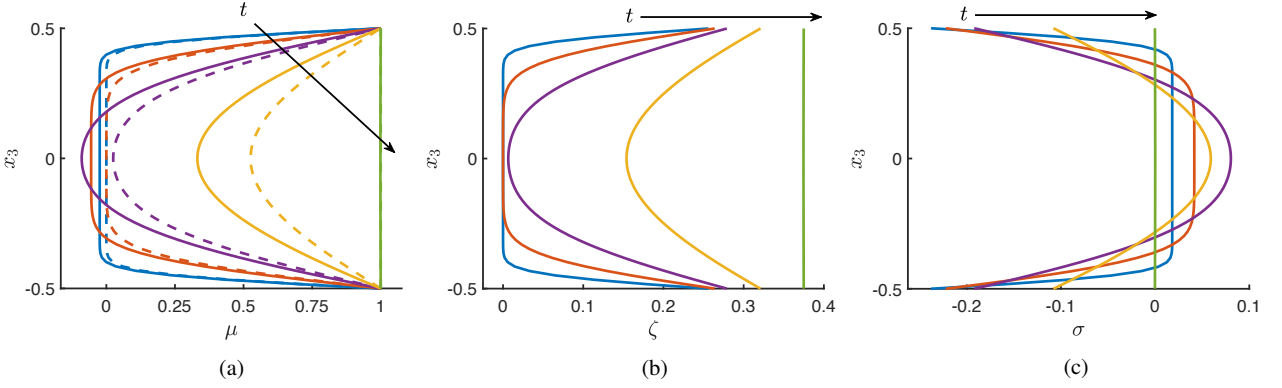
Figure 1.4: Plots for chemical potential (a), incremental volume change (b) and spherical part of the in-plane stress (c) at times $t = \{0.001, 0.005, 0.02, 0.1, 1\}$, for $\bar{\mu}_m = 1$, $\bar{\mu}_d = 0$, and $\eta = 0.5$. Dashed lines in (a) correspond to the solution in the pure diffusion case ($\eta = 0$).

By taking the first term in each sum, substituting these expressions in Eq. (1.76), and performing the inverse Laplace transform we arrive at

$$\mu \simeq \mu_s - \bar{\mu}_m \sum_{n=1}^{\infty} \frac{\phi_{2n-1}}{(2n-1)\pi} \left(\alpha_{2n-1,\eta} e^{-B_\eta \pi^2 t} + \rho_{2n-1,\eta} e^{-(2n-1)^2 \pi^2 t} \right) +$$

$$+ \bar{\mu}_d \sum_{n=1}^{\infty} \frac{\phi_{2n}}{2n\pi} \left(\gamma_{2n,\eta} e^{-4D_\eta \pi^2 t} + \sigma_{2n,\eta} e^{-(2n)^2 \pi^2 t} \right) , \tag{1.82}$$

where $\mu_s = \bar{\mu}_m + 2\bar{\mu}_d x_3$ is the steady-state solution and the coefficients are reported in Table 1.1. Interestingly, although solvent transport is coupled with elasticity, the evolution in time is characterized by decaying exponentials, as it is typical of diffusive processes. In general, this feature may not hold true in the FCP case. To estimate the accuracy of the approximation, we compared it with the inverse Laplace transform of Eq. (1.76) for the case of $\bar{\mu}_m = 1$, $\bar{\mu}_d = 0.5$, computed numerically using the Euler's algorithm [Abate and Whitt, 2006]. The comparison is reported in Fig. 1.3a for $t = \{0.001, 0.005, 0.02, 0.1, 1\}$ and shows good agreement, apart from early times. In the initial transient, the chemical potential profile exhibits boundary layers near $x_3 = \pm 1/2$ that surround an almost flat region with negative values. As expected, the solution attains steady-state at large times.

Similarly, approximate expressions can be obtained for the time-dependent components of strain and curvature, namely

$$f_{\mathbf{E}} \simeq \frac{\eta}{3 + 2\eta} \left(1 - A_\eta \frac{8}{\pi^2} e^{-B_\eta \pi^2 t} \right) , \tag{1.83a}$$

$$f_{\mathbf{K}} \simeq \frac{12\eta}{\varepsilon(3 + 2\eta)} \left(\frac{1}{6} - C_\eta \frac{4}{\pi^2} e^{-4D_\eta \pi^2 t} \right) , \tag{1.83b}$$

where, again, the coefficients are defined in Table 1.1. Since $f_{\mathbf{E}}$ and $f_{\mathbf{K}}$ are proportional to the thickness resultants of the chemical potential (see Eq. (1.78)), formulas in Eq. (1.83) well approximate the numerical solution (Fig. 1.3b-1.3c). Notice that Eq. (1.83) do not satisfy initial conditions because of the poor accuracy of the approximation at short times (insets of Fig. 1.3b-1.3c). In practice, Eq. (1.83a) may be fitted to data from free-swelling experiments ($\mu_\star^\pm = \text{const}$) to identify the
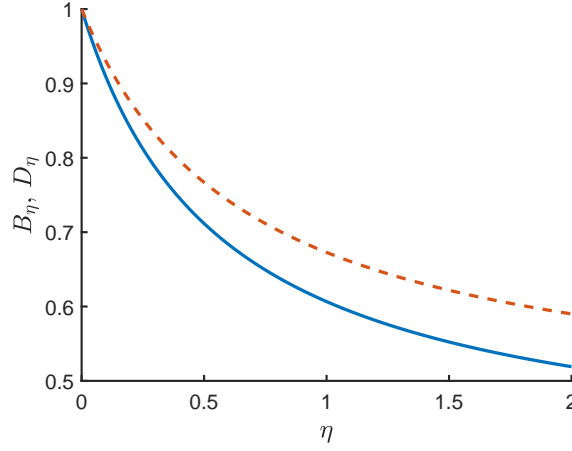
Figure 1.5: Plots of B_η (solid blue line) and D_η (dashed red line) as functions of η.

material parameters from η and τ. In passing, from Eqs. (1.82)-(1.83) we notice that the parameter η influences the rate at which the steady-state is attained through the quantities B_η and D_η, whose dependencies on η are depicted in Fig. (1.5).

We now focus on the distributions of strains and stresses along the thickness during the transient in relation to the profiles of the chemical potential. It is convenient to consider the effect of $\bar{\mu}_m$ separately from that of $\bar{\mu}_d$, which we set to zero. As already observed and more explicitly illustrated in Fig. 1.4a, μ attains negative values in the central region at early times. Physically, this behavior follows from the undrained response of the plate core, since swelling is initially localized at the top and bottom faces of the plate. Indeed, from Eqs. (1.44) and (1.52) we can reconstruct the incremental volume change ζ as

$$\zeta = \frac{\eta}{1 + 2\,\eta}\left(2\mathrm{tr}\mathbf{E} + \mu\right),\tag{1.84}$$

whose plot is reported in Fig. 1.4b. Clearly, under undrained conditions ($\zeta = 0$) and upon swelling ($\mathrm{tr}E > 0$), the chemical potential is negative.

Finally, we can recover the spherical component σ of the in-plane stress from the three-dimensional constitutive equations Eqs. (1.52) together with the reduced kinematics of the plate model and notice that regions that swell first are compressed, while the core is initially under tension (Fig. 1.4c).

1.5.2   The pure diffusion regime of $\eta \to 0$

In this section, we consider the limiting regime where $\eta \to 0$ as concerns the time evolution of chemical potential, strain and curvature. As for the chemical potential, Eq. (1.75) shows that in such limit μ obeys a pure diffusion equation, such that the coupling with elasticity is suppressed. The solution of this equation may be obtained using separation of variables as

$$\mu_{PD} = \mu_s - \bar{\mu}_m \sum_{n=1}^{\infty} \frac{\phi_{2n-1}}{\pi(2n-1)} e^{-\pi^2(2n-1)^2 t} + \bar{\mu}_d \sum_{n=1}^{\infty} \frac{\phi_{2n}}{2n\pi} e^{-4\pi^2 n^2 t}.\tag{1.85}$$

Of course, Eq. (1.85) may also be recovered as the inverse Laplace transform of the limit of Eq. (1.76). Upon swelling, the comparison of Eq. (1.85) with the solution for $\eta = 0.5$ in Fig. 1.4a shows that the chemical potential never attains negative values in the pure diffusion regime, as expected from the

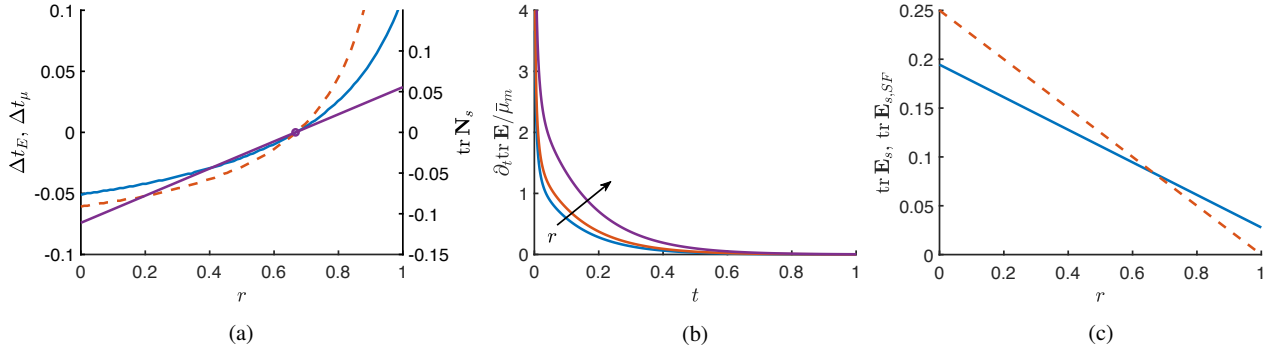*Figure 1.6: Effect of stresses on the swelling dynamics for $\eta = 0.5$. (a) Time differences Δt_E (solid blue line) and Δt_μ (dashed red line) as functions of the radial coordinate. The purple line represents the trace of $\mathbf{N}$ at equilibrium. The crossover point of $\Delta t_E = \Delta t_\mu$ corresponds to the location where $\mathrm{tr}\mathbf{N}_s$ vanishes. (b) Normalized time-rate of $\mathrm{tr}\mathbf{E}$ as a function of time, for $r = \{0, 2/3, 0.9\}$. (c) Steady-state profiles of $\mathrm{tr}\mathbf{E}$ in the fully coupled case (solid blue line) and in the stress-free case (dashed red line).*

properties of the solutions of the pure diffusion equation. In practice, for a gel plate the limit $\eta \to 0$ can be achieved in dry conditions, where $\lambda \to \infty$. Consequently, the characteristic time τ vanishes, such that diffusion is instantaneous. Moreover, strains and curvature also vanish, because of the stress-free relations Eq. (1.74). This feature is conserved by the approximations in Eq. (1.83).

1.6 Effect of stresses on the swelling dynamics: An example

To assess how stresses affect the dynamics of swelling in general, we now study a problem where boundary conditions do not allow for a stress-free solution. For simplicity, we consider a circular plate of unit (dimensionless) radius subject to axisymmetric chemical potential: $\bar{\mu}_\star^\pm = \bar{\mu}_m(r)$, where r is the radial coordinate. Given the symmetry of both geometry and boundary conditions, the deformation is characterized by the radial displacement field $u(r,t)$. The chemical potential that solves Eq. (1.65) admits the representation in Eq. (A.2), as for the stress-free case. Passing to the Laplace domain and using the result of Eq. (A.5) into the constitutive equation (1.63a) we obtain $\hat{\mathbf{N}}$ in polar components as

$$\hat{N}_r = \frac{2 + \eta(2 + \mathcal{A})}{1 + 2\eta} \hat{E}_r + \frac{1 + \eta\mathcal{A}}{1 + 2\eta} \hat{E}_\theta - \frac{\eta}{1 + 2\eta} \left(\frac{\bar{\mu}_m}{s} + \mathcal{D} \right), \tag{1.86a}$$

$$\hat{N}_\theta = \frac{2 + \eta(2 + \mathcal{A})}{1 + 2\eta} \hat{E}_\theta + \frac{1 + \eta\mathcal{A}}{1 + 2\eta} \hat{E}_r - \frac{\eta}{1 + 2\eta} \left(\frac{\bar{\mu}_m}{s} + \mathcal{D} \right), \tag{1.86b}$$

where $\hat{E}_r = \mathrm{d}\hat{u}/\mathrm{d}r$ and $\hat{E}_\theta = \hat{u}/r$ are the strain components. Then, substitution of (1.86) into the equilibrium equation

$$\frac{\mathrm{d}\hat{N}_r}{\mathrm{d}r} + \frac{\hat{N}_r - \hat{N}_\theta}{r} = 0, \tag{1.87}$$

leads to

$$\frac{\mathrm{d}^2\hat{u}}{\mathrm{d}r^2} + \frac{1}{r}\frac{\mathrm{d}\hat{u}}{\mathrm{d}r} - \frac{\hat{u}}{r^2} = \frac{\eta}{2 + \eta(2 + \mathcal{A})} \frac{\mathrm{d}}{\mathrm{d}r}\left(\frac{\bar{\mu}_m}{s} + \mathcal{D} \right), \tag{1.88}$$

which can be solved along with the boundary conditions $\hat{N}_r(1) = 0$ and $\hat{u}(0) = 0$ to obtain

$$\hat{u} = \frac{\eta}{[2 + \eta(2 + \mathcal{A})]r} \int_0^r \left(\frac{\bar{\mu}_m}{s} + \mathcal{D} \right) \rho \mathrm{d}\rho + \tag{1.89}$$

$$+ \frac{\eta(1 + 2\eta)r}{[3 + 2\eta(1 + \mathcal{A})][2 + \eta(2 + \mathcal{A})]} \int_0^1 \left(\frac{\bar{\mu}_m}{s} + \mathcal{D} \right) \rho \mathrm{d}\rho \,.$$

We remark that the solution (1.89) depends on the chemical potential also through the function $\mathcal{D}$, see Appendix A.

For the purpose of the present study, we choose the simple case of $\bar{\mu}_m(r) = 1 - r$. By exploiting the final value theorem for the Laplace transform, the steady-state radial displacement field is obtained as

$$u_s = \frac{\eta(5 + 4\eta)}{6(1 + \eta)(3 + 2\eta)}r - \frac{\eta}{6(1 + \eta)}r^2 \,, \tag{1.90}$$

such that

$$\mathrm{tr}\mathbf{E}_s = \frac{\eta(5 + 4\eta)}{3(1 + \eta)(3 + 2\eta)} - \frac{\eta}{2(1 + \eta)}r \,, \tag{1.91}$$

and the constitutive relations yield

$$\mathrm{tr}\mathbf{N}_s = -\frac{\eta}{3(1 + \eta)} + \frac{\eta}{2(1 + \eta)}r \,. \tag{1.92}$$

We observe that $\mathrm{tr}\mathbf{N}_s$ vanishes at $r = 2/3$, a feature that also holds during the transient, since $\mathrm{tr}\hat{\mathbf{N}}(2/3, s) = 0$. Finally, we report the spherical part of the in-plane strain under steady-state as obtained by assuming stress-free conditions

$$\mathrm{tr}\mathbf{E}_{s,SF} = \frac{2\eta}{3 + 2\eta} - \frac{2\eta}{3 + 2\eta}r \,. \tag{1.93}$$

We remark that the strain field in Eq. (1.93) corresponds to the *target metric* from the theory of non-Euclidean plates [Efrati et al., 2009] and is not compatible in general. With these expressions at hand, we proceed to discuss how the presence of membrane stresses influences the swelling dynamics. As an average measure of swelling rate, we define the time $t_E(r)$ needed for $\mathrm{tr}\mathbf{E}$ to reach its steady state value $\mathrm{tr}\mathbf{E}_s$ within a tolerance of 0.1%. We notice that such a measure is conveniently a constant, $t_{E,SF}$, which only depends on η for any stress-free problem, as it may be deduced from the expressions for $f_{\mathbf{E}}(t)$, see Section 1.5. Analogously, we introduce $t_\mu(r)$ for N_μ. In Fig. 1.6a we report results for $\Delta t_E = t_E/t_{E,SF} - 1$, along with the steady state value $\mathrm{tr}\mathbf{N}_s$ of the spherical membrane stress. We notice that compressive (tensile) stresses promote faster (slower) swelling with respect to the stress-free case. This remarkable feature may be explained by considering the time evolution of the quantities $\mathrm{tr}\mathbf{E}$ and N_μ, which are related to $\mathrm{tr}\mathbf{N}$ via the constitutive equation Eq. (1.63a). Let us consider the inner region of the disk, where $\mathrm{tr}\mathbf{N} < 0$. Then, by taking the trace and the time derivative of Eq. (1.63a), we can show that the time-rate of $\mathrm{tr}\mathbf{E}$ is smaller than that of N_μ. Further, it is possible to show that the only choice consistent with the governing equations is that strain rates are smaller under compression with respect to the stress-free case, as confirmed by numerical results in Fig. 1.6b. With this, from Eq. (1.65), we deduce that the time rate of N_μ is larger than that in stress-free conditions, so that N_μ attains the steady state faster ($\Delta t_\mu < 0$), as shown in Fig. 1.6a. Despite strain rates are smaller in the inner region, swelling is faster ($\Delta t_E < 0$), since $\mathrm{tr}\mathbf{E}_s$ is smaller than in the stress-free case, because of compressive stresses (Fig. 1.6c). A similar reasoning leads to the interpretation of the results for the region of the disk under tension.

1.7 Conclusions

In this work, we have derived a linear poroelastic plate model for polymer gels to investigate their transient response to an external stimulus. First, we have studied a stress-free problem that has allowed us to obtain explicit, approximate solutions for the time evolutions of chemical potential, in-plane strain and curvature. Then, we have presented a problem where elasticity and solvent transport are fully-coupled, namely, the planar swelling of a circular plate, which we have solved using a semi-analytical approach. We have found that tensile (compressive) membrane stresses delay (accelerate) swelling. Even though such an example concerns a specific choice of geometry and boundary conditions, our results highlight the impact of stresses on the dynamics of swelling and, hence, on the evolution of shape in thin poroelastic plates. Given the theoretical nature of the present study, we also plan to carry out experiments to validate our conclusions. The linear theory is applicable whenever perturbations of the external chemical potential induce small strains and displacements with respect to the initial, equilibrium configuration. However, we expect the present theory to be valid even for moderate strains ($\sim 10\%$) [Tanaka and Fillmore, 1979, Yamaue and Doi, 2004] in planar, stress-free evolutions or, more generally, far from bifurcations induced by the interplay between in-plane metric changes and curvature. Future works will be devoted to generalizing our findings, as well as extending the model to the non-linear regime.

Chapter 2

Optimal design of planar shapes with active materials

2.1 Introduction

Designing new strategies based on active materials for the functional, morphing of bodies into prescribed shapes is currently the subject of intense research having implications in a number of engineering and related fields [Jeon et al., 2017, Nojoomi et al., 2018, Aharoni et al., 2018, Andrini et al., 2020, Guseinov et al., 2020, Leronni and Bardella, 2021]. In particular, soft robotics makes broad use of smart materials (*e.g.*, polymer gels, liquid crystal elastomers, electroactive polymers) for actuation and sensing, often by drawing inspiration from natural systems [Sareh et al., 2013, Ford et al., 2019, Noselli et al., 2019, Riccobelli et al., 2020, Cicconofri et al., 2020, Liu et al., 2021]. Indeed, these systems frequently exploit the internal activity of biological tissues and structures to induce the shape changes that are necessary to sustain life [Gray, 1953, Childress, 1981]. Besides its practical relevance, the study of shape-shifting materials is also interesting from a theoretical perspective, as it brings new challenges lying at the interface among differential geometry, analysis and mechanics [Efrati et al., 2009, Efrati et al., 2013, Arroyo and DeSimone, 2014, Goriely, 2017, van Rees et al., 2017, Agostiniani et al., 2019].

Typically, programming equilibrium shape transformations in active structures requires the spatial control of either the material architecture or the external stimulus that triggers the active response. In practice, the active mechanism driving such transformations varies significantly depending on the material. For example, polymer gels swell (or shrink) isotropically in response to changes in the environmental conditions [Hong et al., 2008, Chester and Anand, 2010, Lucantonio et al., 2013]. As another example, liquid crystal elastomers exhibit distinct active stretches in mutually orthogonal directions as a consequence of temperature-driven, molecular re-orientation [Warner and Terentjev, 2003, Sawa et al., 2010]. Then, a relevant and timely question is to devise a criterion for the identification of the active mechanism that is most effective for the attainment of a target shape change. This is the focus of the present study, where such a criterion is based on a notion of "complexity" that accounts for both the magnitude and the spatial variations of the controls. In the present context, the controls correspond to the target metric [Efrati et al., 2013], which we adopt as a unifying descriptor of the diverse active mechanisms, irrespective of the physics behind them. Our approach differs from previous studies on the topic [Günnel and Herzog, 2016, Lucantonio and DeSimone, 2020, Ortigosa et al., 2021], as they were restricted to specific material architectures.

To determine the optimal target metric field for a prescribed shape change, we introduce an optimal control problem based on an objective functional that comprises the complexity of the controls and a penalty term accounting for the distance between the actual and the target shapes. We restrict the study to the active planar morphing of hyperelastic bodies in the plain-strain regime and in the absence of external forces. Due to the complexity of the non-linear optimization problem, we devise and apply a computational approach for the study of generic shape changes. However, the case of affine shape changes is also amenable to analytical treatments.

We remark that our approach to tackle shape morphing problems is alternative to those available in the relevant literature. Indeed, its applicability is not restricted to a specific material class or active mechanism. Rather, it may be exploited to identify new efficient solutions to shape morphing problems and for the accurate design of active systems.

The Chapter is structured as follows. In Section 2.2 we provide a short review of elasticity with distortions. In Section 2.3 we state the constrained optimal control problem. We introduce the objective functional, whose minimization is subject to mechanical equilibrium. Section 2.4 is devoted to the analysis of affine shape changes, for which we obtain explicit conditions of optimality. These are verified in Section 2.5 by means of numerical computations, then extended to the study of more complex shape transitions. We present results for the prototypical shape change of the planar active bending of a block for distinct choices of the complexity functional. Finally, we demonstrate that the proposed approach is applicable to complex shape changes. Section 2.6 closes the Chapter.

2.2   Short review of elasticity with distortions

We devote this Section to a short review of the concept of target metric mentioned in the introduction and, more in general, of the theory of hyperelasticity with distortions. Such a theory first originated with the intent of modeling plasticity of solids [Bilby et al., 1955, Kröner, 1959, Lee, 1969] and was later extended to growth phenomena in soft matter and active materials [Kondaurov and Nikitin, 1987, Taber and Perucchio, 2000, Nardinocchi and Teresi, 2007, Riccobelli and Ambrosi, 2019]. Abstracting from the specific application, distortions theory aims at modelling deformation processes which are not entirely ascribable to mechanical work performed onto the body. Examples of phenomena included in such a theory are thermal distortions, swelling deformations in porous media, and growth processes. In all these cases, the deformation is the result of a subtle interplay between the *accretive forces* (*e.g.* thermal diffusion, solvent diffusion and growth phenomena) and the hyper-elastic response of the body.

Historically, the theory that was first developed relied on the so called *multiplicative decomposition* of the deformation gradient. In such a theory, it is assumed that only a "part" of the actual deformation gradient $\mathbf{F}$, denoted by $\mathbf{F}_e$, contributes to the accumulation of elastic energy since the remaining part of it, denoted by $\mathbf{F}_0$, is supposed to draw energy from a non-mechanical external source. The tensor field $\mathbf{F}_0$ is then called *distortion* and it acts on material fibers accounting for non-elastic phenomena. It is crucial to observe that distortions are in general not curl-free. Hence, $\mathbf{F}_0$ is not the gradient of a deformation map, namely, is not *compatible*. This fact implies that, in general, the distortion cannot coincide with the actual deformation gradient $\mathbf{F}$. Then, hyperelasticity comes into play by selecting, through an energy minimization principle, the *elastic* tensor field $\mathbf{F}_e$ which restores compatibility and contributes to $\mathbf{F}$ according to the following multiplicative decomposition
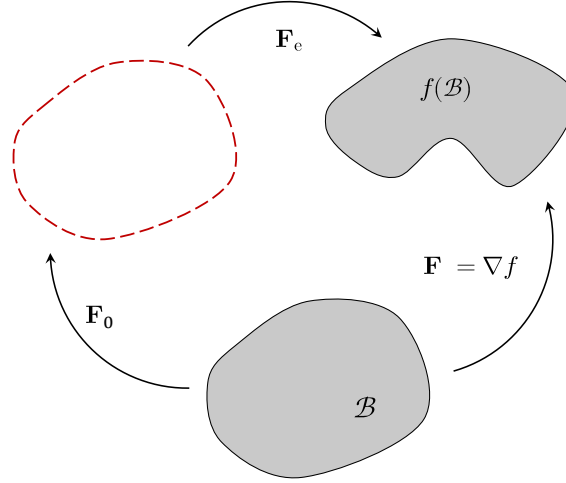
Figure 2.1: Commutative diagram relating the reference configuration $\mathcal{B}$, actual configuration $f(\mathcal{B})$ and virtual configuration (depicted with a red dashed line).

$$\mathbf{F} = \mathbf{F}_e \mathbf{F}_0, \tag{2.1}$$

where tensor fields $\mathbf{F}_e$ and $\mathbf{F}_0$ are required to be invertible and with positive determinant.

It is customary to introduce an energy density $\psi_0 = \psi_0(\mathbf{F}_e)$ per unit *relaxed* volume. Indeed, as explained by the diagram of Fig. 2.1, we can distinguish between the reference configuration $\mathcal{B}$ prior to the intervention of $\mathbf{F}_0$, the actual configuration $\mathcal{B}_f = f(\mathcal{B})$, and a *relaxed* (or *virtual* configuration) identified by the action of $\mathbf{F}_0$ on material elements of $\mathcal{B}$. Hence, as can be deduced from the diagram in Fig. 2.1, the energy density per unit *reference* volume, written in terms of the actual deformation $\mathbf{F}$, reads

$$\psi(\mathbf{F}) = J_0 \psi_0(\mathbf{F}\mathbf{F}_0^{-1}),$$

where $J_0 = \det \mathbf{F}_0$.

The multiplicative decomposition of the gradient has strong connections with the theory of non-Euclidean mechanics, recently introduced in [Efrati et al., 2009, Efrati et al., 2013], according to which the elastic energy is written as a function of the Cauchy-Green metric tensor $\mathbf{C}$ and the so called *target* metric tensor $\bar{\mathbf{C}}$. The former provides a measure of the local distances between points in the actual configuration, while the latter locally sets the *rest* distances, namely the distances for which the elastic energy is null. Hence, the energy density is constructed so that it becomes zero only when the actual distances coincide with the rest ones, namely when $\mathbf{C} = \bar{\mathbf{C}}$. However $\bar{\mathbf{C}}$ may be not the pull-back of a deformation map, that is it may not be *compatible*. Hence, in general, a discrepancy between the two metric tensor must be present, giving rise to a non trivial stress distribution inside the body. The similarities between such a theory and the multiplicative decomposition of the deformation gradient become apparent when comparing the role of $\bar{\mathbf{C}}$ and $\mathbf{F}_0$, both describing the natural state of system prescribed by distortions. Likewise, the discrepancy arising between the two metric tensors is completely analogous to that arising between $\mathbf{F}$ and $\mathbf{F}_0$,

quantified by $\mathbf{F}_e$. Hence, given an energy density $\psi_0 = \psi_0(\mathbf{C}, \bar{\mathbf{C}})$ per unit *relaxed* volume (in this case identified by the action of $\bar{\mathbf{C}}$ on material fibers) we can write the energy per unit *reference* volume as

$$\psi(\mathbf{C}, \bar{\mathbf{C}}) = J_0 \psi_0(\mathbf{C}, \bar{\mathbf{C}}).$$

For the purpose of this Section we leave the balance law and the energetic description of phenomena determining $\mathbf{F}_0$ (or $\bar{\mathbf{C}}$) unspecified and simply assume the distortion field to be assigned as a datum. An extension of the present theory by means of an additional balance law for the accretive forces, regulating the time evolution of distortions, will be employed in the next Chapter.

2.3   Shape optimization problem

We study the planar shape morphing of a cylindrical body $\mathcal{B} \subset \mathbb{R}^3$ whose normal cross-section is denoted by $\omega \subset \mathbb{R}^2$. Specifically, we assume plane strain conditions such that the morphing problem consists in devising a strategy to bring the boundary $\partial\omega = \Gamma$ with unit normal $\mathbf{n}$ close to a target planar curve $\bar{\Gamma}$ with unit normal $\mathbf{m}$, see Fig. 2.2. Further, we assume that the body is traction-free and that it is made of an active material, which allows to realize shape changes by the local control of the natural state through active strains or distortions.

Let $f : \omega \to \mathbb{R}^2$ denote the planar part of the deformation, which maps a material point $X \in \omega$ into the corresponding place x in the current configuration. By adopting a standard notation for related kinematic quantities, we write: $\mathbf{F} = \nabla f$, $\mathbf{C} = \mathbf{F}^\mathsf{T}\mathbf{F}$ and $J = \det \mathbf{F}$. Finally, we introduce an orthonormal reference frame $(\mathbf{e}_1, \mathbf{e}_2, \mathbf{e}_3)$, with $\mathbf{e}_1$ and $\mathbf{e}_2$ lying in ω.
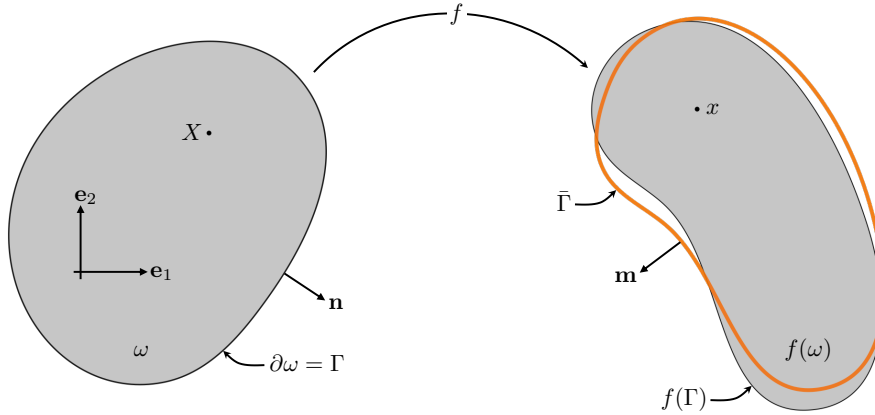
Figure 2.2: Kinematics of the shape optimization problem. Here, ω is the cross-section of the cylindrical body, which undergoes a deformation denoted by $f : \omega \to \mathbb{R}^2$, $X \mapsto f(X) = x$. We also highlight its boundary Γ and the corresponding target curve $\bar{\Gamma}$, with outer unit normals $\mathbf{n}$ and $\mathbf{m}$, respectively.

2.3.1   Mechanics

We characterize the material response by an elastic strain energy density per unit reference volume in $\mathcal{B}$ depending on the actual metric (the three-dimensional right Cauchy-Green strain) and the target metric, which sets the natural state of the system [Efrati et al., 2009, Sharon and Efrati, 2010, Efrati et al., 2013, Nardinocchi et al., 2013]. Consistently with the plane strain hypothesis, we

assume that the target metric does not induce out-of-plane strains, *i.e.* only its in-plane components are non-trivial and invariant along the axis of the cylindrical body. Hence, we introduce a plane elastic energy density $\psi(\mathbf{C}, \bar{\mathbf{C}})$ such that $\psi(\bar{\mathbf{C}}, \bar{\mathbf{C}}) = 0$ and $D_{\mathbf{C}}\psi(\bar{\mathbf{C}}, \bar{\mathbf{C}}) = 0$, with $\bar{\mathbf{C}}$ the plane target metric.

We recall that the boundary Γ is traction-free, so that the deformation of ω is only induced by active strains. Hence, the balance of forces in weak form reads:

$$\int_\omega \mathbf{S}(\mathbf{F}, \bar{\mathbf{C}}) \cdot \nabla \mathbf{u} = 0 \quad \forall \, \mathbf{u} \in T_f V, \quad f \in V \,, \tag{2.2}$$

where $\mathbf{S} = \partial_{\mathbf{F}}\psi$ is the plane part of the first Piola-Kirchhoff stress, $V = \{f : \omega \to \mathbb{R}^2 \mid \det \mathbf{F} > 0 \text{ in } \omega\}$ is the space of plane deformations and $T_f V = \{\mathbf{u} : \omega \to \mathbb{R}^2\}$ its tangent space at f[1].

2.3.2 The objective functional

As anticipated, we are interested in solving a shape optimization problem where we control the (plane) target metric $\bar{\mathbf{C}}$ so that Γ deforms into a prescribed target curve $\bar{\Gamma}$. Clearly, given a deformation sending Γ into $\bar{\Gamma}$, it would be sufficient to choose the controls $\bar{\mathbf{C}} = \mathbf{C}$ to obtain a stress-free solution for the problem. In practice, the target metric $\bar{\mathbf{C}}$ may be either encoded in an active material during fabrication or controlled through the spatial patterning of an external stimulus [Klein et al., 2007, Sawa et al., 2010, Jeon et al., 2017, Nojoomi et al., 2018, Aharoni et al., 2018, Andrini et al., 2020]. In principle, the pointwise stress-free solution may result in complex material architectures or stimuli. Hence, a more interesting problem consists in finding the optimal target metric $\bar{\mathbf{C}}$ deforming Γ into $\bar{\Gamma}$ while minimizing a *complexity functional* $\mathcal{C}(\bar{\mathbf{C}})$, for which we consider the following form:

$$\mathcal{C}(\bar{\mathbf{C}}) = \frac{1}{|\omega|} \int_\omega \chi(\bar{\mathbf{C}}, \nabla\bar{\mathbf{C}}) \,, \tag{2.3}$$

where $\chi : \mathrm{PSym}_2 \times \mathrm{Lin}_3 \to \mathbb{R}$ is a (dimensionless) density function $(\mathbf{G}, \Xi) \mapsto \chi(\mathbf{G}, \Xi)$. Notice that the dependence of the complexity density on both the target metric and its gradient expresses the cost associated to the magnitude and to the spatial variations of the controls, respectively. Moreover, we require the complexity to be *isotropic* in the sense that $\chi(\bar{\mathbf{C}}, \nabla\bar{\mathbf{C}}) = \chi(\mathbf{Q}\bar{\mathbf{C}}\mathbf{Q}^{\mathsf{T}}, \nabla(\mathbf{Q}\bar{\mathbf{C}}\mathbf{Q}^{\mathsf{T}}) \circ \mathbf{Q}^{\mathsf{T}}) \, \forall \, \mathbf{Q} \in \mathrm{Orth}^+$, so that two active distortions that share the principal stretches but differ by a rotation of their principal directions have the same complexity[2]. Finally, we assume that $\chi(\mathbf{G}, \Xi)$ has a minimum in $\Xi = \mathbf{0}$ for every $\mathbf{G}$, so that $D_\Xi\chi(\mathbf{G}, \mathbf{0}) = \mathbf{0}$.

In our approach, we relax the constraint of satisfying the target shape exactly, to allow for a broader set of optimal solutions. Specifically, we combine $\mathcal{C}(\bar{\mathbf{C}})$ with a penalty term accounting for the distance between the actual, $f(\Gamma)$, and the target, $\bar{\Gamma}$, shapes into the objective functional for the optimization problem. As concerns the notion of distance between curves, we choose the *Hausdorff*

---

[1]Throughout the rest of the Chapter and the entire Thesis, we will deliberately be sloppy when we adopt terms like "manifold" and "tangent space" and refer them to infinite dimensional spaces. Indeed, no attempt is made to rigorously asses the structure behind these sets. In particular the term "tangent space" simply refers to the notion of "admissible variations". Nevertheless, we found this notation very evocative and effective, and useful to perform formal calculations (see [Otto, 2001])

[2]Here the composition of the third order tensor $(\mathbf{a}_1 \otimes \mathbf{a}_2 \otimes \mathbf{a}_3)$ with the second order tensor $(\mathbf{b}_1 \otimes \mathbf{b}_2)$ reads $(\mathbf{a}_1 \otimes \mathbf{a}_2 \otimes \mathbf{a}_3) \circ (\mathbf{b}_1 \otimes \mathbf{b}_2) = (\mathbf{a}_3 \cdot \mathbf{b}_1)(\mathbf{a}_1 \otimes \mathbf{a}_2 \otimes \mathbf{b}_2)$.

distance [Delfour and Zolésio, 2011]

$$d_H(\Gamma_1, \Gamma_2) = \max\left\{ \sup_{X \in \Gamma_1} \inf_{Y \in \Gamma_2} |X - Y|, \sup_{X \in \Gamma_2} \inf_{Y \in \Gamma_1} |X - Y| \right\} \tag{2.4}$$

where Γ_1, Γ_2 are closed curves in $\mathbb{R}^2$.

In conclusion, the optimization problem reads:

$$\min_{\bar{\mathbf{C}} \in N, f \in V} \left\{ \mathcal{C}(\bar{\mathbf{C}}) + a_{\mathrm{d}} d_H(f(\Gamma), \bar{\Gamma}) \right\} \quad \text{s.t.} \int_\omega \mathbf{S}(\mathbf{F}, \bar{\mathbf{C}}) \cdot \nabla \mathbf{u} = 0 \quad \forall \mathbf{u} \in T_f V, \ f \in V, \tag{2.5}$$

where $N = \{\bar{\mathbf{C}} : \omega \to \mathrm{PSym}_2\}$ and the parameter a_{d} is a positive constant used to tune the relative weight of the distance penalty term. Observe that the solution to the constrained optimization problem, *i.e.*, the optimal target metric, is insensitive to roto-translations of the target shape, because the deformation that satisfies the balance of forces is defined up to such isometries.

2.4   On the optimality of affine shape changes

The aim of this section is to explore the optimality of target metrics that allow to obtain shape changes attainable by *homogeneous deformations*. These transformations are clearly relevant in applications for their simplicity and are amenable to analytical treatments. In particular, we seek a solution of the optimization problem that allows to satisfy the target shape exactly, such that (2.5) becomes

$$\min_{\bar{\mathbf{C}} \in N} \left\{ \mathcal{C}(\bar{\mathbf{C}}) \right\} \quad \text{s.t.} \int_\omega \mathbf{S}(\mathbf{F}, \bar{\mathbf{C}}) \cdot \nabla \mathbf{u} = 0 \quad \forall \mathbf{u} \in T_f V, \ f \in M, \tag{2.6}$$

where $M = \{f \in V : d_H(f(\Gamma), \bar{\Gamma}) = 0\}$ is the space of deformations mapping Γ into $\bar{\Gamma}$ *exactly*. We can think of (2.6) as the asymptotic limit of (2.5) for $a_{\mathrm{d}} \to \infty$.

Let $\mathbf{C}$ be the actual metric associated to the affine deformation f such that $f(\Gamma) = \bar{\Gamma}$. Then the homogeneous target metric $\bar{\mathbf{C}} = \mathbf{C}$ is the unique absolute minimizer of the elastic energy, so that the shape change $(\Gamma, \bar{\Gamma})$ can be achieved in the absence of stress. It remains to verify whether this stress-free solution minimizes the complexity functional. To this aim, we provide a result that allows to characterize affine shape changes for which homogeneous target metrics are optimal.

Proposition 3. *Let f be an affine map sending Γ into $\bar{\Gamma}$, with $\mathbf{C}$ the associated right Cauchy-Green strain, and assume an isotropic complexity density function χ. Then the homogeneous target metric $\bar{\mathbf{C}} = \mathbf{C}$ is a stationary point of the problem* (2.6) *if and only if at least one of the following conditions holds:*

(i) the outward normal $\mathbf{n}$ to the reference boundary Γ is an eigenvector of $\mathbf{C}$ everywhere on Γ;

(ii) the eigenvalues λ_i^2 of $\mathbf{C}$ and the eigenvalues μ_i of $\partial_{\mathbf{G}}\chi(\mathbf{C}, \mathbf{0})$ are such that $\lambda_1^2 \mu_1 - \lambda_2^2 \mu_2 = 0$.

Since $\mathbf{C} \in \mathrm{PSym}_2$, condition *(i)* implies that an affine shape change attained via a homogeneous target metric $\bar{\mathbf{C}} = \mathbf{C}$ is optimal whenever ω is the union of rectangles oriented along the eigenvectors of $\mathbf{C}$. Moreover, we anticipate that such a condition holds for any *isotropic* complexity density function χ, irrespective of its specific form. On the other hand, affine deformations for which condition *(ii)* holds are optimal independently of the reference shape Γ, but the existence of solutions to that condition depends on the specific choice of χ. As detailed in the following, the proof of the proposition above is divided into three main steps.

Step 1: Stationarity conditions of problem (2.6)   We seek optimal solutions to the problem (2.6) by determining the stationary points of the Lagrangian

$$\mathscr{L}(\bar{\mathbf{C}}, f, \boldsymbol{\eta}) = \mathcal{C}(\bar{\mathbf{C}}) - \frac{1}{|\omega|} \int_\omega \mathbf{F}\boldsymbol{\Sigma}(\mathbf{C}, \bar{\mathbf{C}}) \cdot \nabla\boldsymbol{\eta}, \quad (\bar{\mathbf{C}}, f, \boldsymbol{\eta}) \in N \times M \times T_f V, \tag{2.7}$$

where $\boldsymbol{\eta}$ is a Lagrange multiplier and $\boldsymbol{\Sigma}$ is the plane part of the second Piola-Kirchhoff stress tensor. We proceed by characterizing the tangent spaces to N and M. We have that $T_{\bar{\mathbf{C}}}N = \{\mathbf{V} : \omega \to \mathrm{Sym}_2\}$ and that, following [Fuchs et al., 2009], $T_f M = \{\mathbf{v} : \omega \to \mathbb{R}^2 \mid \mathbf{v}|_\Gamma = \mathbf{Pa}, \forall \mathbf{a} \in V_\Gamma\}$, where $\mathbf{P} = \mathbf{I} - (\mathbf{F}^{-\mathsf{T}}\mathbf{n} \otimes \mathbf{F}^{-\mathsf{T}}\mathbf{n})/|\mathbf{F}^{-\mathsf{T}}\mathbf{n}|^2$ is the tangent projector to $\bar{\Gamma}$ and $V_\Gamma = \{\mathbf{a} : \Gamma \to \mathbb{R}^2\}$. Hence, tangent vectors to M preserve (incrementally) the shape of the boundary since their restriction to Γ is tangent to $\bar{\Gamma}$. It is convenient to introduce the following notation for the Gâteaux derivative of $\mathcal{C}$ with respect to $\bar{\mathbf{C}}$:

$$D_{\bar{\mathbf{C}}}\mathcal{C}[\mathbf{V}] = \frac{1}{|\omega|} \int_\omega \nabla_{\bar{\mathbf{C}}}\mathcal{C} \cdot \mathbf{V} + \frac{1}{|\omega|} \int_\Gamma \mathbf{N} \cdot \mathbf{V}, \quad \mathbf{V} \in T_{\bar{\mathbf{C}}}N, \tag{2.8}$$

where $\nabla_{\bar{\mathbf{C}}}\mathcal{C} = \partial_{\mathbf{G}}\chi - \mathrm{Div}\,(\partial_\Xi \chi) \in \mathrm{Sym}_2$ and $\mathbf{N} = \partial_\Xi \chi[\mathbf{n}] \in \mathrm{Sym}_2{}^3$. With this definition, the derivative of the Lagrangian with respect to the target metric may be computed as

$$D_{\bar{\mathbf{C}}}\mathscr{L}[\mathbf{V}] = \frac{1}{|\omega|} \int_\omega \left(\nabla_{\bar{\mathbf{C}}}\mathcal{C} - (D_{\bar{\mathbf{C}}}\boldsymbol{\Sigma})^\mathsf{T}[\mathbf{F}^\mathsf{T}\nabla\boldsymbol{\eta}]\right) \cdot \mathbf{V} + \frac{1}{|\omega|} \int_\Gamma \mathbf{N} \cdot \mathbf{V} = 0, \quad \forall \mathbf{V} \in T_{\bar{\mathbf{C}}}N. \tag{2.9}$$

Hence, localization of the above equation leads to

$$\nabla_{\bar{\mathbf{C}}}\mathcal{C} - (D_{\bar{\mathbf{C}}}\boldsymbol{\Sigma})^\mathsf{T}[\mathbf{F}^\mathsf{T}\nabla\boldsymbol{\eta}] = \mathbf{0} \quad \text{in } \omega, \qquad \mathbf{N} = \mathbf{0} \quad \text{on } \Gamma, \tag{2.10}$$

where we used the fact that $\nabla_{\bar{\mathbf{C}}}\mathcal{C}$ and $(D_{\bar{\mathbf{C}}}\boldsymbol{\Sigma})^\mathsf{T}[\mathbf{M}] \in \mathrm{Sym}_2 \,\forall \mathbf{M} \in \mathrm{Lin}_2$, the latter following from $(D_{\bar{\mathbf{C}}}\boldsymbol{\Sigma})^\mathsf{T}[\mathbf{M}] \cdot \mathbf{W} = (D_{\bar{\mathbf{C}}}\boldsymbol{\Sigma})[\mathbf{W}] \cdot \mathbf{M} = \mathbf{0} \cdot \mathbf{M} = 0$ for every $\mathbf{W} \in \mathrm{Skw}_2$ and for every $\mathbf{M} \in \mathrm{Lin}_2$.

We next observe that $D_{\mathbf{C}}\boldsymbol{\Sigma} \in \mathrm{Sym}_4$ and that $D_{\mathbf{C}}\boldsymbol{\Sigma}[\mathbf{M}] \in \mathrm{Sym}_2 \,\forall \mathbf{M} \in \mathrm{Lin}_2$, so that the derivative of the Lagrangian with respect to the deformation reads

$$D_f\mathscr{L}[\mathbf{v}] = -\frac{1}{|\omega|} \int_\omega \left(\nabla\boldsymbol{\eta}\boldsymbol{\Sigma} + 2\mathbf{F}(D_{\mathbf{C}}\boldsymbol{\Sigma})[\mathbf{F}^\mathsf{T}\nabla\boldsymbol{\eta}]\right) \cdot \nabla\mathbf{v} = 0, \quad \forall \mathbf{v} \in T_f M. \tag{2.11}$$

Upon introducing the definition of $\mathbf{A} := \nabla\boldsymbol{\eta}\boldsymbol{\Sigma} + 2\mathbf{F}(D_{\mathbf{C}}\boldsymbol{\Sigma})[\mathbf{F}^\mathsf{T}\nabla\boldsymbol{\eta}]$, equation (2.11) yields

$$\int_\Gamma \mathbf{An} \cdot \mathbf{v} - \int_\omega \mathrm{Div}\,\mathbf{A} \cdot \mathbf{v} = 0, \quad \forall \mathbf{v} \in T_f M, \tag{2.12}$$

which, thanks to the characterization of the tangent space to M, is equivalent to

$$\int_\omega \mathrm{Div}\,\mathbf{A} \cdot \mathbf{v} = 0, \quad \forall \mathbf{v} \in C_c^\infty(\omega) \subseteq T_f M, \qquad \int_\Gamma \mathbf{An} \cdot \mathbf{Pa} = 0, \quad \forall \mathbf{a} \in V_\Gamma, \tag{2.13}$$

leading to

$$\mathrm{Div}\,\mathbf{A} = \mathbf{0} \quad \text{in } \omega, \qquad \mathbf{PAn} = \mathbf{0} \quad \text{on } \Gamma. \tag{2.14}$$

---

[3]Recall that the divergence of a third order tensor field Ξ is defined by $\mathrm{Div}\,\Xi \cdot \mathbf{A} = \mathrm{Div}\,(\Xi^\mathsf{T}\mathbf{A})$ for any constant $\mathbf{A} \in \mathrm{Lin}_2$, where the transpose operation reads as $\mathbf{a} \cdot \Xi^\mathsf{T}\mathbf{A} = \Xi\mathbf{a} \cdot \mathbf{A}$ for any constant $\mathbf{A} \in \mathrm{Lin}_2$ and $\mathbf{a} \in \mathbb{R}^2$. Then, $\mathrm{Div}\,\Xi \cdot \mathbf{A} + \Xi \cdot \nabla\mathbf{A} = \mathrm{Div}\,(\Xi^\mathsf{T}\mathbf{A})$ where $\mathbf{A}$ is a second order tensor field.

Finally, the derivative of the Lagrangian with respect to $\boldsymbol{\eta}$ trivially provides equation (2.2) of mechanical equilibrium. Hence, stationary points of the Lagrangian (2.7) are triplets $(\bar{\mathbf{C}}, f, \boldsymbol{\eta}) \in N \times M \times T_f V$ satisfying:

$$\nabla_{\bar{\mathbf{C}}} \mathcal{C} - (D_{\bar{\mathbf{C}}} \boldsymbol{\Sigma})^\mathsf{T} [\mathbf{F}^\mathsf{T} \nabla \boldsymbol{\eta}] = \mathbf{0} \quad \text{in } \omega\,, \qquad \mathbf{N} = \mathbf{0} \quad \text{on } \Gamma\,, \tag{2.15a}$$

$$\text{Div}\,\mathbf{A} = \mathbf{0} \quad \text{in } \omega\,, \qquad \mathbf{PAn} = \mathbf{0} \quad \text{on } \Gamma\,, \tag{2.15b}$$

$$\text{Div}\,\mathbf{F}\boldsymbol{\Sigma} = \mathbf{0} \quad \text{in } \omega\,, \qquad \mathbf{F}\boldsymbol{\Sigma}\mathbf{n} = \mathbf{0} \quad \text{on } \Gamma\,. \tag{2.15c}$$

Step 2: Homogeneous stress-free stationary points   Affine shape changes of homogeneous metric $\mathbf{C}$ achieved by the target metric $\bar{\mathbf{C}} = \mathbf{C}$ are stress-free. Under this condition, the problem of equations (2.15) simplifies to that of determining the pair $(f, \boldsymbol{\eta}) \in M \times T_f V$ such that:

$$\nabla_{\bar{\mathbf{C}}} \mathcal{C} - (D_{\bar{\mathbf{C}}} \boldsymbol{\Sigma})^\mathsf{T} [\mathbf{F}^\mathsf{T} \nabla \boldsymbol{\eta}] = \mathbf{0} \quad \text{in } \omega\,, \qquad \mathbf{N} = \mathbf{0} \quad \text{on } \Gamma\,, \tag{2.16a}$$

$$\text{Div}\,\mathbf{A} = \mathbf{0} \quad \text{in } \omega\,, \qquad \mathbf{PAn} = \mathbf{0} \quad \text{on } \Gamma\,, \tag{2.16b}$$

with $\mathbf{A} = 2\mathbf{F}(D_{\mathbf{C}}\boldsymbol{\Sigma})[\mathbf{F}^\mathsf{T}\nabla\boldsymbol{\eta}]$. These set of equations can be further simplified by recalling that $\tilde{\boldsymbol{\Sigma}}(\bar{\mathbf{C}}) := \boldsymbol{\Sigma}(\bar{\mathbf{C}}, \bar{\mathbf{C}}) = \mathbf{0} \,\forall\, \bar{\mathbf{C}} \in \text{PSym}_2$, which trivially implies $D_{\bar{\mathbf{C}}}\tilde{\boldsymbol{\Sigma}}(\bar{\mathbf{C}})[\mathbf{U}] = \mathbf{0} \,\forall\, \mathbf{U} \in \text{Sym}_2$. This condition, along with the minor symmetries[4] of $D_{\mathbf{C}}\boldsymbol{\Sigma}$ and $D_{\bar{\mathbf{C}}}\boldsymbol{\Sigma}$ provides

$$D_{\bar{\mathbf{C}}}\boldsymbol{\Sigma}(\bar{\mathbf{C}}, \bar{\mathbf{C}}) = -D_{\mathbf{C}}\boldsymbol{\Sigma}(\bar{\mathbf{C}}, \bar{\mathbf{C}})\,. \tag{2.17}$$

Using this result and the major symmetry of $D_{\mathbf{C}}\boldsymbol{\Sigma}$, from the first of equations (2.16a) we obtain $\mathbf{A} = -2\mathbf{F}\,\nabla_{\bar{\mathbf{C}}}\mathcal{C}$, which is homogeneous and thus trivially satisfies the first of equations (2.16b). By recalling that $\partial_\Xi \chi(\bar{\mathbf{C}}, \mathbf{0}) = \mathbf{0}$, the second of equations (2.16a) is satisfied, while the second of equations (2.16b) becomes:

$$\mathbf{PF}\,\partial_{\mathbf{G}}\chi(\bar{\mathbf{C}}, \mathbf{0})\mathbf{n} = \mathbf{0} \quad \text{on } \Gamma\,, \tag{2.18}$$

where we have exploited the definition of $\nabla_{\bar{\mathbf{C}}}\mathcal{C}$. Observe that this result is independent of the specific choices for the elastic energy density and for the complexity functional.

Step 3: Specialization to isotropic complexity   We now assume the complexity functional to be isotropic, so that a representation theorem for isotropic scalar functions [Gurtin, 1982] dictates that $\chi(\mathbf{G}, \cdot) = \varphi(\mathscr{I}_{\mathbf{G}})$, where $\mathscr{I}_{\mathbf{G}}$ is the list of principal invariants of $\mathbf{G}$. It then follows that

$$\partial_{\mathbf{G}}\chi(\bar{\mathbf{C}}, \mathbf{0}) = \varphi_1(\mathscr{I}_{\bar{\mathbf{C}}})\mathbf{I} + \varphi_2(\mathscr{I}_{\bar{\mathbf{C}}})\bar{\mathbf{C}}^{-1}\,, \tag{2.19}$$

with φ_1 and φ_2 scalar functions of the list of principal invariants of $\bar{\mathbf{C}}$. Hence $\partial_{\mathbf{G}}\chi(\bar{\mathbf{C}}, \mathbf{0}) \in \text{Sym}_2$ and shares its eigenvectors $\mathbf{v}_i$ with the target metric $\bar{\mathbf{C}}$. Denoting by λ_i^2 the eigenvalues of $\bar{\mathbf{C}} = \mathbf{C}$ and by μ_i those of $\partial_{\mathbf{G}}\chi(\bar{\mathbf{C}}, \mathbf{0})$, we write $\bar{\mathbf{C}} = \sum_i \lambda_i^2(\mathbf{v}_i \otimes \mathbf{v}_i)$ and $\partial_{\mathbf{G}}\chi(\bar{\mathbf{C}}, \mathbf{0}) = \sum_i \mu_i(\mathbf{v}_i \otimes \mathbf{v}_i)$. Also, by the polar decomposition theorem $\mathbf{F} = \mathbf{RU}$, with $\mathbf{U} = \sum_i \lambda_i(\mathbf{v}_i \otimes \mathbf{v}_i)$ and $\mathbf{R} \in \text{Orth}^+$, such that equation (2.18) can be recast as

$$\mathbf{PF}\,\partial_{\mathbf{G}}\chi(\bar{\mathbf{C}}, \mathbf{0})\mathbf{n} = \sum_i \left\{ \lambda_i \mu_i(\mathbf{v}_i \cdot \mathbf{n}) - \frac{\sum_k \mu_k(\mathbf{v}_k \cdot \mathbf{n})^2}{\sum_k \lambda_k^{-2}(\mathbf{v}_k \cdot \mathbf{n})^2}\lambda_i^{-1}(\mathbf{v}_i \cdot \mathbf{n}) \right\} \mathbf{Rv}_i = \mathbf{0} \quad \text{on } \Gamma\,, \tag{2.20}$$

---

[4]Indeed $D_{\bar{\mathbf{C}}}\boldsymbol{\Sigma}[\mathbf{W}] = D_{\mathbf{C}}\boldsymbol{\Sigma}[\mathbf{W}] = \mathbf{0} \,\forall\, \mathbf{W} \in \text{Skw}_2$.

which, since the eigenvectors $\mathbf{v}_i$ are mutually orthogonal, finally leads to

$$\lambda_i \mu_i (\mathbf{v}_i \cdot \mathbf{n}) - \frac{\sum\limits_k \mu_k (\mathbf{v}_k \cdot \mathbf{n})^2}{\sum\limits_k \lambda_k^{-2} (\mathbf{v}_k \cdot \mathbf{n})^2} \lambda_i^{-1} (\mathbf{v}_i \cdot \mathbf{n}) = 0 \quad \text{on } \Gamma \,, \tag{2.21}$$

for $i = \{1, 2\}$. The equation above is trivially satisfied whenever the outward normal $\mathbf{n}$ to the reference boundary Γ is an eigenvector of the target metric everywhere on Γ, a result that corresponds to condition *(i)* of Proposition 3. Differently, equation (2.21) reduces to

$$\lambda_1^2 \mu_1 - \lambda_2^2 \mu_2 = 0 \,, \tag{2.22}$$

which coincides with condition *(ii)* of Proposition 3.

2.5 Numerical approximation of optimal target metrics

Besides the study of affine shape changes, we are interested in determining the optimal target metrics for generic transformations and in exploring the role of mechanical stresses in the ensuing morphing strategies. To this aim, we solve the optimization problem (2.5) numerically. Specifically, we use a gradient-based method implemented in the SNOPT library [Alt, 1990, Gill et al., 2005] within the finite element software COMSOL Multiphysics. Since the Hausdorff distance does not admit in general a shape derivative, we adopt its smooth approximation $\tilde{d}_H$ as proposed in [Charpiat et al., 2005]:

$$\tilde{d}_H(\Gamma_1, \Gamma_2) = \langle \langle \langle d(\cdot, \cdot) \rangle^{\varphi}_{\Gamma_2} \rangle^{\rho}_{\Gamma_1}, \langle \langle d(\cdot, \cdot) \rangle^{\varphi}_{\Gamma_1} \rangle^{\rho}_{\Gamma_2} \rangle^{\theta} \,, \tag{2.23}$$

where $d(\cdot, \cdot)$ denotes the Euclidean distance in $\mathbb{R}^2$ and

$$\langle f \rangle^{\varphi}_{\Gamma} := \varphi^{-1} \left(\frac{1}{|\Gamma|} \int_{\Gamma} \varphi \circ f \right) \,, \qquad \langle a_1, a_2 \rangle^{\theta} := \theta^{-1} \left(\frac{\theta(a_1) + \theta(a_2)}{2} \right) \,. \tag{2.24}$$

Here $\varphi(\xi) = \phi^{\alpha}(\xi)$, with ϕ a smooth, positive, strictly decreasing function, $\rho(\xi) = \xi^{\beta}$, $\theta(\xi) = \xi^{\gamma}$, while α, β, γ are positive constants controlling the accuracy of the approximation, such that $\tilde{d}_H(\Gamma_1, \Gamma_2) \overset{\alpha, \beta, \gamma \to \infty}{\longrightarrow} d_H(\Gamma_1, \Gamma_2)$, for any pair of curves Γ_1 and Γ_2. Following [Charpiat et al., 2005], in our simulations we set $\alpha = \beta = 4$, $\gamma = 2$, and $\phi(\xi) = \exp[-\xi^2/(2\sigma^2)]/\sqrt{2\pi\sigma^2}$ with σ a small parameter that we choose of the order of the mesh size on Γ and $\bar{\Gamma}$. Hence, the optimization problem becomes that of (2.5) with d_H replaced by $\tilde{d}_H$ and we consider it to be solved with sufficient accuracy provided that $\tilde{d}_H \ll \ell$, with ℓ a characteristic length scale later specified. As for the material response, we choose a plane-strain, compressible neo-Hookean energy density [Nardinocchi et al., 2013] such that

$$\psi(\mathbf{C}, \bar{\mathbf{C}}) = \frac{\bar{J} G}{2} \left[\bar{\mathbf{C}}^{-1} \cdot \mathbf{C} - 2 \log \left(\frac{J}{\bar{J}} \right) - 2 \right] + \frac{\bar{J} \Lambda}{2} \log^2 \left(\frac{J}{\bar{J}} \right) \,. \tag{2.25}$$

In the equation above, $\bar{J} = (\det \bar{\mathbf{C}})^{1/2}$, while G and Λ denote the first and the second Lamé moduli, respectively. In the numerical implementation of the model, we choose the volumetric and

deviatoric components of the target metric as optimization variables, to guarantee the positive definiteness of $\bar{\mathbf{C}}$ by setting the constraint $\bar{J} > 0$, thus preventing the gradient-based solver to explore unfeasible controls.

In the following sections, we first benchmark our computational model against the theoretical result of Proposition 3 related to affine shape changes characterized by homogeneous target metrics and compute the numerical solution in cases where homogeneous target metrics are not optimal. Then, we study more complex shape changes and compare the numerical solutions obtained with different complexity functionals, which allow to select notable activation patterns (*e.g.*, conformal target metrics) that are relevant in applications. We remark that numerical results are reported in dimensionless form, with stress measures normalized by the shear modulus G and spatial coordinates rescaled by the relevant characteristic length ℓ.

2.5.1 Affine shape changes: Optimality of homogeneous target metrics

For the numerical study of affine shape changes and to test for their optimality under the conditions of Proposition 3, we introduce the following isotropic complexity functional

$$\mathcal{C}(\bar{\mathbf{C}}) = \frac{1}{|\omega|} \int_\omega \left(a_\mathrm{c}|\bar{\mathbf{C}} - \mathbf{I}|^2 + a_\mathrm{g}|\nabla\bar{\mathbf{C}}|^2 \right) , \tag{2.26}$$

where a_c and a_g are positive constants. In the simulations, we set the parameter $a_\mathrm{d} \gg (a_\mathrm{c}/\ell, a_\mathrm{g}/\ell^3)$, such that the actual shape, $f(\Gamma)$, approximates the target shape, $\bar{\Gamma}$, with sufficient accuracy. We observe that, with the choice of (2.26), the eigenvalues of $\partial_\mathbf{G}\chi(\bar{\mathbf{C}}, \mathbf{0})$ are $\mu_i = a_\mathrm{c}(\lambda_i^2 - 1)$, so that the only feasible solution to equation (2.22) reads $\lambda_1 = \sqrt{1 - \lambda_2^2}$ and requires that $\lambda_i < 1$ for $i = \{1, 2\}$. This solution, which fulfills condition *(ii)* of Proposition 3, will be explored later in this section.

We first consider the transformation of a square having edge length ℓ into a rectangle having edges of length $\lambda\ell$ and ℓ, with the basis vectors $(\mathbf{e}_1, \mathbf{e}_2)$ aligned along the edges of the reference square (Fig. 2.3a). Clearly, this shape change can be achieved without stress by a uniaxial stretch such that the actual and the target metrics are homogeneous and both equal to $\bar{\mathbf{C}}^\mathrm{us} = \lambda^2 \mathbf{e}_1 \otimes \mathbf{e}_1 + \mathbf{e}_2 \otimes \mathbf{e}_2$. According to condition *(i)* of Proposition 3, this affine shape change is optimal, since the outward normal to the reference domain is an eigenvector of $\bar{\mathbf{C}}_\mathrm{us}$ everywhere on Γ. This conclusion is supported by the numerical results shown in Figs. 2.3a-d, which were obtained by setting $\mathbf{C} = \bar{\mathbf{C}} = \bar{\mathbf{C}}^\mathrm{us}$ as the initial condition for the optimization procedure. Indeed, the discrepancy between the components of $\bar{\mathbf{C}}^\mathrm{us}$ and of the (computed) optimal target metric are negligible (Figs. 2.3b-d), so as the norm of the (dimensionless) Cauchy stress (Fig. 2.3a).

We next study the transformation of a circle of radius ℓ into an ellipse of semi-axes $\lambda\ell$ and ℓ (Fig. 2.3e). While this transformation could be obtained by the target metric $\bar{\mathbf{C}}^\mathrm{us}$ of the previous case, this is not optimal for a circular domain since the conditions of Proposition 3 are not met. Indeed, we notice that the optimal target metric is not uniform (Figs. 2.3f-h) and it differs from the actual metric, such that the solution to the optimization problem is characterized by a non-homogeneous stress field (Fig. 2.3e). A similar result holds for the case of a square domain with edge length ℓ morphing into a parallelogram of height and basis ℓ (Figs. 2.4a-d). Here, the homogeneous shear deformation corresponding to the (actual and target) metric $\bar{\mathbf{C}}^\mathrm{s} = \mathbf{I} + \gamma(\mathbf{e}_1 \otimes \mathbf{e}_2 + \mathbf{e}_2 \otimes \mathbf{e}_1) + \gamma^2 \mathbf{e}_2 \otimes \mathbf{e}_2$ is not optimal. We argue that the two cases just discussed are instances of how stresses can be exploited to reduce the complexity of the controls or the material architecture. However, in this regard, it is important to remark that the heterogeneity of the optimal solutions is a purely geometrical fact, hence it is not subordinate to the presence of stresses.
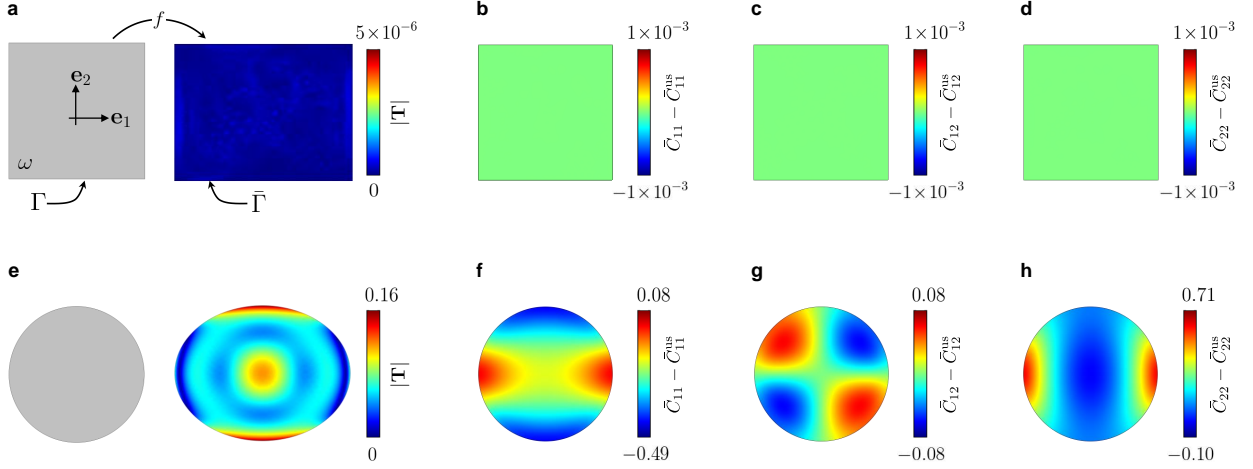
Figure 2.3: Optimal solutions for the transformation of a square into a rectangle and of a circle into an ellipse. Notice that these shape changes can be achieved through the same uniaxial stretch of actual and target metric equal to $\bar{\mathbf{C}}^{\mathrm{us}} = \lambda^2 \, \mathbf{e}_1 \otimes \mathbf{e}_1 + \mathbf{e}_2 \otimes \mathbf{e}_2$, with $\lambda = 1.3$. For both the cases, we report the norm of the (dimensionless) Cauchy stress and the components of $\bar{\mathbf{C}} - \bar{\mathbf{C}}^{\mathrm{us}}$. As predicted by the theoretical results of Proposition 3, $\mathbf{C} = \bar{\mathbf{C}} = \bar{\mathbf{C}}^{\mathrm{us}}$ is the optimal solution for the square domain (a-d). This is not the case of the circular domain, for which the optimal target metric is neither uniform nor corresponding to the actual metric, such that a state of stress characterizes the solution (e-h). Numerical results were obtained for $G/\Lambda = 1$ and with the following sets of parameters: $a_{\mathrm{c}} = 2 \times 10^{-2}$, $a_{\mathrm{g}}/\ell^2 = 2 \times 10^{-4}$, $a_{\mathrm{d}}\ell = 10$ for the square and $a_{\mathrm{c}} = 2 \times 10^{-1}$, $a_{\mathrm{g}}/\ell^2 = 2 \times 10^{-3}$, $a_{\mathrm{d}}\ell = 1$ for the circle.

Indeed, for the two cases depicted in Fig. 2.3e and in Fig. 2.4a, homogeneous target metrics are not optimal even among the restricted set of *stress-free metrics*, as it can be shown by studying the following variational problem

$$\min_{f \in M} \{ \mathcal{C}(\mathbf{C}) \} \,, \tag{2.27}$$

for which detailed calculations are reported in Appendix B. We also remark that the optimality of homogeneous target metrics, corresponding to affine shape changes, is not an intrinsic property of the specific controls. It rather depends on the shape and on the orientation of the reference domain. As an example, we show that $\bar{\mathbf{C}}^{\mathrm{s}}$ is optimal when its eigenvectors are aligned with the outward normal to the boundary of the reference domain (Figs. 2.4e-h).

Finally, we consider the interesting case of a square having edge length ℓ morphing into a rhombus having edges of length $\ell/\sqrt{2}$, with the edges of the reference square oriented at $\pi/4$ with the basis vectors $(\mathbf{e}_1, \mathbf{e}_2)$, see Fig. 2.5a. It is immediate to verify that such transformation can be achieved by the biaxial stretch such that the actual and target metrics both correspond to $\bar{\mathbf{C}}^{\mathrm{bs}} = (1 - \lambda^2) \, \mathbf{e}_1 \otimes \mathbf{e}_1 + \lambda^2 \, \mathbf{e}_2 \otimes \mathbf{e}_2$. While condition *(i)* of Proposition 3 is not met, condition *(ii)* is, as discussed at the beginning of the present section. Consequently, the homogeneous (actual and target) metric $\bar{\mathbf{C}}^{\mathrm{bs}}$ is optimal, as verified by the numerical results (Figs. 2.5a-d).

In concluding this section, it is interesting to comment about the strategy by which the complexity functional (2.26) is minimized in cases where the optimal target metric is not homogeneous. In general, the optimal solution is achieved through a subtle interplay between the target metric components, hence it is intrinsically multi-dimensional. This behaviour may be appreciated by exploring, for instance, the computational results reported in Figs. 2.3f-h, where a decrease, with respect to the initial condition, of the target metric component $\bar{C}_{11}$ is accompanied by an increase
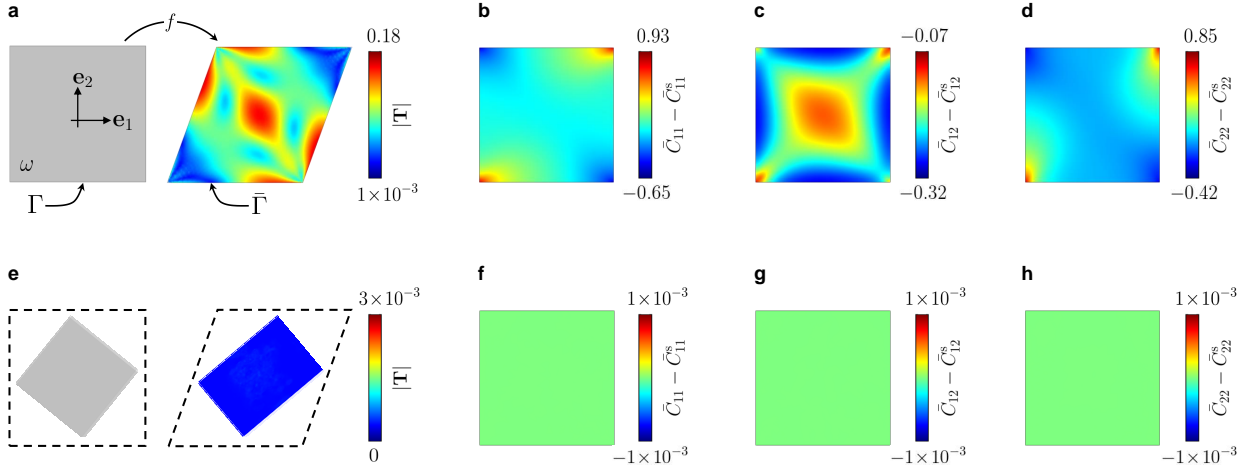
Figure 2.4: Optimal solutions for the transformation of a square into a parallelogram and of a square, with edges aligned along the eigenvectors of $\bar{\mathbf{C}}^{\mathrm{s}}$, into a rectangle. Both shape changes can be achieved through the simple shear of actual and target metric equal to $\bar{\mathbf{C}}^{\mathrm{s}} = \mathbf{I} + \gamma(\mathbf{e}_1 \otimes \mathbf{e}_2 + \mathbf{e}_2 \otimes \mathbf{e}_1) + \gamma^2\,\mathbf{e}_2 \otimes \mathbf{e}_2$, with $\gamma = \tan(\pi/9)$. For both the cases, we report the norm of the (dimensionless) Cauchy stress and the components of $\bar{\mathbf{C}} - \bar{\mathbf{C}}_{\mathrm{s}}$. Consistent with the theoretical results of Proposition 3, $\mathbf{C} = \bar{\mathbf{C}} = \bar{\mathbf{C}}^{\mathrm{s}}$ is not the optimal solution for the fist case (a-d), in which the optimal target metric is neither uniform nor corresponding to the actual metric, such that a state of stress characterizes the solution. Instead, the optimality of $\bar{\mathbf{C}}^{\mathrm{s}}$ is confirmed by the numerical results in the second case (e-f) since condition (i) of Proposition 3 is met. Numerical results were obtained for $G/\Lambda = 1$ and with the following sets of parameters: $a_{\mathrm{c}} = 2 \times 10^{-1}$, $a_{\mathrm{g}}/\ell^2 = 2 \times 10^{-3}$, $a_{\mathrm{d}}\ell = 1$ for the first case and $a_{\mathrm{c}} = 2 \times 10^{-2}$, $a_{\mathrm{g}}/\ell^2 = 2 \times 10^{-4}$, $a_{\mathrm{d}}\ell = 6$ for the second case.

of the component $\bar{C}_{22}$ and by the emergence of $\bar{C}_{12}$. Clearly, such a strategy could not be exploited in a one-dimensional setting, for which the homogeneous solution is always optimal. Indeed, let us consider the one-dimensional counterpart of the optimization problem (2.27):

$$\min_{f \in M} \left\{ \int_0^1 \chi(C, C') \right\} , \tag{2.28}$$

where $M = \{f(X) : (0,1) \to \mathbb{R} \mid f(0) = 0, \; f(1) = \delta, \; f' > 0 \text{ in } (0,1)\}$ is the set of admissible deformations, $C = (f')^2$ is the associated (scalar-valued) metric, and a prime denotes differentiation with respect to the spatial coordinate X. In this simplified case, the tangent space $T_f M$ trivially coincide with functions vanishing at the boundary. Hence, starting with the analog of (B.2) in the present one-dimensional setting, it is immediate to conclude that the *linear* deformation $f(X) = \delta X$ is always optimal.

2.5.2   Non-affine shape changes

In this section, we extend the numerical study of optimal target metrics to generic transformations, *i.e.*, those shape changes which are not achievable through homogeneous deformations. In particular, we focus on the prototypical case of the planar bending of an active block, due to its relevance in application (*e.g.*, soft robotics, smart actuation). Taking the rectangular domain of length ℓ and height $h = \ell/3$ as the reference configuration (Fig. 2.6a), the target shape $\bar{\Gamma}$ is chosen such that it can be realized through the conformal deformation

$$f^{\mathrm{c}}(X_1, X_2) = o + \ell(\lambda/\kappa)\left[\exp(\kappa X_2/\ell)\sin(\kappa X_1/\ell)\,\mathbf{e}_1 + (\exp(\kappa X_2/\ell)\cos(\kappa X_1/\ell) - 1)\,\mathbf{e}_2\right] , \tag{2.29}$$
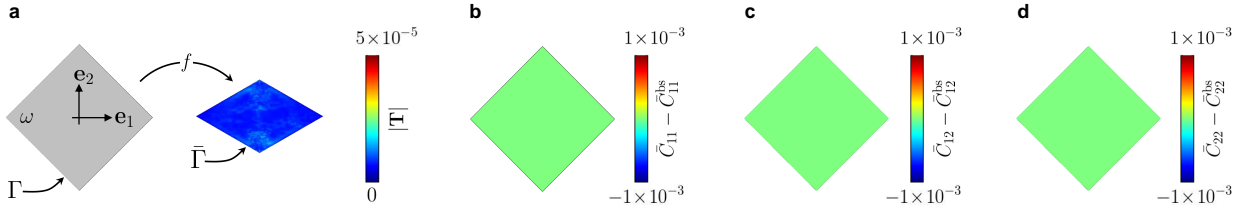
Figure 2.5: Optimal solution for the transformation of a square, with edges oriented at $\pi/4$ with respect to the basis vectors $(\mathbf{e}_1, \mathbf{e}_2)$, into a rhombus. Notice that this shape change can be achieved via the biaxial stretch of actual and target metrics equal to $\bar{\mathbf{C}}^{\mathrm{bs}} = (1 - \lambda^2)\,\mathbf{e}_1 \otimes \mathbf{e}_1 + \lambda^2\,\mathbf{e}_2 \otimes \mathbf{e}_2$, with $\lambda = 0.5$. This is the optimal solution, since the eigenvalues of $\bar{\mathbf{C}}^{\mathrm{bs}}$ satisfy condition (ii) of Proposition 3 for the complexity functional of (2.26). We report (a) the norm of the (dimensionless) Cauchy stress and (b-d) the components of $\bar{\mathbf{C}} - \bar{\mathbf{C}}^{\mathrm{bs}}$. Numerical results were obtained for $G/\Lambda = 1$ and with the following set of parameters: $a_{\mathrm{c}} = 2 \times 10^{-2}$, $a_{\mathrm{g}}/\ell^2 = 2 \times 10^{-3}$, $a_{\mathrm{d}}\ell = 10$.

where o is the origin of the reference frame, κ denotes the relative rotation (the amount of bending) between the block edges at $X_1 = \pm \ell/2$, whereas the dimensionless parameter λ controls local volume changes. Indeed, $J^{\mathrm{c}} = \lambda^2 \exp(2\kappa X_2/\ell)$, such that the associated conformal metric reads $\mathbf{C}^{\mathrm{c}} = J^{\mathrm{c}}\mathbf{I}$, a particularly useful choice since it provides a compatible *stress-free* initial condition for the optimization solver that exactly matches the target shape. In particular, we set $\kappa = \pi/8$ and $\lambda = 1.3$ in equation (2.29) for the numerical simulations. In the following, we explore the impact on optimal solutions of several complexity functional, some of them inspired by features of existing active materials (*e.g.*, polymer gels, liquid crystal elastomers). In particular, we will see how stresses contribute to reduce the complexity of the controls.

Figure 2.6: Optimal active bending of a block for the complexity functional $\mathcal{C}_1$. Prescribed shape change (a) for $\kappa = \pi/8$ and $\lambda = 1.3$ in equation (2.29) and dimensionless norm of the Cauchy stress $|\mathbf{T}|$. The dashed line in (a) denotes the cut-line for the plots in (b) relative to the target metric components $\bar{C}_{11}$ (blue curve), $\bar{C}_{22}$ (red curve), $\bar{C}_{12}$ (purple curve) and J^{c} (yellow curve). In (c-e) the contour plots of the target metric components $\bar{C}_{11}$, $\bar{C}_{12}$, and $\bar{C}_{22}$. Notice that the planar bending of the block is achieved by modulating only the axial strain along the vertical coordinate. Numerical results were obtained for $G/\Lambda = 1$ and with the following set of parameters: $a_{\mathrm{g}}/\ell^2 = 2 \times 10^{-3}$, $a_{\mathrm{d}}\ell = 10$.

We first consider the minimal case where the complexity functional is just characterized by a

term that penalizes the gradient of the controls, such that

$$\mathcal{C}_1(\bar{\mathbf{C}}) = \frac{1}{|\omega|} \int_\omega a_\mathrm{g} |\nabla \bar{\mathbf{C}}|^2 \,. \tag{2.30}$$

Relevant computational results are reported in Fig. 2.6 and comprise the norm of the Cauchy stress tensor (Fig. 2.6a) and the three components of the optimal target metric (Fig. 2.6b-e), for which we also provide plots along the cut-line of $X_1 = 0$. We notice that the target shape is accurately attained, as $f(\Gamma)$ and $\bar{\Gamma}$ almost overlap. Moreover, optimal solution is characterized by the emergence of stresses, which contribute to decrease the norm of the controls gradient, and is almost invariant along the X_1-coordinate, except for boundary layers that develop at the block extremities $X_1 = \pm \ell/2$ to satisfy the traction-free conditions. Finally, the (optimal) target metric component $\bar{C}_{11}$ approaches J^c from the conformal map (2.29), while $\bar{C}_{12}$ and $\bar{C}_{22}$ are essentially constant. Clearly, this behavior is produced by the penalty term in eq. (2.30): as the reference domain develops mainly horizontally, its planar bending is achieved by modulating only the axial strain along the vertical coordinate.
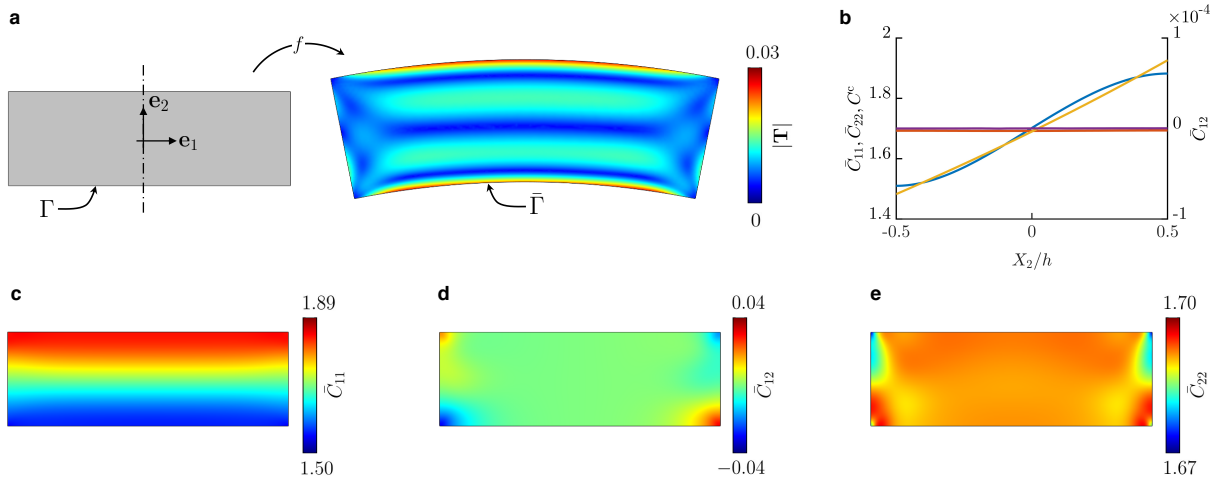

Figure 2.7: Optimal active bending of a block for the complexity functional $\mathcal{C}_2$. Prescribed shape change (a) for $\kappa = \pi/8$ and $\lambda = 1.3$ in equation (2.29) and dimensionless norm of the Cauchy stress $|\mathbf{T}|$. The dashed line in (a) denotes the cut-line for the plots in (b) relative to the target metric components $\bar{C}_{11}$ (blue curve), $\bar{C}_{22}$ (red curve), $\bar{C}_{12}$ (purple curve) and J^c (yellow curve). In (c-e) the contour plots of the target metric components $\bar{C}_{11}$, $\bar{C}_{12}$, and $\bar{C}_{22}$. Notice that the optimal target metric almost matches the conformal one, modulo discrepancies due to the emergence of mechanical stress. Numerical results were obtained for $G/\Lambda = 1$ and with the following set of parameters: $a_\mathrm{g}/\ell^2 = 2 \times 10^{-4}$, $a_\mathrm{dev}/\ell^2 = 2 \times 10^{-1}$, $a_\mathrm{d}\ell = 10$.

Inspired by polymer gels, active materials that typically swell or shrink isotropically in response to an external stimulus [Lucantonio et al., 2013], we next consider a complexity functional that penalizes the deviatoric part of the target metric, such that

$$\mathcal{C}_2(\bar{\mathbf{C}}) = \frac{1}{|\omega|} \int_\omega \left(a_\mathrm{g} |\nabla \bar{\mathbf{C}}|^2 + a_\mathrm{dev} |\bar{\mathbf{C}}^\mathrm{dev} - \mathbf{I}|^2 \right) \,. \tag{2.31}$$

As intuitively clear, setting $a_\mathrm{dev} \gg a_\mathrm{g}/\ell^2$ in (2.31) leads to an optimal target metric that is almost conformal. This conclusion is supported by the results reported in Fig. 2.7, where the target metric components $\bar{C}_{11}$ and $\bar{C}_{22}$ closely match (Fig. 2.7b), while the component $\bar{C}_{12}$ is almost zero apart

from boundary layers, as already discussed. Hence, a hydrogel-like behaviour is captured by the optimization procedure. However, the solution is characterized by stresses (Fig. 2.7a), such that the optimal target metric $\bar{\mathbf{C}} \neq \mathbf{C}^c$.
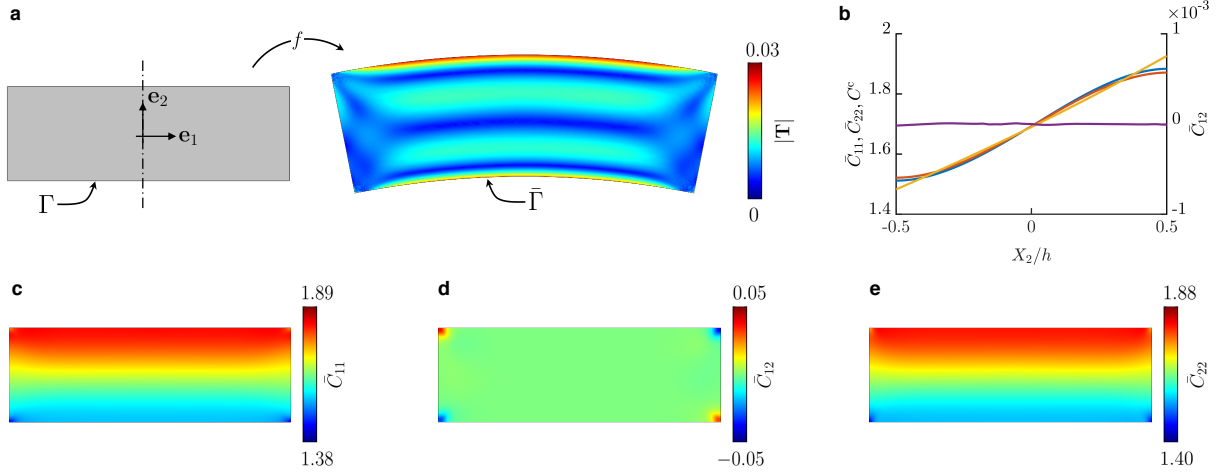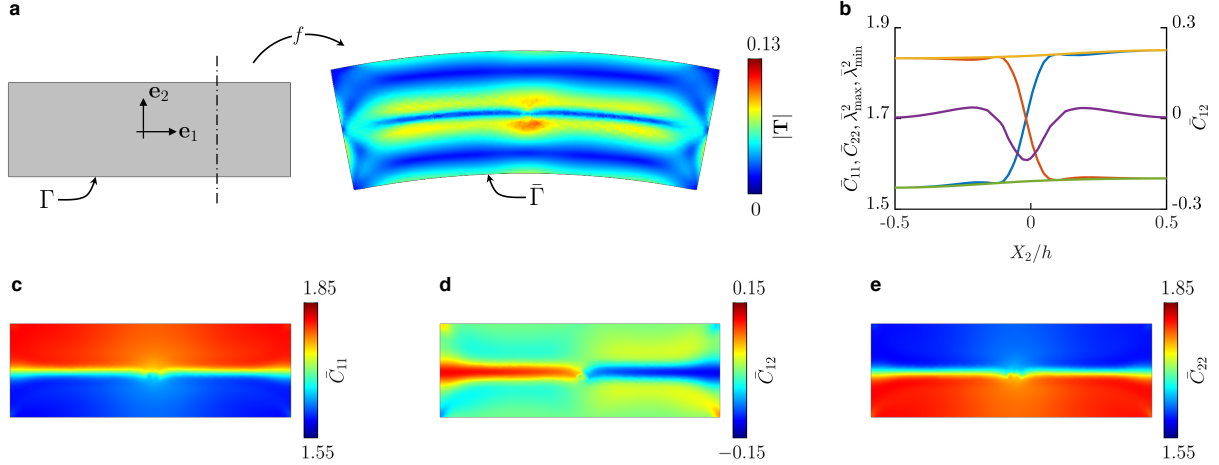

Figure 2.8: Optimal active bending of a block for the complexity functional $\mathcal{C}_3$. Prescribed shape change (a) for $\kappa = \pi/8$ and $\lambda = 1.3$ in equation (2.29) and dimensionless norm of the Cauchy stress $|\mathbf{T}|$. The dashed line in (a) denotes the cut-line for the plots in (b) relative to the target metric components $\bar{C}_{11}$ (blue curve), $\bar{C}_{22}$ (red curve), $\bar{C}_{12}$ (purple curve), $\bar{\lambda}^2_{\max}$ (yellow curve) and $\bar{\lambda}^2_{\min}$ (green curve). In (c-e) the contour plots of the target metric components $\bar{C}_{11}$, $\bar{C}_{12}$, and $\bar{C}_{22}$. Notice that the target metric eigenvalues are almost constant along the cut-line shown in (a). A bilayer structure naturally emerges from the optimization procedure as characterized by a region of sharp transition of the target metric components that divides the reference domain into two halves. Numerical results were obtained for $G/\Lambda = 1$ and with the following set of parameters: $a_g/\ell^2 = 2 \times 10^{-4}$, $a_e/\ell^2 = 2 \times 10^{-1}$, $a_d\ell = 20$.

Finally, we study the interesting case where the complexity functional weights the gradient of the maximum, $\bar{\lambda}^2_{\max}$, and of the minimum, $\bar{\lambda}^2_{\min}$, eigenvalues of the target metric:

$$\mathcal{C}_3(\bar{\mathbf{C}}) = \frac{1}{|\omega|} \int_\omega \left(a_g |\nabla \bar{\mathbf{C}}|^2 + a_e \left(|\nabla \bar{\lambda}^2_{\max}|^2 + |\nabla \bar{\lambda}^2_{\min}|^2 \right) \right) . \tag{2.32}$$

This choice is inspired by nematic elastomers, a class of active materials in which macroscopic distorsions are caused by temperature-driven molecular re-orientation (nematic-to-isotropic transition) and are characterized by homogeneous active stretches in the direction parallel and orthogonal to the nematic director [Sawa et al., 2010]. By setting $a_e \gg a_g$ in the numerical simulations, the optimization procedure leads to the emergence of a bilayer structure (Fig. 2.8), *i.e.* the solution is piecewise constant, except for a region of sharp transition that divides the reference domain into two halves. This phenomenon is reminiscent of phase transitions where two or more phases are separated by an interface. We argue that the transition region may converge to a discontinuity in the limit of $a_g \to 0$. As in the cases previously discussed, the optimal solution is characterized by stresses (Fig. 2.8a) and, as expected, the eigenvalues of the target metric are nearly constant (Fig. 2.8b), while the target metric components $\bar{C}_{11}$ and $\bar{C}_{22}$ swap their values about the sharp horizontal interface centered at $X_2 = 0$, see Fig. 2.8c and Fig. 2.8e. Consequently, the eigenvectors of the target metric undergo a rotation of $\pi/2$ within that interface, and such rotation is accompanied by the occurrence of $\bar{C}_{12}$ of sensible magnitude (Fig. 2.8d). Because of the symmetry of the optimization problem about the vertical coordinate, the rotation of the eigenvectors of the target

metric takes place in opposite directions on the two halves of the reference domain, such that no rotation takes place at the center by continuity.
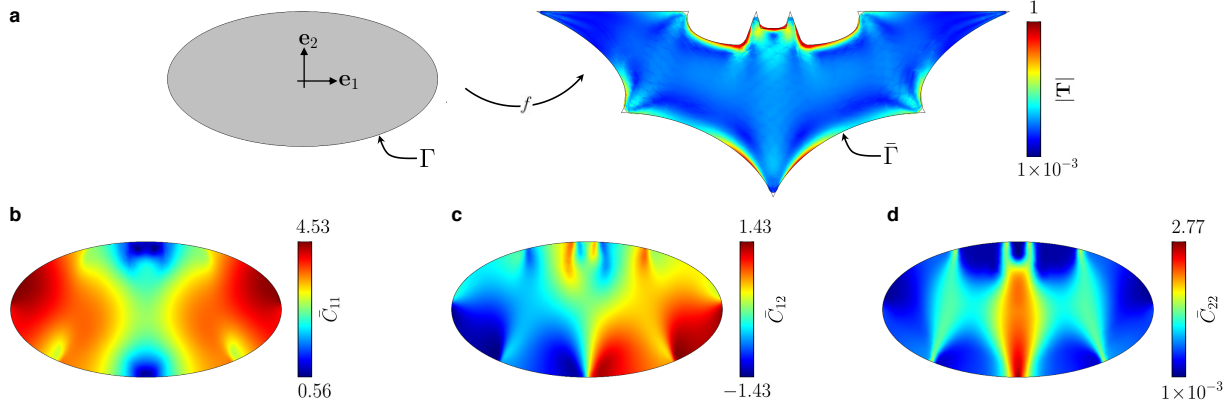

Figure 2.9: Optimal solution exploiting $\mathcal{C}_1$ as the complexity functional for the transformation of an ellipse into a shape resembling a batman-like logo. Prescribed shape change (a) and dimensionless norm of the Cauchy stress $|\mathbf{T}|$. In (b-d) the contour plots of the optimal target metric components $\bar{C}_{11}$, $\bar{C}_{12}$, and $\bar{C}_{22}$. Despite the presence of sharp corners, the numerical procedure is capable to achieve the target shape with remarkable accuracy, thus confirming the possibility to deal with extreme shape changes. Numerical results were obtained for $G/\Lambda = 1$ and with the following set of parameters: $a_{\mathrm{g}}/\ell^2 = 2 \times 10^{-4}$, $a_{\mathrm{d}}\ell = 10$.

To emphasize the applicability of the proposed approach in a more general context, we conclude this section by presenting the numerical results relevant for the shape change depicted in Fig. 2.9a and concerning the morphing of an ellipse of semi-axes ℓ and $\ell/2$ into a complex shape resembling a batman-like logo. As for the test case just discussed, we report the magnitude of the Cauchy stress (Fig. 2.9a) as well as the components of the optimal target metric (Fig. 2.9b-d), where the optimality is intended in the sense of the complexity functional $\mathcal{C}_1$. Despite the presence of sharp corners, the numerical procedure is capable to achieve the target shape with remarkable accuracy, thus confirming the possibility to deal with extreme shape changes.

2.6   Conclusions

Motivated by the quest for effective solutions to shape morphing problems, we formulated a constrained optimal control problem for the determination of the optimal target metric field corresponding to a prescribed shape change. We introduced an objective functional accounting for the complexity of the controls and for the distance between the realized and the target shape. In particular, we explored the planar morphing of active elastic bodies under plane-strain conditions and in the absence of external forces. For the special case of shape transformations achievable via affine mappings, we derived explicit necessary and sufficient conditions for the optimality of homogeneous target metrics. We verified our theoretical findings by means of numerical simulations, later extended to the study of more complex shape changes. While providing evidence of the applicability of our approach to generic shape transformations, we focused on the prototypical case of the active planar bending of a block. In particular, we investigated the effect of different complexity functionals on the optimal target metric. In our opinion, the relevance of the presented case study is twofold. On the one hand, it shows that the appropriate choice of a complexity func-

tional leads to the optimal design of target metrics compatible with a specific material class (*e.g.*, polymer gels, nematic elastomers). On the other hand, it highlights that our computational tool may be employed to devise novel morphing strategies or material architectures, where stresses promote a reduction in the complexity of the controls. Finally, we envisage the applicability of our approach to the study of biological systems, as it may contribute to gather insight into the morphing strategies they adopt as a result of natural selection.

Chapter 3

The effect of cortex contractility and axoplasm integrity in the active reconfigurations of axons

3.1 Introduction

Axons are fundamental structures of neurons whose purpose is the transmission of electro-chemical signals to neighbouring cells. The inner part, called *axoplasm*, is the cytoplasm of axons and contains several organelles and microtubules. The latter are cross-linked together forming a network which gives the axoplasm an elastic behaviour. The axoplasm is surrounded by a coating, called *cortex*, composed of F-actin filaments interconnected together by myosin II molecular motors and spectrin. In particular, the F-actin cortex can actively contract thanks to the action of myosin II. The interplay between the microtubule network and the cortical actomyosin machinery aims at maintaining the cylindrical shape of the axon [Ouyang et al., 2013].

Many phenomena can alter such a delicate dynamic equilibrium. In particular, the disruption of the elastic component of the axoplasm during stretch can lead to bulging along the axon, a process called axonal *beading* or *pearling* that is a hallmark of neuronal damage [Lang et al., 2017, Datar et al., 2019]. Indeed, axons can sustain large deformations, up to 100%, if the strain is slowly and progressively imposed [Tang-Schomer et al., 2009]. Under such conditions, the elastic deformation can even induce an axial growth of the axon thanks to the production of new microtubules [Bray, 1984, Zheng et al., 1991, Chada et al., 1997, Oliveri and Goriely, 2022]. Conversely, a rapid stretch of the axon can lead to a damage of the cytoskeleton and to the depolymerisation of microtubules [Tang-Schomer et al., 2009, Bain and Meaney, 2000].

Axonal beading has been observed as a consequence of several pathological conditions, such as the Alzheimer's [Stokin et al., 2005] and Parkinson's diseases [Tagliaferro and Burke, 2016], viral infections [Jacomy et al., 2006], and multiple sclerosis [Nikić et al., 2011]. There is increasing evidence that all these conditions result in a structural damage of the cytoskeleton. Indeed, it has been shown that axonal beading can be explained by a mechanical instability triggered by both the reduction of axoplasm stiffness and the active contraction of the F-actin cortex [Riccobelli, 2021]. Therefore, unveiling the mechanism underlying cortical contraction is of the utmost importance to understand how axons maintain their structural stability and to prevent their degeneration.

Experimental observations show that F-actin filaments are arranged in a geometrically regular

pattern, forming circles spaced at a constant distance of $180\,\mathrm{nm}$-$190\,\mathrm{nm}$ along the axonal length, interconnected by spectrin and myosin II [Xu et al., 2013]. Such a microstructural organisation suggests that the F-actin cortex can generate an active tension in both the axial and the circumferential direction. Recent experiments have linked hoop contractility to the self-regulation of the axon diameter following an externally imposed axial stretch, microtubule depolymerisation or myosin II disruption [Fan et al., 2017, Costa et al., 2020]. In these works, the authors suggest that such changes may be induced by the compressive force exerted on the axoplasm by the active contraction of the cortex [Fan et al., 2017]. Furthermore, an active diameter reduction is observed when axons are axially stretched, suggesting a coupling between axial and hoop active tensions. However, the nature of such a coupling is still not understood.

In this Chapter, we use tools of Continuum Mechanics to investigate the non-trivial coupling of the axial and circumferential active contraction, showing that the cortex contractility induces a compression of the axoplasm. The Chapter is organized as follows: in Section 3.2 we propose a continuum model of the axon exploiting the active strain approach and the Coleman-Noll procedure to obtain evolution equations coupling the hoop and the axial active stretch. Under the simplifying assumption of material incompressibility, in Section 3.3 we show that the above mentioned equations reduce to a simple dynamical system that can be easily studied analytically. A more appropriate compressible behavior is assumed in Section 3.4, where we numerically approximate the mathematical model and we provide a quantitative comparison with experimental results. Finally, in Section 3.4.6 we discuss the main outcomes of the present work together with some concluding remarks.

3.2   Mathematical model

The aim of this Section is to construct a mathematical model of F-actin cortex contraction and to investigate the coupling between the axial and the circumferential contractility using the framework of Continuum Mechanics.

3.2.1   Notation and kinematics

We model the axon as a continuum body with reference configuration

$$\Omega_0 = \left\{ \mathbf{X} \in \mathbb{E}^3 \mid R \in [0,\, R_{\mathrm{o}}],\, \Theta \in [0,\, 2\pi],\, Z \in \mathbb{R} \right\},$$

where R, Θ, Z are the Lagrangian cylindrical coordinates of $\mathbf{X} = R\cos\Theta\,\mathbf{e}_R + R\sin\Theta\,\mathbf{e}_\Theta + Z\mathbf{e}_Z$ denoting the position vector of material points belonging to the three dimensional Euclidean space $\mathbb{E}^3$. Due to the slenderness of the axon we assume the reference domain to be infinite along $\mathbf{e}_Z$.

The axon is composed of an inner part $\Omega_{0\mathrm{a}}$ and an outer coating $\Omega_{0\mathrm{c}}$, representing the axoplasm and the actomyosin cortex, respectively. More explicitly, we define

$$\Omega_{0\mathrm{a}} = \left\{ \mathbf{X} \in \Omega_0 \mid 0 \le R < R_{\mathrm{i}} \right\},$$
$$\Omega_{0\mathrm{c}} = \left\{ \mathbf{X} \in \Omega_0 \mid R_{\mathrm{i}} \le R \le R_{\mathrm{o}} \right\},$$

where R_{i} is the internal radius of the axoplasm.[1]

---

[1]Problems of this type, involving composite materials with cylindrical inclusions, have been extensively studied by means of analytical solutions in [Christensen and Lo, 1979, Ogden, 1997].
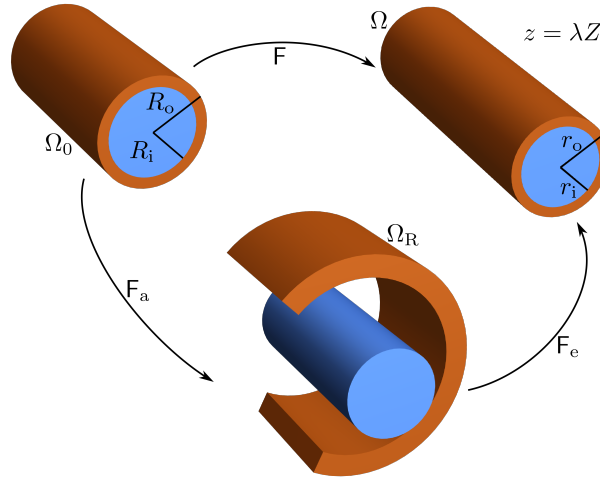
Figure 3.1: Representation of the multiplicative decomposition of the deformation gradient $\mathbf{F} = \mathbf{F}_e\mathbf{F}_a$.

Let $f : [t_0,\, t_1]\times\Omega_0 \to \mathbb{E}^3$ denote the motion of Ω_0, and $\mathbf{f}$ its corresponding position vector so that $\mathbf{x} = \mathbf{f}(t,\, \mathbf{X})$ is the actual position vector of point $\mathbf{X}$ at time t. We denote by $r,\, \theta,\, z$ the coordinate of $\mathbf{x}$ in a cylindrical reference frame where $(\hat{\mathbf{e}}_r,\, \hat{\mathbf{e}}_\theta,\, \hat{\mathbf{e}}_z)$ is the corresponding vector basis.

Let $\mathbf{F} = \nabla f$ be the deformation gradient. Since the cortex can actively contract, we exploit the active strain approach [Ambrosi and Pezzuto, 2011, Giantesio et al., 2018], a method first developed for modeling muscle contraction [Kondaurov and Nikitin, 1987, Taber and Perucchio, 2000, Nardinocchi and Teresi, 2007, Riccobelli and Ambrosi, 2019] which has been recently exploited to model axonal contractility [García-Grajales et al., 2017, Riccobelli, 2021]. More explicitly, we assume a multiplicative decomposition of the deformation gradient into an active and an elastic part

$$\mathbf{F} = \mathbf{F}_e\mathbf{F}_a,$$

where $\mathbf{F}_e$ and $\mathbf{F}_a$ account for the elastic and the inelastic active distortion, respectively. The tensor $\mathbf{F}_a$ describes the contractility of the cortex and has to be constitutively prescribed (see Fig. 3.1). We also denote by J, J_e, and J_a the determinants of the tensors $\mathbf{F}$, $\mathbf{F}_e$, and $\mathbf{F}_a$, respectively, representing the local change of volume induced by the relative distortion field.

Given the micro-structural organisation of the cortex, it is reasonable to assume that

$$\mathbf{F}_a = \frac{1}{a_\Theta a_Z}\mathbf{e}_R \otimes \mathbf{e}_R + a_\Theta\mathbf{e}_\Theta \otimes \mathbf{e}_\Theta + a_Z\mathbf{e}_Z \otimes \mathbf{e}_Z, \tag{3.1}$$

for $\mathbf{X} \in \Omega_{0c}$, where a_Θ and a_Z are the active stretches along the circumferential and the axial direction, respectively. In this way, the active strain tensor accounts for a pure remodelling of the cortex [Epstein, 2015], i.e. $J_a = 1$, without any volume modification (as would happen in growth/resorption). The axoplasm is treated as a deformable body composed of a passive elastic material, setting $\mathbf{F}_a = \mathbf{I}$ in Ω_{0a}, where $\mathbf{I}$ is the identity tensor.

3.2.2 Balance equations and boundary conditions

We follow the approach proposed in [DiCarlo and Quiligotti, 2002] to build a thermodynamically consistent model of cortex contractility. The main idea is to postulate the existence of remodelling

forces that drive the contraction of the cortex. Then, exploiting the Clausius-Duhem inequality, we derive some constitutive restrictions for the expressions of such forces. This approach is also known in Continuum Mechanics as the Coleman-Noll procedure [Coleman and Noll, 1974].

More explicitly, similarly to the modelling of growth [DiCarlo and Quiligotti, 2002], we prescribe a balance between the remodelling stresses driving cortex contractility as follows:

$$\begin{cases} B_\Theta = C_\Theta, \\ B_Z = C_Z, \end{cases} \tag{3.2}$$

where B_Θ and B_Z are the external remodelling stresses along the circumferential and the axial direction, while C_Θ and C_Z are the corresponding internal remodelling stresses.

As regards the balance of the linear momentum, in the absence of external body forces and neglecting inertia we get

$$\mathrm{Div}\, \mathbf{S} = \mathbf{0}\,, \tag{3.3}$$

where $\mathbf{S}$ is the first Piola-Kirchhoff stress tensor and Div represents the divergence in material coordinates. Equivalently, the balance of the linear momentum can be recast in the actual configuration, that is

$$\mathrm{div}\, \mathbf{T} = \mathbf{0}\,, \tag{3.4}$$

where $\mathbf{T} = J^{-1}\mathbf{S}\mathbf{F}^\mathsf{T}$ is the Cauchy stress tensor and div is the divergence operator in the actual reference frame.

The balance equations are complemented by proper boundary and interface conditions. We assume that the external boundary of the axon is free of traction, therefore

$$\mathbf{S}\mathbf{n} = \mathbf{0} \qquad \text{where } R = R_\mathrm{o}, \tag{3.5}$$

where $\mathbf{n}$ is the outward normal to Ω_0. We also enforce the continuity of displacement and traction at the interface between the cortex and the axoplasm, namely

$$\begin{cases} \lim_{R \to R_\mathrm{i}^-} \mathbf{u} = \lim_{R \to R_\mathrm{i}^+} \mathbf{u}, \\ \lim_{R \to R_\mathrm{i}^-} \mathbf{S}\mathbf{n} = \lim_{R \to R_\mathrm{i}^+} \mathbf{S}\mathbf{n}. \end{cases} \tag{3.6}$$

where $\mathbf{n}$ is the outward normal to the interface. To proceed, we must provide some constitutive assumptions on the material.

3.2.3 Thermodynamics restrictions and Coleman-Noll procedure

In the following, we exploit the so-called Coleman-Noll [Coleman and Noll, 1974] procedure based on the Clausius-Duhem inequality to deduce restrictions on the constitutive laws. This allows to formulate the coupling between the active stretches a_Θ and a_Z in a thermodynamically consistent manner.

Specifically, we postulate the existence of a strain energy density function ψ and, following [DiCarlo and Quiligotti, 2002], we write the Clausius-Duhem inequality

$$\int_\mathcal{P} \dot{\psi} \le \int_\mathcal{P} \mathbf{S} \cdot \dot{\mathbf{F}} + \int_{\mathcal{P} \cap \Omega_{0c}} \left[C_\Theta \frac{\dot{a}_\Theta}{a_\Theta} + C_Z \frac{\dot{a}_Z}{a_Z} \right]\,, \tag{3.7}$$

where $\mathcal{P}$ is a subdomain of Ω_0 and the superposed dot denotes the time derivative. We remark that the latter integral in the inequality (3.7), representing the power of the internal remodelling forces, is performed on $\mathcal{P} \cap \Omega_{0c}$ since only the cortex can actively contract.

By the equipresence principle [Truesdell and Noll, 1965], we postulate that the constitutive relations for ψ, C_Θ, C_Z, and $\mathbf{S}$ depend on the same kinematical quantities. Here, we assume that

$$\psi = \psi(\mathbf{X}, \mathbf{F}, a_j, \dot{a}_j),$$
$$C_j = C_j(\mathbf{X}, \mathbf{F}, a_j, \dot{a}_j),$$
$$\mathbf{S} = \mathbf{S}(\mathbf{X}, \mathbf{F}, a_j, \dot{a}_j),$$

where $j = \Theta, Z$.

Under such assumptions, we can rewrite (3.7), obtaining

$$\int_{\mathcal{P}} (\partial_{\mathbf{F}}\psi - \mathbf{S}) \cdot \dot{\mathbf{F}} + \sum_{j=\Theta, Z} \int_{\mathcal{P} \cap \Omega_{0c}} \left(a_j \, \partial_{a_j}\psi - C_j\right) \frac{\dot{a}_j}{a_j} + \int_{\mathcal{P} \cap \Omega_{0c}} \partial_{\dot{a}_j}\psi \, \ddot{a}_j \leq 0, \tag{3.8}$$

which must hold for any admissible process [Coleman and Noll, 1974, Podio-Guidugli, 2019]. Thus, from the arbitrariness of $\dot{\mathbf{F}}$ and $\ddot{a}_j$, we obtain

$$\mathbf{S} = \partial_{\mathbf{F}}\psi, \qquad \partial_{\dot{a}_j}\psi = 0, \tag{3.9}$$

where the first relation is the classical expression of the first Piola-Kirchhoff stress tensor of a hyperelastic material, while the second one states that the energy ψ is independent of $\dot{a}_\Theta$ and $\dot{a}_Z$.

We remark that the molecular motors can only generate an active contraction in the circumferential and the axial directions. Therefore, a_Θ must satisfy the unilateral constraint $a_\Theta \leq 1$, and similarly for a_Z. Considering the possible continuations on $\dot{a}_j$ for $j = \Theta, Z$ in (3.8), we can set [2]

$$C_j = a_j \, \partial_{a_j}\psi + \mu_c \tau_j \frac{\dot{a}_j}{a_j} + \Gamma_j, \tag{3.10}$$

where Γ_j is the reactive term enforcing the unilateral constraint $a_j \leq 1$ playing the role of a Lagrange multiplier. More into detail, Γ_j satisfies the following relations:

$$\begin{cases} \Gamma_j(a_j - 1) = 0, \\ \Gamma_j \geq 0. \end{cases} \tag{3.11}$$

We observe that Γ_j is zero whenever $a_j \neq 1$. Exploiting (3.2) and (3.10), we get

$$\dot{a}_j = \frac{a_j}{\mu_c \tau_j} \left(B_j - a_j \, \partial_{a_j}\psi - \Gamma_j\right). \tag{3.12}$$

If the constraint is binding (i.e. $a_j = 1$) with $\dot{a}_j|_{t=t_0} = 0$, from (3.12) we get

$$\Gamma_j = B_j - a_j \, \partial_{a_j}\psi,$$

---

[2]We stress that the restrictions on C_Θ and C_Z depend on the power of the remodelling forces postulated in (3.7). For an extensive discussion see [Goriely, 2017],§14. In addition we remark that the dissipative term in (3.10) is just one of the admissibile choices compatible with the Clausius-Duhem inequality, see [Ambrosi and Guana, 2005].

which holds whenever $\Gamma_j \geq 0$, namely when $B_j \geq a_j\,\partial_{a_j}\psi$. Conversely, if $B_j < a_j\,\partial_{a_j}\psi$, from (3.12) we observe that $\dot{a}_j|_{t=t_0}$ is negative, therefore leading to the detachment from the boundary of the constraint $a_j \leq 1$ if $a_j|_{t=t_0} = 1$.

In summary, when $a_j = 1$ the reactive term Γ_j is given by

$$\Gamma_j = \max\left\{0,\, B_j - a_j\,\partial_{a_j}\psi\right\}. \tag{3.13}$$

We now specialise the evolution equation (3.12) enforcing the multiplicative decomposition of the deformation gradient dictated by the active strain approach [Kondaurov and Nikitin, 1987, Taber and Perucchio, 2000]. Let ψ_0 be the strain energy density of the passive material, we define the active free energy density as

$$\psi(\mathbf{X},\, \mathbf{F},\, a_\Theta,\, a_Z) = \psi_0(\mathbf{X},\, \mathbf{F}\mathbf{F}_a^{-1}). \tag{3.14}$$

With the newly defined energy density in the equation above, from (3.9) we get

$$\mathbf{S} = \partial_{\mathbf{F}_e}\psi_0\,\mathbf{F}_a^{-\mathsf{T}}. \tag{3.15}$$

By using (3.14), we obtain

$$\partial_{a_j}\psi = -\mathbf{M} \cdot \left(\partial_{a_j}\mathbf{F}_a\right)\mathbf{F}_a^{-1}, \qquad \text{with } \mathbf{M} = \mathbf{F}_e^{\mathsf{T}}\,\partial_{\mathbf{F}_e}\psi_0, \tag{3.16}$$

where $\mathbf{M}$ denotes the Mandel stress tensor. Introducing the tensors

$$\mathbf{I}_\Theta = \mathbf{e}_\Theta \otimes \mathbf{e}_\Theta - \mathbf{e}_R \otimes \mathbf{e}_R,$$
$$\mathbf{I}_Z = \mathbf{e}_Z \otimes \mathbf{e}_Z - \mathbf{e}_R \otimes \mathbf{e}_R,$$

and combining the expression of $\mathbf{F}_a$ given by (3.1) with (3.16), we get

$$a_j\,\partial_{a_j}\psi = -\mathbf{M} \cdot \mathbf{I}_j. \tag{3.17}$$

Thus, substituting (3.17) into (3.12) and enforcing (3.13), we finally get

$$\dot{a}_j = \begin{cases} \dfrac{a_j}{\mu_c\tau_j}\left(B_j + \mathbf{M} \cdot \mathbf{I}_j\right), & \text{if } a_j < 1 \text{ or } B_j < -\mathbf{M} \cdot \mathbf{I}_j, \\[2mm] 0, & \text{otherwise,} \end{cases} \tag{3.18}$$

where again $j = \Theta,\, Z$.

The evolution equations (3.18) for a_Θ and a_Z can be used to provide a physical interpretation of the external remodelling stress in (3.2). As for growth processes studied in [DiCarlo and Quiligotti, 2002, Ambrosi and Guana, 2005], B_Θ and B_Z represent the external forces driving the active contraction of the cortex: when the linear combinations of the Mandel stress components $\mathbf{M} \cdot \mathbf{I}_\Theta$ and $\mathbf{M} \cdot \mathbf{I}_Z$ are equal to $-B_\Theta$ and $-B_Z$, respectively, the system is in chemo-mechanical equilibrium. Therefore, B_Θ and B_Z can be regarded as the equilibrium, or *homeostatic*, stresses towards which the system is led.

Despite sharing many similarities with models for growing tissues developed in [Ambrosi and Guana, 2005], there are some peculiarities. First, the active strain tensor is isochoric, namely $J_a = 1$. The effect of such a restriction is that the Mandel stress appears in (3.18) in place of the Eshelby stress (see for instance equations (2.24) and (3.2) in [Ambrosi and Guana, 2005]). Secondly, $\mathbf{F}_a$ is not

a generic tensor with positive determinant but belongs to the subset described by (3.1). Thus, only a particular combination of the Mandel stress components are involved in the evolution equations (3.18).

A similar approach has been recently adopted by Dehghany et al. in [Dehghany et al., 2020] to model F-actin contractility in axons. Compared with their work, inspired by the models of smooth muscles developed by Stålhand et al. [Stålhand et al., 2011], our model considers a more general active strain tensor where the active strains a_Θ and a_Z are initially decoupled and their coupling is provided by the Coleman-Noll procedure instead of being prescribed *a priori*. In particular, the assumption of a linear relationship between a_Θ and a_Z such as $a_Z = \beta a_\Theta$ can lead to problems in the passive limit, since $\mathbf{F}_a$ cannot be equal to the identity when $\beta \neq 1$. Furthermore, the approach presented in this Section, based on the balance equations proposed by DiCarlo and Quiligotti in [DiCarlo and Quiligotti, 2002], allows us to enlighten the key role of Mandel tensor in regulating the homeostatic stress within the axon.

3.2.4 Variational characterization

The model already introduced exhibits a variational structure, in particular, the equations in (3.18) are the gradient flow of an energy functional. In order to show it, let us first recast the free energy density as follows

$$\Psi(\mathbf{F}, a_j) = \begin{cases} \psi_0(\mathbf{F}\mathbf{F}_a^{-1}) & \text{on } \Omega_{0a}, \\ \psi_0(\mathbf{F}) & \text{on } \Omega_{0c}. \end{cases}$$

We then introduce the following energy functional

$$\mathscr{E}(\mathbf{F}, a_j) = \int_{\Omega_0} \left(\Psi(\mathbf{F}, a_j) - \sum_j B_j \chi_{\Omega_{0c}} \log a_j \right),$$

where $\chi_{\Omega_{0c}}$ is the characteristic function of Ω_{0c}. Now, for every fixed a_j, define f^* as a stationary point of $\mathscr{E}$, namely

$$D_f \mathscr{E}(\mathbf{F}^*, a_j)[\nabla \mathbf{v}] = \int_{\Omega_0} \partial_\mathbf{F} \Psi(\mathbf{F}^*, a_j) \cdot \nabla \mathbf{v} = 0, \qquad \forall \mathbf{v} \in T_f V_f \ \ f \in V_f, \tag{3.19}$$

where V_f is the functional space for f and $T_f V_f$ denotes its tangent space at the point f. Finally let us define the energy functional $\mathscr{E}^*$ and the density Ψ^* as

$$\mathscr{E}^*(a_j) = \mathscr{E}(\mathbf{F}^*, a_j), \quad \Psi^*(a_j) = \Psi(\mathbf{F}^*, a_j),$$

respectively.

We claim that the system of equations in (3.18) is a gradient flow of $\mathscr{E}^*$ in the variable $a = (a_\Theta, a_Z) \in V = V_\Theta \times V_Z$, subject to the constraint $0 \leq a_j \leq 1$ in Ω_{0c}. The latter can be conveniently rephrased as $\log(a_j) \leq 0$.

To properly formulate the gradient flow we have to choose a scalar product for the variations of a, namely, a scalar product for elements of the tangent space $T_a V$. The subsequent calculations will confirm that the proper choice for the scalar product is

$$(v, w) = \mu_c \sum_j \tau_j \int_{\Omega_0} \frac{1}{a_j^2} v_j w_j,$$

for every $v, w \in T_a V$. We remark that, the correct choice of a scalar product is typically dictated by the existence of a dissipation mechanism. Indeed, our model features the following dissipation power $\mathscr{D}$

$$\mathscr{D}(v) = \|v\|^2 = (v, v).$$

Finally, in order to account for the unilateral constraint $a_j \leq 1$ we introduce the following Lagrangian

$$\mathscr{L}(a_j, \phi_j) = \mathscr{E}^*(a_j) + \sum_j \int_{\Omega_0} \Gamma_j \chi_{\Omega_{0c}} \log a_j \,,$$

where the Γ_j's play the role of Lagrange multipliers.

At this point, we have introduced all the ingredients to properly formulate the gradient flow for the evolution of a, which is defined as

$$\dot{a} = -\nabla_a \mathscr{L}, \tag{3.20}$$

where $\nabla_a \mathscr{L}$ denotes the variational gradient of $\mathscr{L}$ with respect to the scalar product $(\cdot, \cdot)$. According to the representation theorem for linear functional in scalar product spaces, $\nabla_a \mathscr{L}$ is obtained as the solution of the following variational equation

$$D_a \mathscr{L}[v] = (\nabla_a \mathscr{L}, v), \qquad \forall v \in T_a V \quad \nabla_a \mathscr{L} \in T_a V \,. \tag{3.21}$$

The variation of $\mathscr{L}$ reads

$$
\begin{aligned}
D_a \mathscr{L}[v] &= \sum_j \int_{\Omega_0} \left(D_{a_j} \Psi^*(a_j)[v_j] + \frac{\Gamma_j \chi_{\Omega_{0c}}}{a_j} v_j - \frac{B_j \chi_{\Omega_{0c}}}{a_j} v_j \right) \\
&= \sum_j \int_{\Omega_0} \left(\partial_{a_j} \Psi(\mathbf{F}^*, a_j) v_j + \partial_{\mathbf{F}} \Psi(\mathbf{F}^*, a_j) \cdot D_{a_j} \mathbf{F}^*[v_j] + \frac{\Gamma_j \chi_{\Omega_{0c}}}{a_j} v_j - \frac{B_j \chi_{\Omega_{0c}}}{a_j} v_j \right) \\
&= \sum_j \int_{\Omega_0} \left(\partial_{a_j} \Psi(\mathbf{F}^*, a_j) + \frac{\Gamma_j \chi_{\Omega_{0c}}}{a_j} - \frac{B_j \chi_{\Omega_{0c}}}{a_j} \right) v_j \\
&= \sum_j \int_{\Omega_0} \frac{1}{a_j^2} \left(\partial_{a_j} \Psi(\mathbf{F}^*, a_j) a_j^2 + \Gamma_j \chi_{\Omega_{0c}} a_j - B_j \chi_{\Omega_{0c}} a_j \right) v_j,
\end{aligned}
$$

where in the third line we exploited the definition of f^* through Eq. 3.19. Then, thanks to the above equation, Eq. (3.21) becomes

$$
\begin{aligned}
\sum_j & \int_{\Omega_0} \frac{1}{a_j^2} \left(a_j^2 \partial_{a_j} \Psi + \Gamma_j \chi_{\Omega_{0c}} a_j - B_j \chi_{\Omega_{0c}} a_j \right) v_j \\
&= \sum_j \int_{\Omega_0} \frac{\tau_j \mu_c}{a_j^2} (\nabla_a \mathscr{L})_j v_j \quad \forall v \in T_a V \quad \nabla_a \mathscr{L} \in T_a V, \tag{3.22}
\end{aligned}
$$

where $(\nabla_a \mathscr{L})_j$ denote the projection of $\nabla_a \mathscr{L}$ onto the space V_j ($j = \Theta, Z$). Equation (3.22) can be trivially solved, thus leading to

$$(\nabla \mathscr{L})_j = \frac{1}{\tau_j \mu_c} \left(a_j^2 \partial_{a_j} \Psi + \Gamma_j \chi_{\Omega_{0c}} a_j - B_j \chi_{\Omega_{0c}} a_j \right). \tag{3.23}$$

Substitution of Eq. (3.23) into Eq. (3.20) then leads to Eq. (3.18). Finally, the complete set of equations for the model is recovered once we add the condition in Eq. (3.19), which is nothing but the weak form of the balance of linear momentum, and the Karush-Kuhn-Tucker conditions for the unilateral constraint, namely

$$\Gamma_j \log a_j = 0, \qquad \Gamma_j \geq 0. \tag{3.24}$$

Notice that Eq. (3.24) is equivalent to Eq. (3.11).

3.2.5 Symmetry assumptions

Supported by the experimental evidence [Fan et al., 2017] that the changes of the axonal external radius are invariant along $\mathbf{e}_Z$, we assume the axon deformation to be axisymmetric, enforcing the following simplified kinematics:

$$\mathbf{f}(t, \mathbf{X}) = r(t, R)\hat{\mathbf{e}}_r + \lambda Z \hat{\mathbf{e}}_z, \tag{3.25}$$

with $\lambda \in (0, +\infty)$ being the imposed axial stretch along Z. Thus, the deformation gradient reads

$$\mathbf{F} = \frac{\partial r}{\partial R}\hat{\mathbf{e}}_r \otimes \mathbf{e}_R + \frac{r}{R}\hat{\mathbf{e}}_\theta \otimes \mathbf{e}_\Theta + \lambda \hat{\mathbf{e}}_z \otimes \mathbf{e}_Z, \tag{3.26}$$

where $r(t, R) = R + u(t, R)$ with u representing the radial displacement. Under the assumption (3.25), the balance of the linear momentum (3.3) becomes the following scalar equation:

$$\frac{\mathrm{d}S_{RR}}{\mathrm{d}R} + \frac{S_{RR} - S_{\Theta\Theta}}{R} = 0, \tag{3.27}$$

where S_{RR} and $S_{\Theta\Theta}$ are the radial and the hoop components of the first Piola-Kirchhoff stress tensor, respectively. In terms of the Cauchy stress tensor the balance reads as:

$$\frac{\mathrm{d}T_{rr}}{\mathrm{d}r} + \frac{T_{rr} - T_{\theta\theta}}{r} = 0, \tag{3.28}$$

where T_{rr} and $T_{\theta\theta}$ are the radial and hoop components of $\mathbf{T}$. The balance of the linear momentum, either in material or spatial coordinates, must be solved with respect to the radial displacement u satisfying homogeneous Dirichlet boundary conditions $u(t, 0) = 0$ ensuring the continuity of the deformation field along the Z axis. Enforcing (3.25), the boundary condition (3.5) reduces to the scalar equation

$$S_{RR}|_{R=R_\mathrm{o}} = 0, \tag{3.29}$$

or, equivalently, in the actual configuration

$$T_{rr}|_{r=r_\mathrm{o}} = 0, \tag{3.30}$$

where $r_\mathrm{o} = r(t, R_\mathrm{o})$. Equation (3.27) endowed with the above mentioned boundary condition should be coupled with (3.18) to completely describe the dynamics of axons.

3.3   Qualitative analysis: the incompressible case

In the following, we analyse more into detail the evolution equations (3.18) when the axon is treated as an incompressible medium. Such a simplifying assumption allows us to provide analytical predictions on the existence and stability of equilibrium solutions of (3.18).

To impose the incompressibility constraint, we require that

$$J_e = \det \mathbf{F}_e = 1 \tag{3.31}$$

which, combined with the expression of the active strain tensor (3.1), implies that $\det \mathbf{F} = 1$ as well. The enforcement of the incompressibility constraint can be done by introducing a Lagrange multiplier p. Through standard steps, we get the following expressions for the Cauchy and the Mandel stress tensors:

$$\mathbf{T} = \partial_{\mathbf{F}_e} \psi_0 \, \mathbf{F}_e^\mathsf{T} - p\mathbf{I}, \qquad \mathbf{M} = \mathbf{F}_e^\mathsf{T} \, \partial_{\mathbf{F}_e} \psi_0 - p\mathbf{I}.$$

As a constitutive choice, we assume that both the cortex and the axoplasm are composed of incompressible neo-Hookean materials, that is

$$\psi_0(\mathbf{F}_e) = \frac{\mu}{2} \left(\mathbf{F}_e \cdot \mathbf{F}_e - 3 \right), \quad \mu = \begin{cases} \mu_a, & R < R_i, \\ \mu_c, & R \geq R_i, \end{cases} \tag{3.32}$$

where μ_a and μ_c are positive constants representing the shear moduli of the axoplasm and of the cortex, respectively. Using the constitutive assumption (3.32), we get the following expression for the Cauchy and the Mandel stress tensors:

$$\mathbf{T} = \mu \mathbf{F}_e \mathbf{F}_e^\mathsf{T} - p\mathbf{I}, \qquad \mathbf{M} = \mu \mathbf{F}_e^\mathsf{T} \mathbf{F}_e - p\mathbf{I}. \tag{3.33}$$

Looking for a radially symmetric solution in the form of (3.25) and using the incompressibility constraint $J = 1$ we get

$$r(t, R) = R/\sqrt{\lambda}$$

so that (3.26) becomes

$$\mathbf{F} = \frac{1}{\sqrt{\lambda}} \left(\hat{\mathbf{e}}_r \otimes \mathbf{e}_R + \hat{\mathbf{e}}_\theta \otimes \mathbf{e}_\Theta \right) + \lambda \hat{\mathbf{e}}_z \otimes \mathbf{e}_Z. \tag{3.34}$$

Using the balance of the linear momentum (3.28), we get

$$p(r) = k_1, \qquad\qquad\qquad 0 \leq r < r_i, \tag{3.35}$$

$$p(r) = k_2 + \frac{\left(a_\Theta^4 a_Z^2 - 1 \right) \mu_c \log(r)}{a_\Theta^2 \lambda}, \qquad\qquad r_i \leq r < r_o, \tag{3.36}$$

where $r_i = r(t, R_i)$, while k_1 and k_2 are constants to be determined exploiting the interface and the boundary conditions (3.6) and (3.30), so that

$$k_1 = \frac{\mu_a}{\lambda} + \frac{\mu_c \left[\log(r_i) - \log(r_o) \right] \left(a_\Theta^4 a_Z^2 - 1 \right)}{a_\Theta^2 \lambda}, \tag{3.37}$$

$$k_2 = \frac{\mu_c \left[a_Z^2 a_\Theta^4 + \log(r_o) - a_Z^2 a_\Theta^4 \log(r_o) \right]}{a_\Theta^2 \lambda}. \tag{3.38}$$

The radial component of the Cauchy stress T_{rr} evaluated at the interface $r = r_i$ can be computed by combining $(3.33) - (3.38)$ as follows

$$T_{rr}(r_i) = -\frac{\mu_c}{\lambda} \frac{(a_\Theta^4 a_Z^2 - 1) [\log(r_i) - \log(r_o)]}{a_\Theta^2}. \tag{3.39}$$

Thus, by using the expression of the Mandel stress tensor (3.33) and (3.34), the evolution equations (3.18) reduce to the following dynamical system:

$$\begin{cases} \dot{a}_\Theta = \dfrac{a_\Theta}{\mu_c \tau_\Theta} \left(B_\Theta + \dfrac{\mu_c(1 - a_\Theta^4 a_Z^2)}{\lambda a_\Theta^2} \right), \\[4mm] \dot{a}_Z = \dfrac{a_Z}{\mu_c \tau_Z} \left(B_Z + \dfrac{\mu_c \left(\lambda^3 - a_\Theta^2 a_Z^4 \right)}{\lambda a_Z^2} \right), \end{cases} \tag{3.40}$$

where the first equation holds whenever $a_\Theta < 1$ or the right-hand side is negative, otherwise $\dot{a}_\Theta = 0$; analogously the latter holds if $a_Z < 1$ or the corresponding right-hand side is negative, otherwise $\dot{a}_Z = 0$.

3.3.1 Stability of the equilibria

Throughout the rest of the Chapter, we will focus on the case where $B_\Theta = B_Z = B < 0$ is spatially constant, so that the external remodelling stresses are homogeneous and share the same value. As we will show in the following, we require B to be negative so that the cortex actively contracts. Moreover, since we are interested in the uniaxial stretch of the axon, we focus on the range $\lambda \geq 1$.

We look for equilibrium solutions of (3.40), setting $\dot{a}_\Theta = \dot{a}_Z = 0$. Subtracting the two equations, we get

$$a_\Theta^2 = \frac{a_Z^2}{\lambda^3}. \tag{3.41}$$

Substitution of (3.41) into the second equation of (3.40) implies that, to find the equilibria, we have to prescribe

$$\varphi(a_Z) = \mu_c a_Z^6 - B\lambda^4 a_Z^2 - \mu_c \lambda^6 = 0. \tag{3.42}$$

Recalling that $B < 0$ and $\lambda \geq 1$, the function φ in (3.42) is strictly increasing and takes values of opposite sign at the endpoints of the interval $[0, 1]$ whenever

$$\frac{B}{\mu_c} < \frac{1 - \lambda^6}{\lambda^4}. \tag{3.43}$$

Hence, if such a condition is satisfied there exists a unique equilibrium solution $(\bar{a}_\Theta, \bar{a}_Z)$. In particular, $\bar{a}_Z$ is obtained from (3.42) and $\bar{a}_\Theta = \bar{a}_Z / \lambda^{3/2}$ is given by (3.41).

To evaluate the stability, we compute the Jacobian matrix of the system (3.40), obtaining

$$\mathbf{J} = \begin{pmatrix} J_{11} & -\dfrac{2a_Z a_\Theta^3}{\lambda \tau_\Theta} \\[4mm] -\dfrac{2a_Z^3 a_\Theta}{\lambda \tau_Z} & J_{22} \end{pmatrix}, \tag{3.44}$$
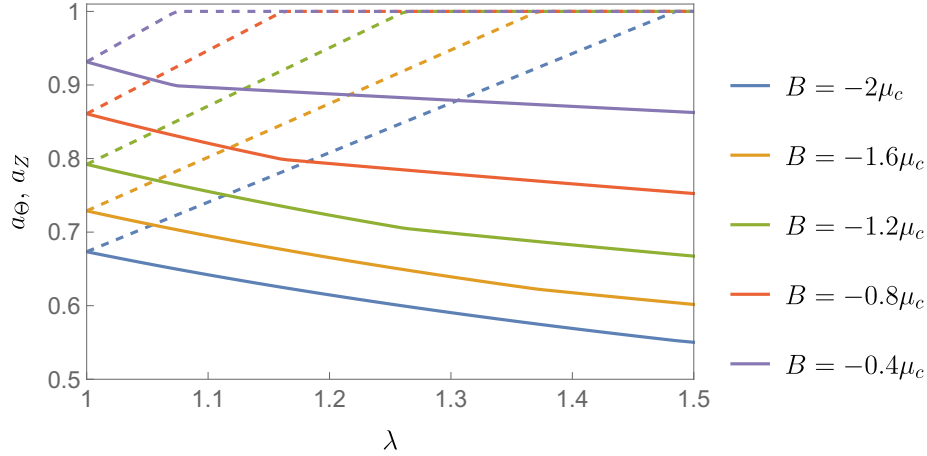
Figure 3.2: Homeostatic active stretches $\bar{a}_\Theta$ (solid lines) and $\bar{a}_Z$ (dashed lines) plotted against the applied stretch λ. The curves are obtained from (3.41), (3.42), and (3.46) by varying $B/\mu_c = -2, -1.6, -1.2, -0.8, -0.4$.

with

$$J_{11} = \frac{a_\Theta^2 \lambda B - \mu_c(1 - 3a_Z^2 a_\Theta^4)}{\lambda \mu_c \tau_\Theta a_\Theta^2},$$

$$J_{22} = \frac{a_Z^2 \lambda B - \mu_c(\lambda^3 - 3a_Z^4 a_\Theta^2)}{\lambda \mu_c \tau_Z a_Z^2}.$$

A direct computation shows that, for all the admissible a_Θ and a_Z, $\mathrm{tr}\mathbf{J} < 0$ and $\det\mathbf{J} > 0$, so that the equilibrium solution $(\bar{a}_\Theta, \bar{a}_Z)$ is asymptotically stable.

On the other hand, if (3.43) does not hold, that is

$$\frac{B}{\mu_c} \geq \frac{1 - \lambda^6}{\lambda^4}, \tag{3.45}$$

we set $\bar{a}_Z = 1$, so that the first equation of (3.18) admits the equilibrium solution

$$\bar{a}_\Theta = \frac{1}{\sqrt{2}} \sqrt{\sqrt{\frac{B^2}{\mu_c^2}\lambda^2 + 4} + \frac{B\lambda}{\mu_c}} \tag{3.46}$$

which always lies in $(0, 1)$. Finally we need to check that $B_Z + \mathbf{M} \cdot \mathbf{I}_Z \geq 0$, so that $\bar{a}_Z = 1$ is a stationary solution of (3.18). It can be easily verified that such a condition is equivalent to (3.45). Moreover, such an equilibrium is always stable since the component J_{11} of the Jacobian matrix (3.44) is negative.

The existence of asymptotically stable equilibria of (3.18) implies that, depending on the initial conditions, the system evolves towards the equilibrium points $\bar{a}_\Theta$ and $\bar{a}_Z$ representing the homeostatic active stretches of the axon.

In Fig. (3.2) we show the stationary solutions $\bar{a}_\Theta$ and $\bar{a}_Z$ against the applied stretch λ, for different values of B. Starting from the same value for $\lambda = 1$, the two active stretches $\bar{a}_\Theta$ and $\bar{a}_Z$ exhibit opposite behaviours as λ increases. On the one hand, $\bar{a}_\Theta$ decreases with λ, leading to a stronger contraction in the circumferential direction generated by the actin molecular motors. On the other hand, a_Z increases until it reaches 1.

(a)

(b)
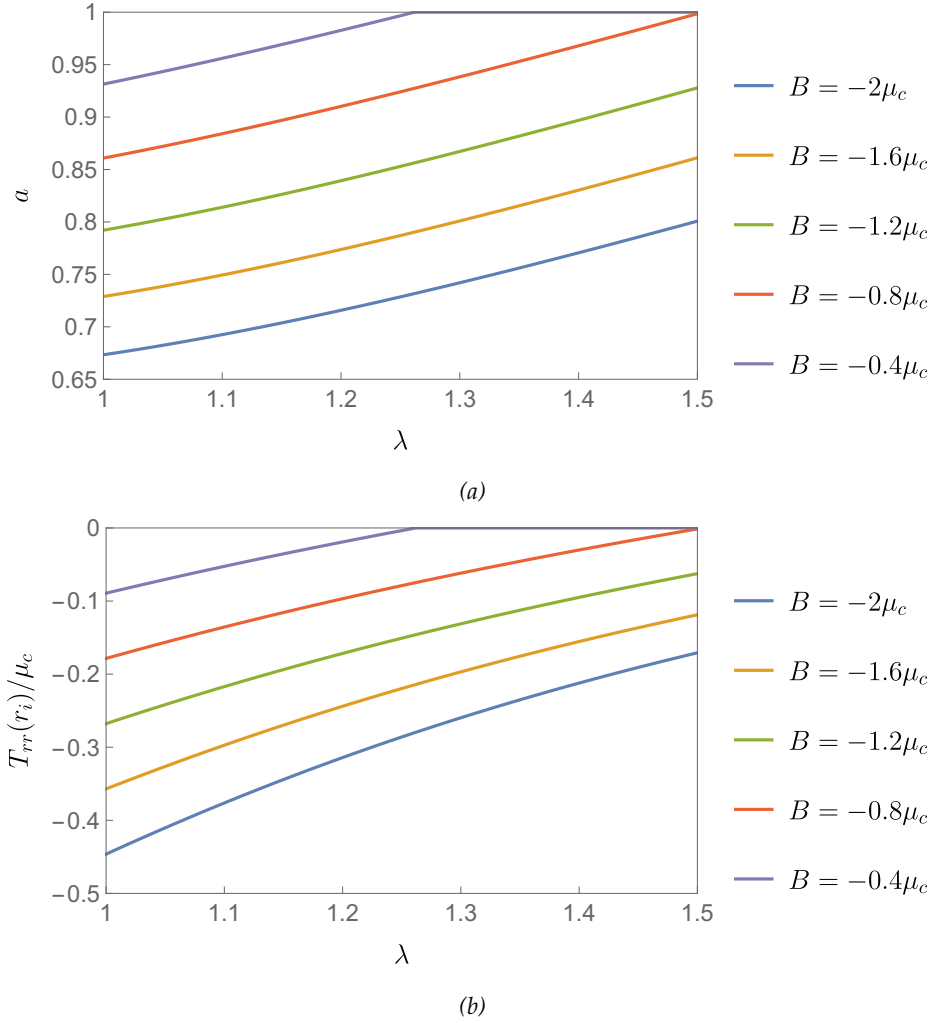
Figure 3.3: Monoparametric approach. (a) Homeostatic active stretch a versus the applied stretch λ. The value of a is computed by using (C.3). (b) Radial stress at the interface calculated from (3.49) for $R_i/R_o = 0.8$. In both cases, the curves are obtained with $B/\mu_c = -2, -1.6, -1.2, -0.8, -0.4$.

We remark that, when $\bar{a}_Z < 1$, exploiting (3.39) the equilibrium radial Cauchy stress at the interface $r = r_i$ can be written as

$$\overline{T}_{rr}(r_i) = B_\Theta \log\left(\frac{R_o}{R_i}\right), \tag{3.47}$$

which is independent of the applied stretch λ. Thus, as the axon is axially stretched the cortex undergoes remodelling to maintain a constant compression of the axoplasm.

3.3.2 Monoparametric active stretch

In [Dehghany et al., 2020], the authors directly prescribe a coupling between a_Θ and a_Z, by assuming a linear relation between the two active stretches. In our case, by enforcing $a_\Theta = a_Z = a$ we

get

$$\mathbf{F_a} = \frac{1}{a^2}\mathbf{e}_R \otimes \mathbf{e}_R + a(\mathbf{I} - \mathbf{e}_R \otimes \mathbf{e}_R). \tag{3.48}$$

The corresponding evolution equation for the active stretch a can be obtained by repeating the procedure exposed in Section 3.2. Similarly to the stability analysis performed in this Section, we find a single asymptotically stable equilibrium, as detailed in C. At the equilibrium, the radial stress at the interface is instead given by

$$\overline{T}_{rr}(r_i) = \frac{\mu_c(\bar{a}^6 - 1)}{\lambda \bar{a}^2} \log\left(\frac{R_o}{R_i}\right). \tag{3.49}$$

As shown in Fig. 3.3a, we observe that a is an increasing function of the axial stretch λ. Eventually, for large enough values of λ, the axon behaves as a passive material when a reaches 1. Differently, our approach predicts an opposite behaviour for the hoop active stretch, as reported in Fig. (3.2). Such differences have important consequences on the stress distribution within the axon. While in our model the compression of the axoplasm is independent of λ, as shown in equation (3.47), in the monoparametric approach the radial stress at the interface relaxes as we increase λ and, eventually, becomes zero, see Fig. 3.3b. This behaviour is the main drawback of such an approach since, as we will show in the next Section, axons actively decrease their radius upon stretching thanks to axoplasm compression.

3.4   Active regulation of axon diameter

In this Section, we investigate the role of cortex contractility in the active regulation of axon diameter, performing a quantitative comparison of the model outcomes with some experimental results. We use data from [Fan et al., 2017], where the authors perform experiments on embryonic drosophila axons, measuring variations of the diameter as a consequence of chemo-mechanical manipulations. In particular, some drugs are exploited to test the mechanical contribution of specific constituents: nocodazole is applied to depolymerise microtubules, while cytochalasin D is used to disrupt F-actin. The effect of these drugs on the axon is depicted in Fig. 3.4. Axons are then rapidly stretched and elongated by 20% of their initial length.

The authors also compare treated axons with some control cases to highlight the effect of each drug on the axonal diameter.

First, we observe that we need to relax the simplifying assumptions of incompressibility made in Section 3.3 to capture the effect of the active contractilty on the axon radius. Thus, we rely on numerical simulations to obtain approximate solutions of the mathematical model. Second, we need to enrich our model to describe the effect of the drugs on the mechanical response of the axon.

3.4.1   Damage

Experimental evidence shows that the axon stiffness diminishes when exposed to nocodazole and cytochalasin D [Ouyang et al., 2013]. We model the structural damage of the axon by introducing a scalar field $\alpha : [t_0, t_1] \times \Omega_0 \to [0, 1]$ describing the percentage of solid material depolymerised by the action of the drug or during the stretch. The free energy for the damaged axon can then be written as

$$\psi(\mathbf{F}, \alpha) = (1 - \alpha)\psi_0(\mathbf{F}\mathbf{F_a}^{-1}), \tag{3.50}$$
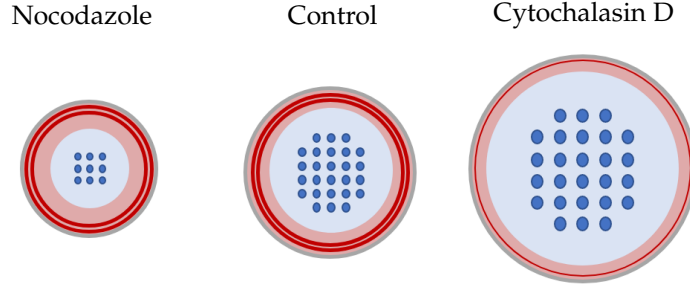
Nocodazole   Control   Cytochalasin D

Figure 3.4: Effect of drugs on the axon structure: red lines represent actin filaments while blue circles indicate micro-tubules. With respect to the control case (center), nocodazole depolymerises microtubules (left) leading to a reduction of the axon diameter, while cytochalasin D reduces the number of the actin filaments (right) and the axon can expand.

where ψ_0 is the strain energy density of the passive, sound axon. Initially, the axon is not damaged and therefore

$$\alpha(t = 0, \mathbf{X}) = 0.$$

When nocodazole is applied, the actin cortex is not affected and only the microtubule network is damaged. Therefore, we propose the following simple phenomenological law for the damage of the axoplasm, describing an exponential degradation:

$$\alpha(t, \mathbf{X}) = \begin{cases} \alpha_n^\infty (1 - e^{-t/\tau_n}), & R < R_i, \\ 0, & R > R_i, \end{cases} \tag{3.51}$$

where α_n^∞ is a constant indicating the percentage of microtubules depolymerised in an infinite amount of time, while τ_n is a characteristic time for the action of nocodazole.

When cytochalasin D is applied, the contractility of the cortex is reduced and actin filaments are depolymerised, thus damaging the elastic response of the cortex [Rotsch and Radmacher, 2000]. Therefore, similarly to nocodazole, we assume that the damage field α reads

$$\alpha(t, \mathbf{X}) = \begin{cases} 0, & R < R_i, \\ \alpha_c^\infty (1 - e^{-t/\tau_c}), & R > R_i, \end{cases} \tag{3.52}$$

where α_c^∞ and τ_c play the same role as α_n^∞ and τ_n in (3.51). On the other hand, we postulate that cytochalasin D also reduces the contractility of the actin cortex by modulating the homeostatic stress in (3.2). Recalling that we are taking $B_\Theta = B_Z = B$, for the sake of simplicity, we also assume that the contraction in the circumferential and axial direction share the same characteristic time, namely $\tau_\Theta = \tau_Z = \tau$ in (3.18). Here we postulate that the reduction of the external remodelling stress due to damage reads

$$B(t, \mathbf{X}) = (1 - \alpha(t, \mathbf{X}))^2 B_0,$$

where B_0 denotes the homeostatic stress in the sound axon.

In the experiments in [Fan et al., 2017], Fan and co-authors observe that, when loads are removed, the final radius is smaller than the initial one. The authors hypothesise that this phenomenon is induced by a damage of the axoplasm. Indeed, a fast axial stretch can induce microtubule depolymerisation [Tang-Schomer et al., 2009]. We model this phenomenon by introducing an instantaneous damage in the axoplasm, increasing $\alpha(t, \mathbf{X})$ by adding a constant α_s for $R < R_i$.

Symbol	Parameter description	Range	Value
R_o	Axon radius	$[1.45\,\mu\mathrm{m},\ 1.90\,\mu\mathrm{m}]$	$1.5\,\mu\mathrm{m}$
$R_o - R_i$	Cortex thickness	$[0.08\,\mu\mathrm{m},\ 0.5\,\mu\mathrm{m}]$	$0.3\,\mu\mathrm{m}$
μ_c	Cortex shear modulus	$[0.1\,\mathrm{kPa},\ 10\,\mathrm{kPa}]$	$1\,\mathrm{kPa}$
μ_a	Axoplasm shear modulus	$[0.1\,\mathrm{kPa},\ 10\,\mathrm{kPa}]$	$1\,\mathrm{kPa}$
Λ_c	Cortex I Lame's coefficient	$[0.21\,\mathrm{kPa},\ +\infty]$	$100\,\mathrm{kPa}$
Λ_a	Axoplasm I Lame's coefficient	$[0,\ 0.29\,\mathrm{kPa}]$	$0.1\,\mathrm{kPa}$
B_0	Homeostatic stress	—	$-1.6\,\mathrm{kPa}$
τ	Active contraction characteristic time	$\sim 10\,\mathrm{min}$	$11.7\,\mathrm{min}$
τ_n	Nocodazole characteristic time	$[8.5\,\mathrm{min},\ 83.4\,\mathrm{min}]$	$20\,\mathrm{min}$
τ_c	Cytochalasin D characteristic time	$\sim 10\,\mathrm{min}$	$10\,\mathrm{min}$
α_n^∞	Nocodazole damage	—	0.65
α_c^∞	Cytochalasin D damage	—	0.9
α_s	Stretch induced damage	—	$0.1/0.75$

Table 3.1: Values of parameters involved in the model. Except for those calibrated in the present study (B_0, α_n^∞, α_c^∞ and α_s), all the parameters were chosen within a suitable range of values given by experimental measurements [Dennerll et al., 1989, Rotsch and Radmacher, 2000, Bernal et al., 2007, Liewald et al., 2014, Fan et al., 2017, García-Grajales et al., 2017, Zhang et al., 2017, Datar et al., 2019, Dehghany et al., 2020]. The stretch induced damage has been set equal to 0.75 in the control case and when cytochalasin D is applied. In the case of nocodazole treated axons, the parameter is decreased to 0.1 since the axoplasm is already damaged. With the exception of [García-Grajales et al., 2017], the cortex is frequently treated as an almost incompressible medium, thus we have chosen a high value for Λ_c.

3.4.2   Constitutive assumptions

For the sake of simplicity, we disregard any anisotropy induced by the orientation of microtubules or actin filaments, assuming that both the axoplasm and the cortex are composed of a compressible neo-Hookean material, that is

$$\psi_0(\mathbf{F}_\mathrm{e}) = \frac{\mu}{2}\left(\mathbf{F}_\mathrm{e} \cdot \mathbf{F}_\mathrm{e} - 2\log J_\mathrm{e} - 3\right) + \frac{\Lambda}{2}(\log J_\mathrm{e})^2, \tag{3.53}$$

where μ and Λ are the Lamé coefficients of the sound axon. The axoplasm and the cortex are homogeneous, so that the Lamé coefficients are piecewise constant within the domain

$$\mu = \begin{cases} \mu_\mathrm{a}, & R < R_\mathrm{i}, \\ \mu_\mathrm{c}, & R > R_\mathrm{i}, \end{cases} \qquad \Lambda_0 = \begin{cases} \Lambda_\mathrm{a}, & R < R_\mathrm{i}, \\ \Lambda_\mathrm{c}, & R > R_\mathrm{i}. \end{cases}$$

In the next Section, we propose a numerical scheme to discretise the model.

3.4.3   Initial conditions

In the experiments reported in [Fan et al., 2017], the axons are in their equilibrium state at the initial instant of time. Thus, we set $\lambda = 1$ and

$$\begin{cases} \alpha|_{t=0} = 0, \\ u|_{t=0} = u_0, \\ a_\Theta|_{t=0} = a_{\Theta 0}, \\ a_Z|_{t=0} = a_{Z0}, \end{cases}$$
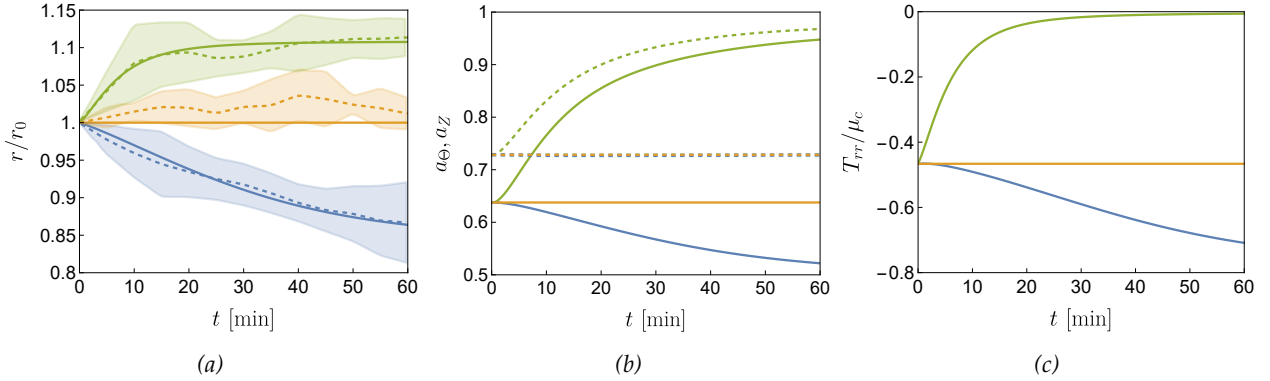
Figure 3.5: Unstretched axons ($\lambda = 1$). Plots are reported for each treatment scenario: control (orange), nocodazole (blue) and cytochalasin (green). (a) Comparison between the numerical result (continuous lines) and the experimental data reported in [Fan et al., 2017] (dashed lines) for the evolution of external radius. The latter is normalised with respect to r_0, the radius of the axon at equilibrium. The shaded regions indicate error bar in standard deviation relatively to the experimental data. (b) Plots of a_Θ (continuous lines) and a_Z (dashed lines) averaged over the cortex sectional area. (c) Evolution of radial stress T_{rr} at the interface $r = r_i$, normalised with respect to the undamaged shear modulus of the cortex.

as initial conditions, where u_0, $a_{\Theta 0}$, and a_{Z0} are the stationary solutions of (3.18) and (3.27). Such equilibrium state has to be determined by means of numerical computations.

3.4.4 Numerical implementation

Here we detail the numerical implementation of the problem under the cylindrical symmetry assumptions discussed in Section 3.2.5. We subdivide the interval $[0, R_o]$, representing the spatial computational domain, into 500 elements. The time step of the simulations is $\Delta t = 0.3$ minutes. Exploiting the finite element method, we approximate the radial displacement field u with continuous piece-wise linear functions while the active stretches a_Θ and a_Z are discretised by means of piece-wise constant functions. At each time step we solve the balance of the linear momentum (3.27) enforcing the boundary condition (3.29). Time integration of the evolution equations (3.18) is performed by using an explicit Euler scheme. The numerical algorithm is implemented using the Python library FEniCS [Alnæs et al., 2015], exploiting PETSc as linear algebra back-end.

3.4.5 Results of the simulations

In the following, we present and discuss the outcomes of the numerical simulations. First, we analyse the effect of drugs in unstretched axons (i.e. $\lambda = 1$). Then, in accordance with the experimental procedure proposed in [Fan et al., 2017], we impose an elongation of the axon up to 20% of its initial length (i.e. $\lambda = 1.2$) and analyse its effect following a one-hour-long exposure to drugs.

The parameters used in the numerical model are fixed by either exploiting measures coming from the existing literature or through a fitting of the experimental data. We refer to Table 3.1 for details on the choice of the model parameters.
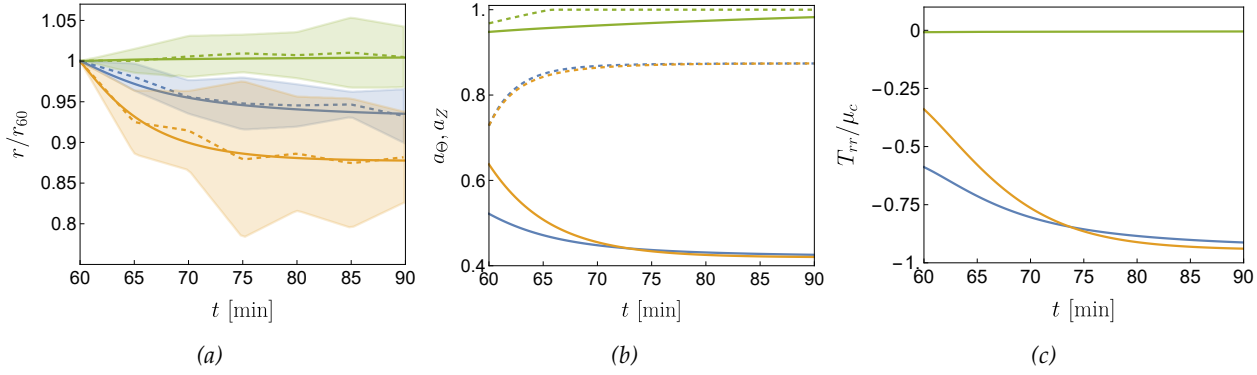
Figure 3.6: Uniaxial stretch ($\lambda = 1.2$). Plots are reported for each treatment scenario: control (orange), nocodazole (blue) and cytochalasin (green). (a) Comparison between the numerical result (continuous lines) and the experimental data reported in [Fan et al., 2017] (dashed lines) for the evolution of external radius. The latter is normalised with respect to r_{60}, the radius of the axon at $t = 60$ minutes, immediately after stretch. The shaded regions indicate error bar in standard deviation relatively to the experimental data. (b) Plots of a_Θ (continuous lines) and a_Z (dashed lines) averaged over the cortex sectional area. (c) Evolution of radial stress T_{rr} at the interface $r = r_i$, normalised with respect to the shear modulus of the sound cortex.

3.4.5.1 Effect of drugs on unstretched axons

First, we remark that untreated axons maintain the initial equilibrium state since they are not damaged.

In all the cases, the active contraction of the cortex induces a compressive stress on the axoplasm. The depolymerisation of microtubules due to nocodazole leads to a reduction of the radius and modifies the cortical stress state. Interestingly, the cortex restores the target homeostatic stress by progressively decreasing a_Θ as shown in Fig. $3.5b$, while the axial active stretch a_Z does not undergo significant variations. The increase in the circumferential contraction results into a greater compression exerted by the cortex on the axoplasm (i.e. T_{rr} at the interface is negative and decreases, as shown in Fig. $3.5c$). In summary, the reduction of the axonal radius following nocodazole exposure is due to the coupling between microtubule depolymerisation and the circumferential active contraction. The longitudinal active stretch instead features an imperceptible deviation from the equilibrium configuration.

Finally, cytochalasin D is responsible for a disruption of actin filaments in the cortex and the reduction of cortical homeostatic stress. As a consequence, both the active stretches a_Θ and a_Z undergo a substantial increment which makes them close to 1 after one hour. In this case, the axoplasm behaves as a nearly passive material and the stress is almost completely relaxed (see Fig. $3.5c$).

3.4.5.2 Uniaxial stretch

Let us first consider the control case, i.e. the stretching of a sound axon without any applied pharmacological treatment. The radius significantly reduces in time, as shown in Fig. $3.6a$. This is the result of cortex remodelling: while a_Z increases to balance the tension due to the axial stretch, a_Θ diminishes, i.e. the active hoop contraction increases (see Fig. $3.6b$). Such a microstructural reorganisation increases axoplasm compression, as shown in Fig. $3.6c$. The changes in the axon diameter are amplified by the axoplasm damage induced by the fast stretch.
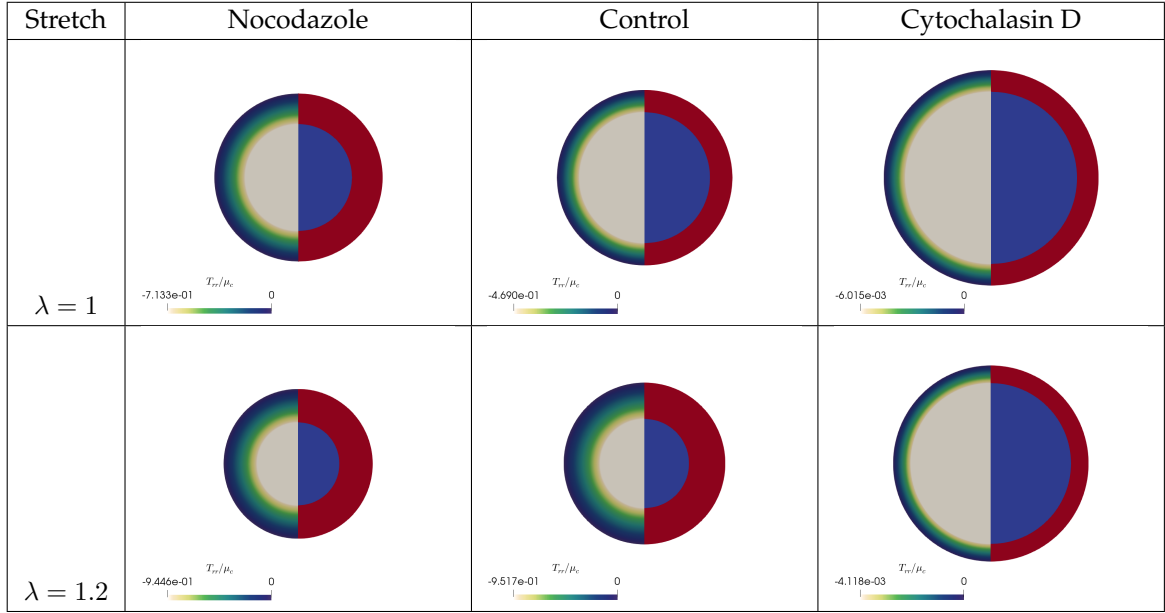
Stretch	Nocodazole	Control	Cytochalasin D
$\lambda = 1$	T_{rr}/μ_c -7.133e-01 0	T_{rr}/μ_c -4.690e-01 0	T_{rr}/μ_c -6.015e-03 0
$\lambda = 1.2$	T_{rr}/μ_c -9.446e-01 0	T_{rr}/μ_c -9.517e-01 0	T_{rr}/μ_c -4.118e-03 0

Figure 3.7: Actual transverse section of the axon for $\lambda = 1$ (top) and $\lambda = 1.2$ (bottom) at $t = 60\,\mathrm{min}$ and $t = 90\,\mathrm{min}$, respectively. In each transverse section, on the left we plot the dimensionless radial stress profile T_{rr}/μ_c, while on the right half we highlight the actual configurations of the axoplasm and of the cortex, represented as the blue and the red areas, respectively.

The dynamics of axons undergoing uniaxial deformation after being exposed to nocodazole is similar, even though the induced thinning is less pronounced compared with the control case. We remark that axons treated with nocodazole are already damaged when stretch is performed, therefore less microtubules are depolymerised as a result of the deformation, and the initial state is closer to the final equilibrium state, as depicted in Fig. 3.6*b*. Instead, the evolution of a_Z is almost the same in both the cases. Qualitatively similar trends are also observed in Fig. 3.6*c* where we plot the radial stress T_{rr} at the interface as a function of time: radius reduction is correlated with an increased compression of the axoplasm.

Finally, let us consider the stretching of axons exposed to cytochalasin D. In Fig. 3.6*a* we see that the radius is almost constant in time after the deformation. Indeed, as shown in Fig. 3.6*b*, both the active stretches are close or equal to 1, so that the cortex behaves as an almost passive material. The constant diameter as the result of F-actin depolymerisation supports our conjecture: the modification of the radius when the axon is stretched is induced by the active reorganisation of the cortex that aims at maintaining a homeostatic stress state.

To better visualise how the stress profile influences axonal morphing, in Fig. 3.7 we show the actual transverse section at the final instant of time. Here, we plot the nondimensionalised radial stress T_{rr}/μ_c. We observe that thinning of axons appears to be correlated with cortex thickening.

3.4.6 Discussion and concluding remarks

In this work, we have constructed a mathematical model based on Continuum Mechanics to analyse the active contraction of axonal cortex when subject to chemo-mechanical stimuli.

Modelling the axon as a continuum hyperelastic body, we have exploited the active strain ap-

proach to describe cortex contractility. A thermodynamically consistent constitutive model has been obtained by means of the Coleman-Noll procedure. The resulting system of differential equations regulating the time evolution of the hoop and axial components of the active stretch is the one in (3.18). Such equations exhibit some peculiarities if compared with models of stress modulated growth in biological tissues [DiCarlo and Quiligotti, 2002, Ambrosi and Guana, 2005]. Indeed, the system evolves so that particular linear combinations of the Mandel stress tensor components remain constant. Thus, the axon reacts to external chemo-mechanical stimuli regulating the active contraction to target a homeostatic stress state.

The qualitative behaviour of the axon is then assessed with analytical calculations under the simplifying assumption of material incompressibility. In this context, the evolution equations reduce to the nonlinear dynamical system (3.40). Through a linear stability analysis, we have shown the existence of a single asymptotically stable solution, representing the above mentioned homeostatic state towards which the system evolves.

Then, using a more suitable compressible constitutive model, we have proposed a numerical discretisation of the problem by means of the finite element method. We have investigated mechanical conditions corresponding to the experiments reported in [Fan et al., 2017], analyzing the behaviour of the unstretched axon and its response to a subsequent uniaxial strain of the 20%. Three pharmacological conditions are reproduced: a) control case, b) the disruption of F-actin filaments when exposed to cytochalasin D and c) the depolymerisation of microtubules following the application of nocodazole. In the model, the effect of the drugs is accounted for by introducing a damage function that modifies the energy functional, as discussed in Section (3.4.1). Moreover, since in the *in vitro* experiments the axons are pulled at a high strain rate [Fan et al., 2017], we assume that microtubules are further damaged during the axial deformation [Tang-Schomer et al., 2009].

The numerical outcomes for each scenario described above are in excellent quantitative agreement with the experimental results, as shown in Figs. (3.5)-(3.6). Indeed, the diameter progressively increases when F-actin filaments are disrupted, while a decrease of the transverse section area with respect to the control case is observed when microtubules are depolymerised. We have shown that the diameter of axons is regulated by the compressive stress exerted on the axoplasm by the cortex. Diameter reduction appears to be correlated with the thickening of the axonal cortex, as reported in Fig. (3.7).

Our results support the hypothesis of a coupling between the axial and hoop active stretches [Fan et al., 2017]. The cortex undergoes a microstructural reorganisation to modulate its stress state and regulates axon diameter by compressing the axoplasm. The understanding of such a mechanism may represent a preliminary step towards the comprehension of the physical causes underlying axon morphological degeneration as a consequence of neurodegenerative diseases, viral infections, and traumatic strain injuries.

Future efforts will be devoted to the analysis of such a system when subject to displacements breaking the axial symmetry. Furthermore, it would interesting to study the effect of morphological changes of the axon on its ability to transmit electro-chemical signals.

Chapter 4

A gradient flow approach to leaves morphogenesis

4.1 Introduction

Unveiling the mechanisms behind growth processes in biological structures is crucial for the understanding of organ morphogenesis and plasticity. In this Chapter we focus on the growth of leaves, which are often considered as a prototypical example of active tissues.

The accurate description of leaves growth must take into account many physical phenomena ranging from the chemical processes happening at a cellular level to the mechanical phenomena occurring at microscopic and macroscopic scales. Many works focused on reproducing the experimentally observed growth patterns through mathematical models describing how genes and hormones control cellular proliferation and expansion [Kuchen et al., 2012, Kierzkowski et al., 2019, Bhatia et al., 2021]. Here we study leaves growth from a different perspective and try to justify it in terms of the purpose it serves, rather than in terms of its causes. In other words, we give a *teleological* description of growth. In particular we embrace the common assumption by which leaves maximize the benefit coming from light absorption. Indeed, leaves are fundamental for plants, since they exploit light for the photosynthesis of the nutrients necessary for sustaining life. Hence it is usually assumed that, due to their importance, leaves have been subject to intense evolutionary pressures leading them to develop highly efficient strategies for carrying out their tasks.

An example of highly optimized structure that can be found in leaves (but also in most of the living systems) is the venation pattern for the transport of water and nutrients. Indeed, it is well known that ramified networks can emerge as the solution of an Optimal Transport Problem [Xia, 2003, Oudet and Santambrogio, 2011, Facca, 2016, Tosi, 2018, Facca et al., 2021]. Hence it is believed that biological networks like those constituting the circulatory system or leaves venation have been singled out by Natural Selection as a means to efficiently transport nutrients in living organisms. Many studies focused on these aspects either through a discrete or a continuous approach [Xia, 2007, Hu and Cai, 2013, Xia, 2015, Facca et al., 2018, Lu and Hu, 2022]. The great morphological diversity of leaves is another instance of natural adaptation driven by evolutionary pressures. Among the factors influencing the shape of leaves we mention structural compliance, thermal dissipation, water availability, amount of light exposure of the blade and venation pattern [Kidner and Umbreen, 2010, Shimoda and Nakata, 2012, Wright et al., 2017, Ding et al., 2020, Ronellenfitsch,

2021].

In the present work, we derive a model for the growth of veins and of the leaf's blade. Such a problem was first addressed in [Xia, 2007] using a discrete teleological model, by which new leaf's cells are generated only if the revenue they produce through light absorption is greater than the transport cost needed to reach them with nutrients. We embrace this principle and embed it into a continuum framework as a way to overcome some of the inherent limitations of the model presented in [Xia, 2007], which does not describe the bulk growth pattern leading to the final shape of the leaf. In fact, as reported in [Das Gupta and Nath, 2015], leafs often show an *allometric growth*, namely, the growth rate is non-homogeneous throughout the leaf blade and exhibits spatial polarity. Hence, in order to deal with allometric growth, we develop a continuum model describing the evolution of the leaf blade using a growth map. Moreover, inspired by [Lu and Hu, 2022], we model the formation of veins through a phase-field approach based on the introduction of a conductance field. In [Lu and Hu, 2022] the authors advance a criterion for describing growth and plasticity in vein formation. In particular, they assume that the phase-field for the venation pattern arises from the minimization of a suitable transport cost. Moreover, they postulate that the growth process is governed by the L^2-gradient flow of such a cost functional. Inspired by [Xia, 2007] and [Lu and Hu, 2022], we develop a model in which the growth map and the conductance field evolve according to a gradient flow aiming at maximizing the net power absorbed by the leaf. This quantity is given by the difference between the light energy absorbed by the leaf blade and the energy cost for the transport of nutrients.

In Section 4.2 we carry out the derivation of the model detailing the kinematics, the mass balance and the gradient flow equations ruling the growth of the leaf. In Section 4.3 we discuss the numerical implementation of the equations and the outcome of preliminary simulations. Finally, in Section 4.4 we summarize our findings and discuss future development and possible improvements of the model.

4.2   Formulation of the model

4.2.1   Notation and kinematics

We model the leaf as a two dimensional body immersed in the two-dimensional Euclidean space. We denote by $\mathcal{B} \subset \mathbb{R}^2$ the reference configuration of the leaf blade (see Fig. 4.1) and by Γ its boundary. The latter is subdivided in to two complementary parts, Γ_{p}, representing the petiole and Γ_{m} representing the leaf's margin. The leaf growth is described by a motion $f : \mathcal{B} \to \mathbb{R}^2$ mapping material points $X \in \mathcal{B}$ into the corresponding places x in $\mathbb{R}^2$, namely $x = f(X, t)$. The current configuration of the leaf at time t is denoted by $\mathcal{B}_t = f(\mathcal{B}, t)$. We then indicate with the symbol ∇ the material gradient and with $\mathrm{grad}(\cdot)$ the spatial one. Finally, by adopting a standard notation for related kinematic quantities, we write: $\mathbf{F} = \nabla f$, $\mathbf{C} = \mathbf{F}^{\mathsf{T}}\mathbf{F}$ and $J = \det \mathbf{F}$.

We stress that, in the present model, f accounts for a growth process and is by no means associated to an *elastic* energy density. Traditionally, growth is described through a multiplicative decomposition of the deformation gradient into an elastic part and a growth one, the latter not necessarily coinciding with the gradient of a map. In this framework, our choice of describing growth with a map f is equivalent to assume that the growth tensor evolves preserving its compatibility, and hence that no residual stresses are present. This simplifying assumption is motivated by the fact that leaves, despite being thin two-dimensional structures, grow preserving a flat configura-
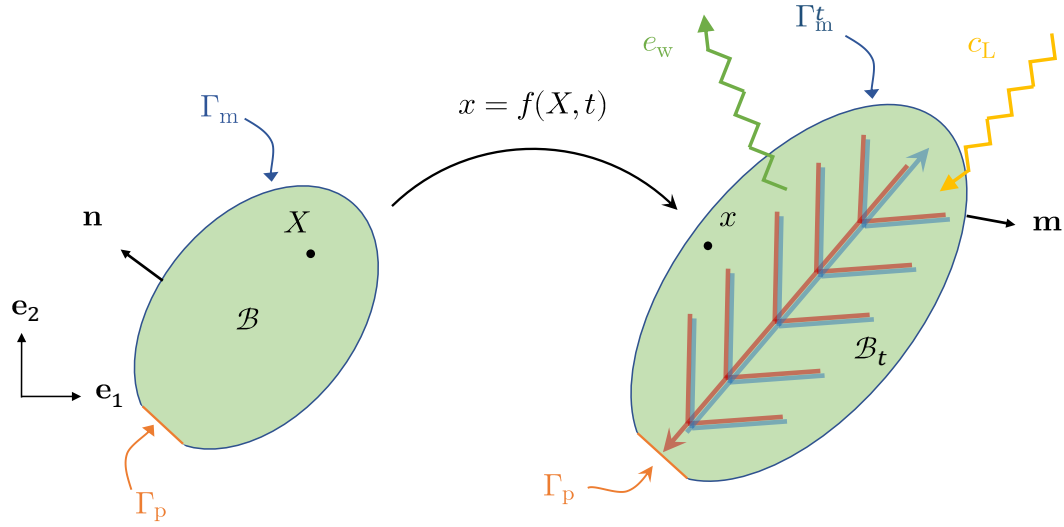
Figure 4.1: Pictorial illustration of a leaf and its kinematics. Water absorbed by the roots enters the petiole and is distributed, through a network of veins known as xilems (in blue), to every place of the leaf's blade. Most of the water evaporates (green arrow), while the remaining part takes part to photosynthetic processes necessitating of light absorption (yellow arrow). Finally, the photosynthesized nutrients are sent back to the plant, as sap, through veins called phloems (in red). Here, $\mathcal{B}$ is the reference configuration of the leaf, which undergoes a growth process encoded by $f : \mathcal{B} \to \mathbb{R}^2$, $X \mapsto f(X) = x$. We also highlight its boundary Γ with outer unit normal $\mathbf{n}$, decomposed into Γ_p, representing the petiole and Γ_m, representing the leaf margin. Finally we denote with $\mathcal{B}_t$ the actual configuration and with Γ_t its boundary with outer unit normal $\mathbf{m}$. Again, the actual boundary is decomposed into complementary parts Γ_p and Γ_m^t (notice that, since we do not model the growth of the petiole, we have $f(\Gamma_p, t) = \Gamma_p$).

tion allowing them to optimize the exposure to light[1]. Indeed, it is well known from the theory of thin plates ([Efrati et al., 2009, Sharon and Efrati, 2010, Efrati et al., 2013]) that non-compatible growth processes are often responsible for the insurgence of highly curved configurations. Hence, we found it an acceptable approximation to assume that leafs tend to growth in an almost compatible way, thanks to some unidentified internal regulation mechanism. The nature of this regulation mechanism is still object of debate ([Shahaf et al., 2021, al Mosleh and Mahadevan, 2022]). This argument also motivates our choice to model the leaf as a body immersed in the two-dimensional Euclidean space.

4.2.2 Mass balance

Leafs are complex systems interacting with the environment through the exchange of mass and energy in order to grow and sustain their metabolic activity (see Fig. 4.1). Light energy is converted into utilizable chemical energy through photosynthesis, a process necessitating of the supply of water and carbon dioxide. Water enters leaves trough the petiole and reaches the cells through a ramified system of veins known as xilems [Sack and Scoffoni, 2013]. Interestingly, almost 95% of

---

[1]In fact, it is believed that the optimal configuration for the leaf is the result of a trade-off between flatness and structural compliance of the blade, as discussed in [Shimoda and Nakata, 2012]. Nevertheless, as a first approximation, leafs are supposed to be essentially flat bodies.

water evaporates in the atmosphere thanks to the opening of stomata, which are pores found in the epidermis of leaves controlling the rate of gas exchange. Water evaporation is fundamental for regulating the temperature of the leaf and it also acts as a driving force drawing water adsorbed by the roots. Stomata also allow leaves to absorb the carbon dioxide dispersed in the atmosphere. The outcome of photosynthesis is oxygen (expelled through stomata) and glucose, which the plant exploits for sustaining its metabolism and for carbon fixation. Finally, sap (a mixture of water and glucose) is distributed to the rest of the plant through a network of veins, parallel to xilems, called phloems.

We consider the leaf as a homogenized porous medium constituted by a solid substratum permeated by two liquid phases: water and sap. For every $\mathcal{P}_t$ regular subset of $\mathcal{B}_t$, we denote by $M(\mathcal{P}_t)$ the mass of a part of the leaf. Then, the mass balance reads

$$\frac{\mathrm{d}}{\mathrm{d}t} M(\mathcal{P}_t) = -\int_{\partial \mathcal{P}_t} \mathbf{h}_{\mathrm{xi}} \cdot \mathbf{m} - \int_{\partial \mathcal{P}_t} \mathbf{h}_{\mathrm{ph}} \cdot \mathbf{m} + \int_{\mathcal{P}_t} (e_{\mathrm{CO}_2} - e_{\mathrm{O}_2} - e_{\mathrm{w}}) \qquad \forall \mathcal{P}_t \subset \mathcal{B}_t, \qquad (4.1)$$

where $\mathbf{h}_{\mathrm{xi}}$ is the water mass flux carried by the xilems, $\mathbf{h}_{\mathrm{ph}}$ is the sap mass flux carried by the phloems, $e_{\mathrm{CO}_2} > 0$ is the mass density rate for carbon dioxide absorption, whereas $e_{\mathrm{w}} > 0$ and $e_{\mathrm{O}_2} > 0$ are the mass density rates for carbon dioxide absorption and water and oxygen evaporation, respectively. As already mentioned, most of the water evaporates through the leaf blade so that only a small percentage (between 3%-5%) is employed by the leaf for photosynthesis. Hence, the stoichiometry of photosynthesis reactions allows us to assume that also the rates of carbon dioxide absorption and oxygen release are small if compared to the total water uptake from the roots. This also implies that the rate of glucose production, responsible for biomass accumulation (*i.e.* time variations of $M(\mathcal{P}_t)$), is small compared to water fluxes. Accordingly, we simplify equation (4.1) by neglecting the contribution of CO_2, O_2 and mass change of the part $\mathcal{P}_t$. Hence, equation (4.1) simplifies into

$$\int_{\partial \mathcal{P}_t} \mathbf{h}_{\mathrm{xi}} \cdot \mathbf{m} + \int_{\mathcal{P}_t} e_{\mathrm{w}} = 0 \qquad \forall \mathcal{P}_t \subset \mathcal{B}_t. \qquad (4.2)$$

Fluid transport in veins   To model transport mediated by veins, we adopt the approach proposed in [Lu and Hu, 2022]. First, we assume a Darcy's law according to which $\mathbf{h}_{\mathrm{xi}} = -\mathbf{A}_{\mathrm{s}}\mathrm{grad}(p)$, where $\mathbf{A}_{\mathrm{s}}$ is the *spatial* conductance tensor field (symmetric and positive definite) and p is the water pressure. Then, we additively decompose $\mathbf{A}_{\mathrm{s}}$ as follows

$$\mathbf{A}_{\mathrm{s}} = r\mathbf{I} + \mathbf{M}_{\mathrm{s}}.$$

The first term, $r\mathbf{I}$, describes the background diffusion of the tissue of the leaf and accounts for fluid diffusion across cells membranes. The second one, $\mathbf{M}_{\mathrm{s}}$, typically much larger than the former, accounts for fluid flow mediated by xilems. Hence, $\mathbf{M}_{\mathrm{s}}$ can be though as a phase-field for the description of veins and consequently is supposed to distribute in space according to a ramified structure.

To simplify the analysis we assume $\mathbf{M}_{\mathrm{s}}$ to be isotropic, namely, $\mathbf{M}_{\mathrm{s}} = m_{\mathrm{s}}^2\mathbf{I}$, so that the total conductance can be written as $\mathbf{A}_{\mathrm{s}} = a_{\mathrm{s}}\mathbf{I}$, with $a_{\mathrm{s}} = r + m_{\mathrm{s}}^2$. Then, exploiting the Darcy's law, the mass balance equation (4.2) becomes

$$\int_{\partial \mathcal{P}_t} a_{\mathrm{s}}\mathrm{grad}(p) \cdot \mathbf{m} - \int_{\mathcal{P}_t} e_{\mathrm{w}} = 0 \qquad \forall \mathcal{P}_t \subset \mathcal{B}_t. \qquad (4.3)$$

Furthermore, the leaf's margin is assumed impermeable and is thus endowed with zero flux boundary conditions, while we impose homogeneous Dirichlet conditions for the pressure at the petiole:

$$a_\text{s}\text{grad}(p) \cdot \mathbf{m} = 0 \text{ on } \Gamma_\text{m}^t \qquad p = 0 \text{ on } \Gamma_\text{p}. \tag{4.4}$$

Pull-back on $\mathcal{B}$ As already anticipated in the introduction, we are interested in modelling the growth of the leaf's blade and venation by deriving a set of evolution equations for f and m_s. The evolution of m_s accounts for the transition between different cell types, namely from "vein type" to "blade type" and vice-versa. Such a process can be assimilated to *cellular differentiation*. On the other hand, f accounts for growth due to *cell proliferation* and *expansion*. It is then clear that vein formation is influenced by both differentiation and growth. Therefore, a little care must be taken when pulling back Eq. (4.3) in the reference domain, since one must establish how the evolution of f affects the vein pattern encoded by m_s. In other words, we must prescribe how m_s is advected by f. It appears that the process of cell division generates new cells of the same type of the mother cell [Laguna et al., 2008]. Even more so, cell expansion does not alter the differentiated state of cells. Hence, it is reasonable to describe the growth of "vein-type" tissue trough the advection of a *material* field $m(X, t)$ introduced for labeling and tracking material points, namely,

$$m_\text{s}(x, t) = (m \circ f^{-1})(x, t). \tag{4.5}$$

In such a way, material elements grow preserving their value of m, hence preserving their tissue-type attributes.

So, thanks to (4.5) and recalling that $\text{grad}(p)_\mathbf{m} = \mathbf{F}^{-\mathsf{T}}\nabla p$, the balance in Eq. (4.3) in the referential form becomes

$$\int_{\partial\mathcal{P}} Ja\mathbf{C}^{-1}\nabla p \cdot \mathbf{n} - \int_{\mathcal{P}} Je_\text{w} = 0 \qquad \forall\mathcal{P} \subset \mathcal{B},$$

where $a = r + m^2$. Upon localization, the above equation leads to

$$\text{Div}\,(Ja\mathbf{C}^{-1}\nabla p) - Je_\text{w} = 0 \text{ on } \mathcal{B}\,. \tag{4.6}$$

As regards the boundary conditions in Eq. (4.4), they become

$$\begin{cases} Ja\mathbf{C}^{-1}\nabla p \cdot \mathbf{n} = 0 & \text{on } \Gamma_\text{m}, \\ p = 0 & \text{on } \Gamma_\text{p}. \end{cases} \tag{4.7}$$

For later use, we also report the weak formulation of (4.6)-(4.7), which reads

$$\int_\mathcal{B} Ja\mathbf{F}^{-\mathsf{T}}\nabla p \cdot \mathbf{F}^{-\mathsf{T}}\nabla\phi + \int_\mathcal{B} Je_\text{w}\phi = 0 \quad \forall\phi \in V_p = \{\phi \text{ s.t } \phi = 0 \text{ on } \Gamma_\text{p}\}. \tag{4.8}$$

4.2.3 The gain functional

As anticipated in the introduction, we adopt a *teleological* approach. In particular, inspired by [Xia, 2007], we postulate a growth process which aims at maximizing the net power gained by the leaf. Such a gain, $\mathscr{G}$, is given by the difference between $\mathscr{L}$, the rate of light energy absorbed through the blade, and $\mathscr{C}$, the cost for transporting water from the petiole to every place of the leaf. Hence we have

$$\mathscr{G} = \mathscr{L} - \mathscr{C}. \tag{4.9}$$

We simply model light absorption as

$$\mathscr{L} = \int_{\mathcal{B}_t} c_L, \tag{4.10}$$

where $c_L(x)$ is a scalar field accounting for the amount of light exposure to which the point x is subjected.

As regards the cost for mass transport, we recall that the water flow in leaves is mediated by an intricate network of veins. Larger veins offer a smaller hydrodynamic resistance to fluid flow but, at the same time, they are responsible for a higher metabolism cost and for additional weight to be supported by the leaf [Murray, 1926]. Hence, the dimension of veins is the result of a trade-off that typically leads to the formation of hierarchical structures where few main large veins branch out into smaller secondary veins, and so on in a fractal fashion. In the present work, following [Lu and Hu, 2022] we represent the power expended by the leaf for transporting fluid as

$$\mathscr{C} = \int_{\mathcal{B}_t} \left(c^2 a |\mathrm{grad}(p)|^2 + \alpha^2 |m_{\mathrm{s}}|^{2\gamma} + \varepsilon |\mathrm{grad}(m_{\mathrm{s}})|^2 \right), \tag{4.11}$$

where $\gamma < 1$. Regarding the first and second term, they account for the hydrodynamic dissipation and for the metabolic cost, respectively. They are scaled by factors (c^2 and α^2, respectively) weighting their they relative importance. Finally, the third term is added to regularize the model. Observe that the hydrodynamic dissipation in Eq. (4.11) is only relative to fluid flow in xilems, since all the other contribution are negligible, as detailed in Subsection 4.2.2.

So, according to Eqs. (4.10), (4.11) and (4.9), the net gain reads

$$\mathscr{G} = \int_{\mathcal{B}_t} \left[c_L - \left(c^2 a_{\mathrm{s}} |\mathrm{grad}(p)|^2 + \alpha^2 |m_{\mathrm{s}}|^{2\gamma} + \varepsilon |\mathrm{grad}(m_{\mathrm{s}})|^2 \right) \right],$$

which can be pulled-back in the reference configuration as

$$\mathscr{G}(f, m) = \int_{\mathcal{B}} J \left[c_L - \left(c^2 a |\mathbf{F}^{-\mathsf{T}} \nabla p|^2 + \alpha^2 |m|^{2\gamma} + \varepsilon |\mathbf{F}^{-\mathsf{T}} \nabla m|^2 \right) \right]. \tag{4.12}$$

We remark that in Eq. (4.12) the dependence of $\mathscr{G}$ on p is ruled out thanks to the mass balance equation in Eq. (4.8). Also, p will be treated as a function of f and m throughout the rest of the present Chapter.

4.2.4   A gradient flow description of leaves growth

On large scales, advection is energetically favorable with respect to diffusion, thus explaining why natural selection has led plants to develop an efficient venation structure. Inspired by this fact, the authors in [Lu and Hu, 2022] adopt the field m arising from the minimization of the cost in Eq. (4.11) as the descriptor of veins. As shown in [Lu and Hu, 2022], the minimization of $\mathscr{C}$ leads to the emergence of ramified structures, identified by regions where m is greater than a certain threshold. The observed symmetry-breaking patterns of m are *bifurcation* points arising from the lack of *convexity* of $\mathcal{C}$ ([Haskovec et al., 2015, Albi et al., 2016, Albi et al., 2017]). Besides the characterization of the network structure, the authors also propose a mechanism for its growth

by postulating an evolution for m based on a formal L^2-gradient flow of $\mathscr{C}$. We extend such a theory by modelling the growth of both the venation pattern and the leaf blade. We then postulate that both the fields f and m evolve following a gradient flow aiming at maximizing the net gain $\mathscr{G}$, subject to the constraint of the mass balance (4.8).

The variational problem As shown in Appendix D.1, the gradient flow can be formally characterized through a variational principle for the rates of f and m. In particular, let $f \in V_f = \{f \text{ smooth on } \mathcal{B} \text{ s.t. } f = \text{Id on } \Gamma_p\}$, $m \in V_m = \{m \text{ smooth on } \mathcal{B}\}$, and let $\mathcal{M} = V_f \times V_m$ denote the product "manifold" on which the pair (f, m) is defined. Moreover, let us consider a scalar product $(\cdot, \cdot)$ for the elements of the "tangent space" $T_{(f,m)}\mathcal{M} = \{(\mathbf{v}, \nu) \text{ s.t } \mathbf{v} = 0 \text{ on } \Gamma_p\}$ and denote with $\|\cdot\|$ the norm it induces. Then, the evolution of (f, m) is given by

$$\begin{cases} \partial_t f = \mathbf{u}_f, \\ \partial_t m = \mu_m, \end{cases} \tag{4.13}$$

where $\mathbf{u}_f$ and μ_m solves the following variational problem

$$(\mathbf{u}_f, \mu_m) = \underset{(\mathbf{v},\nu) \in T_{(f,m)}\mathcal{M}}{\text{argmax}} \left\{ D_{f,m}\mathscr{G}[\mathbf{v}, \nu] - \frac{1}{2}\|(\mathbf{v}, \nu)\|^2 \right\}. \tag{4.14}$$

Finally, the equations in (4.13) are coupled with the mass balance given by Eqs. (4.6)-(4.7).

It is apparent from Eq. (4.14) that, besides the functional $\mathscr{G}$, the choice of the norm $\|\cdot\|$ is essential for determining the evolution for f and m. In addition, notice that $\mathscr{G}$ depends on f only through the domain $\mathcal{B}_t = f(\mathcal{B}, t)$. As a consequence of that, each value of $\mathscr{G}$ can be attained by infinitely many deformations f. The selection of the actual growth map f is determined by the gradient flow, which in turn relies on the choice of the norm $\|\cdot\|$.

Norms and dissipation As seen in Subsection 3.2.4, the choice of the norm is typically dictated by the presence of a dissipation mechanism. Specifically, we could identify the norm of the variations appearing in equation (4.14) with the power dissipated by the evolving system. Denoting by $\mathscr{D}$ such a dissipation, we write

$$\mathscr{D}[\mathbf{v}, \nu] = \|(\mathbf{v}, \nu)\|^2. \tag{4.15}$$

In doing the identification in Eq. (4.15), a subtle but important remark should be made concerning the dimensional consistency of Eq. (4.14). In Subsection 4.2.3, we introduced the gain functional as the net power absorbed by the leaf. Hence, as long as we treat the variations $\mathbf{v}$ and ν as velocities, the term $D_{f,m}\mathscr{G}[\mathbf{v}, \nu]$ appearing in Eq. (4.14) has the dimension of a power per unit time, which is incompatible with the interpretation of $\|\cdot\|$ as a power. This apparent inconsistency can be resolved by invoking the teleological nature of the model. Indeed, the optimality principle underlying our model may be considered as the manifestation of a free energy whose minimizers provide the equilibria of the system, and $-\mathscr{G}(f, m)$ may be acknowledged as the natural candidate for it. In other words, an accurate description of the physics involved in leaf growth would lead to a free energy $\Phi(f, m)$ such that $\Phi = -\mathscr{G}$ for every f and m. Hence, dimensional consistency in Eq. (4.14) is restored once we give to $-\mathscr{G}$ the meaning of free energy.

Such an interpretation also allows to recast problem (4.14) in a form which is strongly reminiscent of the *minimum energy dissipation principle,* first introduced by Onsager [Onsager, 1931, Doi, 2011], namely

$$(\mathbf{u}_f, \mu_m) = \operatorname*{argmin}_{(\mathbf{v},\nu)\in T_{(f,m)}\mathcal{M}} \left\{ D_{f,m}\Phi[\mathbf{v},\nu] + \frac{1}{2}\mathscr{D}[\mathbf{v},\nu] \right\},$$

where Φ is the previously mentioned free energy ($\Phi = -\mathscr{G}$).

Definition of the norms We construct the metric on $T_{(f,m)}\mathcal{M}$ as the sum of the two scalar products $(\cdot,\cdot)_f$ and $(\cdot,\cdot)_m$ for the variations of f and m, respectively. Hence we define

$$((\mathbf{v},\nu),(\mathbf{w},\mu)) = (\mathbf{v},\mathbf{w})_f + (\nu,\mu)_m.$$

In [Lu and Hu, 2022] the authors employ an L^2-gradient flow for the evolution of the conductance field. As anticipated, their model does not account for the evolution of the reference domain, and so there is no ambiguity in deciding to which domain the L^2 norm must refer. On the contrary, in our study we account for the deformation of $\mathcal{B}$ and develop the gradient flow by referring the L^2-norm to the current domain $\mathcal{B}_t$ as the conductance field is naturally spatial. Hence, we define

$$(\nu,\mu)_m = \eta_m(\nu_{\mathsf{s}},\mu_{\mathsf{s}})_{L^2(\mathcal{B}_t)} = \eta_m \int_{\mathcal{B}_t} \nu_{\mathsf{s}}\mu_{\mathsf{s}} = \eta_m \int_{\mathcal{B}} J\nu\mu, \tag{4.16}$$

where η_m is a viscosity-like coefficient.

Concerning the norm for variations of f we propose the following form

$$(\mathbf{v},\mathbf{w})_f = \eta_f \int_{\mathcal{B}_t} \operatorname{grad}(\mathbf{v})\cdot\operatorname{grad}(\mathbf{w}) = \eta_f \int_{\mathcal{B}} J\nabla\mathbf{v}\mathbf{C}^{-1}\cdot\nabla\mathbf{w}, \tag{4.17}$$

where, again, η_f is a viscosity-like coefficient. Here, we recall that $\|\mathbf{v}\|_f^2 = (\mathbf{v},\mathbf{v})_f$ is a norm thanks to the Dirichlet conditions $\mathbf{v} = 0$ on Γ_{p}. Such a norm is reminiscent of viscous dissipation in fluids and its choice is motivated by the visco-plastic nature of plant tissues [Ali et al., 2014] and its simplicity.

Penalty method for the constraint $J > 0$ We observe that equations (4.16) and (4.17) define a scalar product provided that $J > 0$. However, despite being a tacit assumption, there is no guarantee that the set of equations will spontaneously fulfill this condition. Instead of dealing with the difficult task of exactly imposing the unilateral constraint $J > 0$, we adopt a penalty approach by modifying the gain functional as follows

$$\mathscr{G} = \int_{\mathcal{B}} \left[J\left[c_L - \left(c^2 a|\mathbf{F}^{-\mathsf{T}}\nabla p|^2 + \alpha^2|m|^{2\gamma} + \varepsilon|\mathbf{F}^{-\mathsf{T}}\nabla m|^2 \right) \right] - \kappa\zeta(J) \right].$$

In particular we choose ζ as

$$\zeta(J) = \begin{cases} (J-1)^3 & \text{if } J < 1, \\ 0 & \text{if } J \geq 1, \end{cases}$$

such that tissue resorption is penalized through a scalar parameter $\kappa > 0$.

4.2.5   Properties of the solution

The evolution ruled by Eq. (4.13) enjoys the following property directly coming from the gradient flow structure of the equations:

Proposition 4. *The gain is nondecreasing along smooth solutions of (4.13), namely*

$$\frac{\mathrm{d}\mathscr{G}}{\mathrm{d}t} = \|(\partial_t f, \partial_t m)\|^2 \geq 0.$$

Proof. The stationarity of (4.14) reads

$$D_{f,m}\mathscr{G}[\mathbf{v}, \nu] = ((\mathbf{u}_f, \mu_m), (\mathbf{v}, \nu)) \qquad \forall (\mathbf{v}, \nu) \in T_{(f,m)}\mathcal{M}.$$

Hence, we have that

$$\frac{\mathrm{d}\mathscr{G}}{\mathrm{d}t} = D_{f,m}\mathscr{G}[\partial_t f, \partial_t m] = ((\mathbf{u}_f, \mu_m), (\partial_t f, \partial_t m)), \tag{4.18}$$

and substitution of (4.13) into (4.18) leads to

$$\frac{\mathrm{d}\mathscr{G}}{\mathrm{d}t} = D_{f,m}\mathscr{G}[\partial_t f, \partial_t m] = \|(\partial_t f, \partial_t m)\|^2 \geq 0.$$

$\square$

The above Proposition implies that the evolution of the pair (f, m) always points toward (local) maxima of $\mathscr{G}$, whenever they exist. Here, we do not provide a proof of the existence of maxima. However, for the simplified one-dimensional case, we are able to provide an upper bound to $\mathscr{G}$, as stated in the Proposition of Appendix D.2. The estimate of $\mathscr{G}$ that we provide, gives an indication of how light gain and transport cost scale with the length of the leaf ℓ_t. In particular, $\mathscr{L} \sim \ell_t$ while $\mathscr{C} \sim \ell_t^\sigma$, where $\sigma = \frac{3\gamma+1}{1+\gamma}$ and $0 < \gamma < 1$. Hence, $\mathscr{C}$ grows with ℓ_t more rapidly than $\mathscr{L}$ such that there exists a critical length ℓ_t^* beyond which the cost due to an increment in the leaf's length is not compensated by the corresponding revenue in terms of light absorption. While not a rigorous proof, this scaling argument seems to explain the reason why leaves do not growth beyond a certain amount and reach a steady state.

4.2.6   Derivation of the equations

In this subsection we detail the derivation of the gradient flow equations. The stationarity conditions of Eq. (4.14) can be expressed as

$$D_{f,m}\mathscr{G}[\mathbf{v}, \nu] = ((\mathbf{u}_f, \mu_m), (\mathbf{v}, \nu)) \qquad \forall (\mathbf{v}, \nu) \in T_{(f,m)}\mathcal{M}. \tag{4.19}$$

In passing notice that, according to the representation theorem for linear functionals in scalar product spaces (*i.e.* Riesz theorem), equation (4.19) is nothing but the characterization of the functional

gradient of $\mathscr{G}$ with respect to the scalar product $(\cdot, \cdot)$. To make equation (4.19) explicit, let us compute the first variation of $\mathscr{G}$, namely

$$
\begin{aligned}
D_{f,m}\mathscr{G}[\mathbf{v}, \nu] &= \int_{\mathcal{B}} \left(c_L - c^2 a |\mathbf{q}|^2 - \frac{\alpha^2}{\gamma} |m|^{2\gamma} - \varepsilon |\mathbf{F}^{-\mathsf{T}} \nabla m|^2 \right) J \mathbf{F}^{-\mathsf{T}} \cdot \nabla \mathbf{v} + \\
&\quad + \int_{\mathcal{B}} -2 J c^2 a D_f \mathbf{q}[\mathbf{v}] \cdot \mathbf{q} - 2\varepsilon J \mathbf{F}^{-\mathsf{T}} \nabla m \cdot (-\mathbf{F}^{-\mathsf{T}} \nabla \mathbf{v}^{\mathsf{T}} \mathbf{F}^{-\mathsf{T}} \nabla m) \\
&\quad - \int_{\mathcal{B}} J \left(2 c^2 m |q|^2 \nu + 2 c^2 a D_m \mathbf{q}[\nu] \cdot \mathbf{q} + 2\alpha^2 |m|^{2\gamma - 2} m\nu + 2\varepsilon \mathbf{F}^{-\mathsf{T}} \nabla m \cdot \mathbf{F}^{-\mathsf{T}} \nabla \nu \right) \\
&\quad - \int_{\mathcal{B}} J \kappa \zeta'(J) \mathbf{F}^{-\mathsf{T}} \cdot \nabla \mathbf{v},
\end{aligned}
\tag{4.20}
$$

where we defined $\mathbf{q} = \mathbf{F}^{-\mathsf{T}} \nabla p$, which, thanks to the mass balance equation, is treated as a function of f and m. The mathematical structure of the problem allows to get rid of the derivatives $D_f \mathbf{q}[\mathbf{v}]$ and $D_m \mathbf{q}[\mathbf{v}]$, appearing in Eq (4.20), by simply differentiating the mass balance equation (4.8) as follows:

$$
D_{f,m} \left(\int_{\mathcal{B}} J a \mathbf{F}^{-\mathsf{T}} \nabla p \cdot \mathbf{F}^{-\mathsf{T}} \nabla \phi + J e_{\mathrm{w}} \phi \right) [\mathbf{v}, \nu] = 0,
\tag{4.21}
$$

for every $\phi \in V_p$ and for every variation $(f, m) \in T_{(f,m)}\mathcal{M}$. Through an explicit computation, Eq. (4.21) becomes

$$
\begin{aligned}
\int_{\mathcal{B}} (a\mathbf{q} \cdot \mathbf{F}^{-\mathsf{T}} \nabla \phi + e_{\mathrm{w}} \phi) J \mathbf{F}^{-\mathsf{T}} \cdot \nabla \mathbf{v} + J a D_f \mathbf{q}[\mathbf{v}] \cdot \mathbf{F}^{-\mathsf{T}} \nabla \phi + \\
- J a \mathbf{q} \cdot \mathbf{F}^{-\mathsf{T}} \nabla \mathbf{v}^{\mathsf{T}} \mathbf{F}^{-\mathsf{T}} \nabla \phi + 2 J m \mathbf{q} \cdot \mathbf{F}^{-\mathsf{T}} \nabla \phi \nu + J a D_m \mathbf{q}[\nu] \cdot \mathbf{F}^{-\mathsf{T}} \nabla \phi = 0.
\end{aligned}
\tag{4.22}
$$

Now, test Eq. (4.22) with $\phi = p \in V_p$ and obtain

$$
-2c^2 \int_{\mathcal{B}} J a D_f \mathbf{q}[\mathbf{v}] \cdot \mathbf{q} = \int_{\mathcal{B}} (2c^2 a |\mathbf{q}|^2 + 2c^2 e_{\mathrm{w}} p) J \mathbf{F}^{-\mathsf{T}} \cdot \nabla \mathbf{v} - 2c^2 J a (\mathbf{q} \otimes \mathbf{F}^{-1} \mathbf{q}) \cdot \nabla \mathbf{v},
\tag{4.23a}
$$

$$
-2c^2 \int_{\mathcal{B}} J a D_m \mathbf{q}[\nu] \cdot \mathbf{q} = 4c^2 J m |\mathbf{q}|^2 \nu.
\tag{4.23b}
$$

We then observe that the left-hand-side in Eq. (4.23) also appear in Eq. (4.20). Hence substitution of Eq. (4.23) into Eq. (4.20) leads to

$$
D_{f,m}\mathscr{G}[\mathbf{v}, \nu] = -\int_{\mathcal{B}} \mathbf{S}_{\mathrm{a}} \cdot \nabla \mathbf{v} + \int_{\mathcal{B}} J \left(2c^2 m |\mathbf{q}|^2 \nu - 2\alpha^2 |m|^{2\gamma - 2} m\nu - 2\varepsilon \mathbf{F}^{-\mathsf{T}} \nabla m \cdot \mathbf{F}^{-\mathsf{T}} \nabla \nu \right),
\tag{4.24}
$$

where we defined $\mathbf{b} = \mathbf{F}^{-\mathsf{T}} \nabla m$, and

$$
\mathbf{S}_{\mathrm{a}} = -J \left(\iota - 2c^2 a \mathbf{q} \otimes \mathbf{q} + 2\varepsilon \mathbf{b} \otimes \mathbf{b} \right) \mathbf{F}^{-\mathsf{T}},
$$

$$
\iota = c_L + c^2 a |\mathbf{q}|^2 + 2c^2 e_{\mathrm{w}} p - \frac{\alpha^2}{\gamma} |m|^{2\gamma} - \varepsilon |\mathbf{b}|^2 - \kappa \zeta'(J).
$$

By substituting Eq. (4.24) into Eq. (4.19) and integrating by parts we get a set of equations in the unknowns μ_m and $\mathbf{u}_f$. In particular μ_m satisfies

$$\begin{cases} \mu_m = \dfrac{1}{\eta_m}\left\{ 2c^2 m|\mathbf{q}|^2 - 2\alpha^2|m|^{2\gamma-2}m + \dfrac{2\varepsilon}{J}\mathrm{Div}\left(J\mathbf{C}^{-1}\nabla m\right)\right\} & \text{on } \mathcal{B}, \\ J\mathbf{C}^{-1}\nabla m \cdot \mathbf{n} = 0 & \text{on } \Gamma. \end{cases} \tag{4.25}$$

Observe that the boundary conditions in Eq. (4.25), written in the spatial configuration, read $\mathrm{grad}(m)\cdot\mathbf{m} = 0$ on Γ_t. Hence they are standard Neumann Boundary conditions as the ones prescribed in [Lu and Hu, 2022].

As for $\mathbf{u}_f$, we get the following set of equations

$$\begin{cases} \mathrm{Div}\left(\eta_f J\nabla\mathbf{u}_f\mathbf{C}^{-1} + \mathbf{S}_\mathrm{a}\right) = 0 & \text{on } \mathcal{B}, \\ (\eta_f J\nabla\mathbf{u}_f\mathbf{C}^{-1} + \mathbf{S}_\mathrm{a})\mathbf{n} = 0 & \text{on } \Gamma_\mathrm{m}, \\ \mathbf{u}_f = 0 & \text{on } \Gamma_\mathrm{p}. \end{cases} \tag{4.26}$$

Finally, the combination of Eqs (4.26),(4.25) with Eq. (4.13), together with the mass balance in Eqs. (4.6),(4.7), allows to write the complete set of equations ruling the gradient flow evolution. They read

$$\begin{cases} \eta_m\partial_t m = 2c^2 m|\mathbf{q}|^2 - 2\alpha^2|m|^{2\gamma-2}m + \frac{2\varepsilon}{J}\mathrm{Div}\left(J\mathbf{C}^{-1}\nabla m\right) & \text{on } \mathcal{B}, \\ J\mathbf{C}^{-1}\nabla m \cdot \mathbf{n} = 0 & \text{on } \Gamma, \end{cases} \tag{4.27a}$$

$$\begin{cases} \mathrm{Div}\,\mathbf{S} = 0 & \text{on } \mathcal{B}, \\ \mathbf{S} = \mathbf{S}_\mathrm{a} + \eta_f J\dot{\mathbf{F}}\mathbf{C}^{-1} & \text{on } \mathcal{B}, \\ \mathbf{Sn} = 0 & \text{on } \Gamma_\mathrm{m}, \\ f = \mathrm{Id} & \text{on } \Gamma_\mathrm{p}, \end{cases} \tag{4.27b}$$

$$\begin{cases} \mathrm{Div}\left(Ja\mathbf{C}^{-1}\nabla p\right) = Je_\mathrm{w} & \text{on } \mathcal{B}, \\ Ja\mathbf{C}^{-1}\nabla p \cdot \mathbf{n} = 0 & \text{on } \Gamma_\mathrm{m}, \\ p = 0 & \text{on } \Gamma_\mathrm{p}. \end{cases} \tag{4.27c}$$

Concerning the initial conditions, we prescribe

$$m|_{t=0} = m_0, \quad f|_{t=0} = \mathrm{Id}, \quad p|_{t=0} = 0. \tag{4.28}$$

We also report the weak formulation of the equations in (4.27), which can be obtained by simply combining Eq. (4.13) with Eq. (4.19). It reads as follows: find $(f, m) \in \mathcal{M}$ and $p \in V_p$ such that

$$\int_{\mathcal{B}} \eta_m J(\partial_t m)\nu - 2c^2 Jm|\mathbf{q}|^2\nu + \frac{2\alpha^2}{\gamma}J|m|^{2\gamma-2}m\nu + 2\varepsilon J\mathbf{F}^{-\mathsf{T}}\nabla m \cdot \mathbf{F}^{-\mathsf{T}}\nabla\nu = 0, \tag{4.29a}$$

$$\int_{\mathcal{B}} \mathbf{S} \cdot \nabla\mathbf{v} = 0, \tag{4.29b}$$

$$\int_{\mathcal{B}} Ja\mathbf{F}^{-\mathsf{T}}\nabla p \cdot \mathbf{F}^{-\mathsf{T}}\nabla\phi + Je_\mathrm{w}\phi = 0, \tag{4.29c}$$

for every $(\mathbf{v}, \nu) \in T_{(f,m)}\mathcal{M}$ and $\phi \in V_p$.

Non-dimensional equations   In the following, we non-dimensionalize the equations in (4.27) so that to identify the relevant dimensionless groups describing the system. We consider the following list of dimensionless variables

$$X^* = \frac{X}{\ell}, \quad f^* = \frac{f}{\ell}, \quad m^* = \frac{m}{\sqrt{r}}, \quad p^* = \frac{p}{e_w \ell^2 / r} \quad t^* = \frac{t}{\eta_f / c_L}, \quad \mathbf{S}_a^* = \frac{\mathbf{S}_a}{c_L},$$

where ℓ is a characteristic length of $\mathcal{B}$. With this choice, the non-dimensional form of Eqs. (4.27), written in the *current* configuration, reads

$$\begin{cases} \mathsf{N}\partial_t^* m^* = 2\mathsf{C}m^*|\mathrm{grad}^*(p^*)|^2 - 2\mathsf{A}|m^*|^{2\gamma-2}m^* + 2\mathsf{E}\Delta^*(m^*) & \text{on } \mathcal{B}_t^*, \\ \mathrm{grad}^*(m^*) \cdot \mathbf{m} = 0 & \text{on } \Gamma_t^*, \end{cases} \tag{4.30a}$$

$$\begin{cases} \mathrm{div}\,^*\mathbf{T}^* = 0 & \text{on } \mathcal{B}_t^*, \\ \mathbf{T}^* = \mathbf{T}_a^* + \mathrm{grad}^*(\mathbf{u}_f^*) & \text{on } \mathcal{B}_t^*, \\ \mathbf{T}^*\mathbf{m} = 0 & \text{on } \Gamma_m^{t*}, \\ f^* = \mathrm{Id} & \text{on } \Gamma_p^{t*}, \end{cases} \tag{4.30b}$$

$$\begin{cases} \mathrm{div}\,^*(a^*\mathrm{grad}^*(p^*)) = 1 & \text{on } \mathcal{B}_t^*, \\ a^*\mathrm{grad}^*(p^*) \cdot \mathbf{m} = 0 & \text{on } \Gamma_m^{t*}, \\ p^* = 0 & \text{on } \Gamma_p^{t*}, \end{cases} \tag{4.30c}$$

where $a^* = 1+(m^*)^2$, $\mathcal{B}^* = \mathcal{B}/\ell^2$ and Δ^* denotes the (dimensionless) Laplacian operator computed with respect to *spatial* coordinates. Finally, $\mathbf{T}_a^* = \mathbf{S}_a^*\mathbf{F}^\mathsf{T}/J$ is given by

$$\mathbf{T}_a^* = -\iota^*\mathbf{I} + 2\mathsf{C}a^*\mathrm{grad}^*(p^*) \otimes \mathrm{grad}^*(p^*) - 2\mathsf{E}\mathrm{grad}^*(m^*) \otimes \mathrm{grad}^*(m^*), \tag{4.31}$$

$$\iota^* = 1 + \mathsf{C}a^*|\mathrm{grad}^*(p^*)|^2 - 2\mathsf{C}p^* - \frac{\mathsf{A}}{\gamma}|m^*|^{2\gamma} - \mathsf{E}|\mathrm{grad}^*(m^*)|^2 - \mathsf{K}\zeta'(J). \tag{4.32}$$

The dimensionless groups appearing in Eq. (4.30) are defined as follows

$$\mathsf{N} = \frac{r\eta_m}{\eta_f}, \qquad \mathsf{C} = \frac{c^2\ell^2 e_w^2}{c_L r}, \qquad \mathsf{A} = \frac{\alpha^2 r^\gamma}{c_L}, \qquad \mathsf{E} = \frac{\varepsilon r}{\ell^2 c_L}, \qquad \mathsf{K} = \frac{\kappa}{c_L}.$$

Notice that, the equations in (4.30a) are formally identical to the ones derived in [Lu and Hu, 2022]. Indeed we recognize the so called *activation term* $\mathsf{C}m^*|\mathrm{grad}^*(p^*)|^2$, the functional derivative of the *metabolic cost* $\mathsf{A}|m^*|^{2\gamma-2}m^*$ and the diffusion term $\mathsf{E}\Delta^*(m^*)$. The latter, besides acting as a regularizing term, can be interpreted as the effect of *random fluctuations* (Brownian process) in the network structure [Albi et al., 2017]. Moreover, the equations in (4.30b), for the evolution of f, have a structure which is strongly reminiscent of the force balance equations of continua. The symmetric tensor $\mathbf{T}_a^*$ plays the role of an "active stress" balancing the "viscous" forces given by $\mathrm{grad}^*(\mathbf{u}_f^*)$, at least on a mathematical level. In the following, we will loosely speak about active stress when referring to $\mathbf{T}_a^*$. Finally, as already discussed, the term $\zeta'(J)$ is simply introduced as a penalty to prevent the system from evolving toward negative values of J.
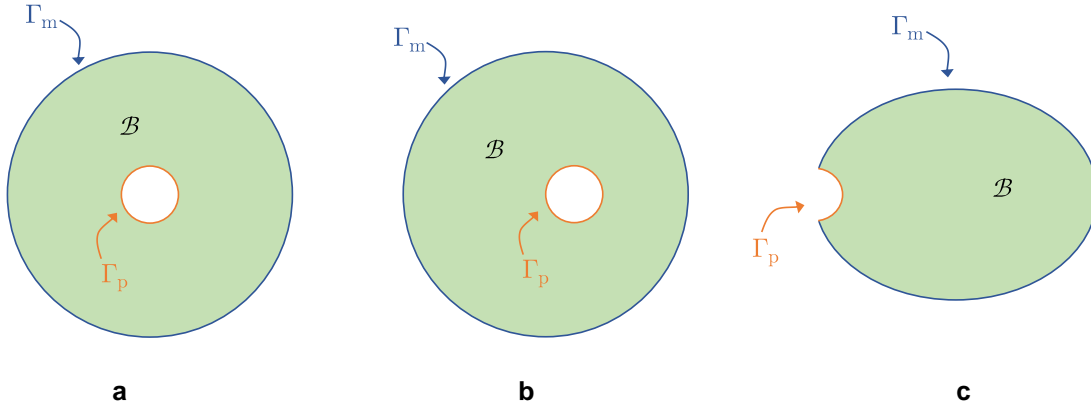
Figure 4.2: Sketch of the reference domains adopted in the numerical simulations. To each domain we associate a reference length ℓ that will later be used to non-dimensionalize the equations. In particular in (a) and (b), ℓ is defined as the radius of the outer circle while in (c) we define ℓ as the major semi-axis of the ellipse.

4.3 Numerical results

In this section we discuss the results coming form the numerical solution of the equations reported in Eqs. 4.29. These were implemented in weak form in the commercial software COMSOL Multiphysics 4.6, and solved by means of the finite element method combined with a backward Euler scheme for time integration.

We first consider the growth of a round leaf whose reference configuration is the annular domain depicted in Fig. 4.2a. Water coming from the roots enters the leaf through the inner circle, namely the boundary Γ_p representing the petiole. Instead, the outer circle Γ_m represents the leaf's margin, which is impermeable and hence endowed with zero flux boundary conditions. As for the initial conditions, we prescribe those reported in Eq. (4.28) with m_0 homogeneous throughout the domain. We let the simulation run until $\mathscr{G}$ reaches a steady state corresponding to the final configuration of the leaf.

In Fig. 4.3 we report a sequence of snapshots at different times showing the evolution of the leaf's shape and of the venation pattern. Interestingly, the leaf grows preserving its circular shape in the early phases, while it develops a lobed margin at equilibrium. The venation pattern, identified by the conductance phase field, visibly divides the leaf into circular sectors delimited by radial strips of very low conductance. In particular, we see that the lobes are distributed so as to subtend each of the circular sectors. We argue that lobes are formed because, at the interface between the circular sectors, growth is not advantageous due to the presence of a very low conductance field. Moreover, a closer look to the shape of the boundary reveals the presence of sub-lobes, *i.e.* minor lobes within the main ones, matching the fractal-like structure of the veins. Remarkably, the equilibrium shape of Fig. 4.3c somehow resembles the lobed leaf reported in Fig. 4.4, which exhibits a similar arrangements of the veins in relation to the positioning of the lobes. Indeed, each lobe is split into halves by a main rib.

As regards the growth pattern, in Fig. 4.5 we report the radial and circumferential stretches.
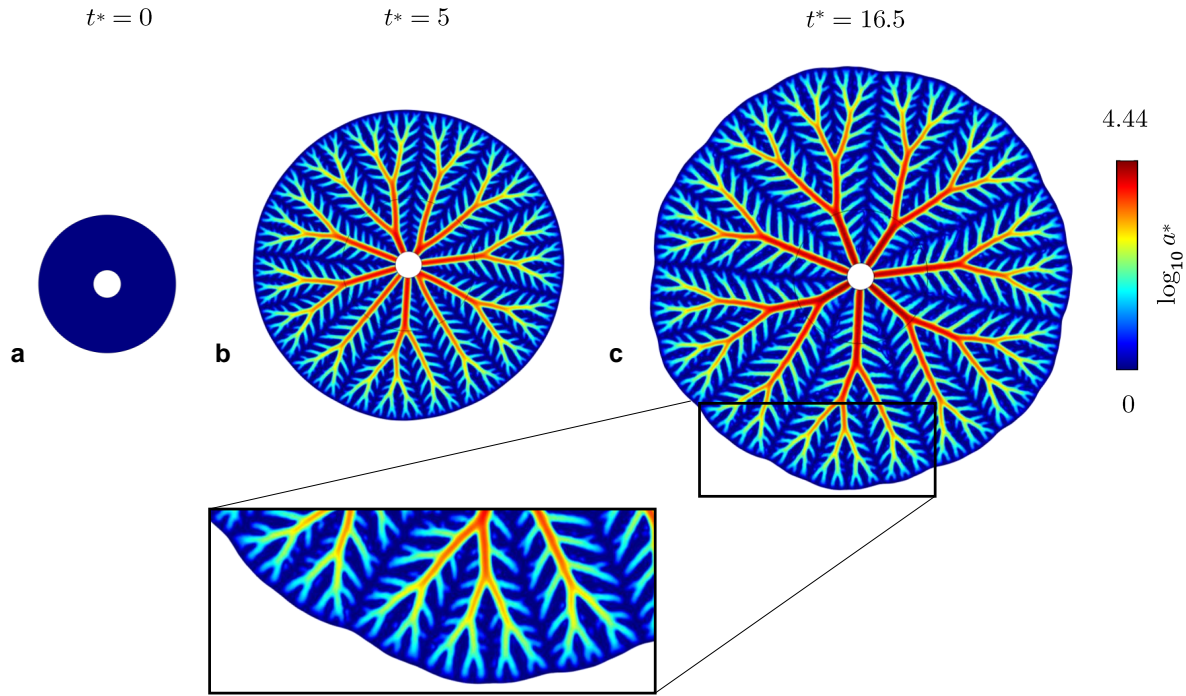
Figure 4.3: Snapshots of the growth of a round leaf with annular reference domain (Fig. 4.2a) at different dimensionless times ($t^* = t/\tau$, with $\tau = \eta_f/c_L$). The time instant $t^* = 16.5$ (c) can be considered as an approximation of the steady state of the system. For each snapshot, we plot the dimensionless conductance field $a^* = a/r$ in logarithmic scale, showing the emergence of a venation pattern. A closer look to the leaf's margin reveals the presence of lobes and sub-lobes arranged in a fractal-like manner. The reference domain is discretized with 24440 triangular elements, and the simulations are performed with the following parameters: $\mathsf{N} = 10^{-5}, \mathsf{C} = 125, \mathsf{A} = 0.0126, \mathsf{E} = 10^{-8}, \mathsf{K} = 2 \times 10^4$. As for the initial conditions we take $m_0^*(X) = m_0(X)/\sqrt{r} = 0.1$.

Figure 4.4: Picture of a sample of Hydrocotyle vulgaris *(also known as the marsh pennywort) exhibiting a round lobed leaf. (Photo taken from the database* Plants of the World Online*).*
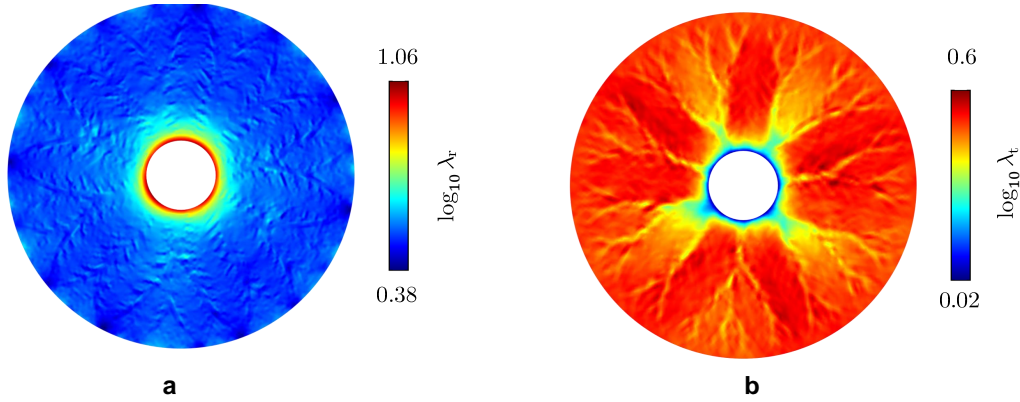
Figure 4.5: Plot of of the radial (a) and circumferential (b) stretches in logarithmic scale, at equilibrium.

In particular, the leaf shows an allometric pattern such that growth is larger in proximity of the petiole, a fact persisting through the entire evolution of the leaf blade. As for the circumferential stretch, we notice that veins deform less than the regions in between them. This trend is even more pronounced during lobes formation. As a measure of growth anisotropy, we report in Fig. 4.6 (the logarithm of) the ratio between the principal stretches, λ_1/λ_2. This quantity attains its maximum near the petiole due to significantly large radial stretch. Apart from that, the other regions feature an anisotropy ratio close to one in the early phases in which the leaf preserves its circular shape, Fig. 4.6a. Instead, during lobes formation, the anisotropy ratio increases in regions occupied by veins, Fig. 4.6b. This aspect is compatible with the experimental measurements reported in [Kierzkowski et al., 2019, Shahaf et al., 2021], where the authors report that growth anisotropy mostly localizes on the main ribs. By filtering out large values of the radial stretch (see Fig. 4.7), we finally observe that lobes formation is achieved by periodically enhancing and inhibiting growth at the leaf margin. Again, this is in qualitative agreement with the measurements in [Kierzkowski et al., 2019]. As regards the driving forces ruling the growth of the leaf's blade, we plot in Fig. 4.8a the principal component of the active stress, $\mathbf{T}_a$, together with streamlines tangent to its line of action. On the regions occupied by veins, the active stress is negative (*contractile*), highly anisotropic, and follows the direction of the veins. On the contrary, the active stress is almost isotropic and positive (*extensile*) throughout the blade. Indeed, on veins, the main contribution to the active stresses is given by the term proportional to $\mathrm{grad}(p) \otimes \mathrm{grad}(p)$ in Eq. (4.31), as confirmed by the plot of the pressure gradient in Fig. 4.8b. There, we see that the pressure gradient is directed as the principal eigenvector of $\mathbf{T}_a$. Instead, the isotropic part regulated by term ι in Eq. (4.32) dominates outside the veins. The final shape of the leaf results form the balance between contractile "forces" in the veins and extensile ones in the blade. We advance the hypothesis that lobes are formed due to an excess of contractile, active stress at their interface.

Next, we extend the study by exploring the case of an annular reference domain with eccentric inner rim, as depicted in Fig. 4.2b. We plot in Fig. 4.9a the leaf configuration at equilibrium. Despite the lack of symmetry of the reference domain, the leaf evolves in order to restore the concentricity of the petiole with respect to the leaf margin, thus leading to a shape that closely matches the one in Fig. 4.3. This behavior may be explained by noticing that, among all the leaves with the same
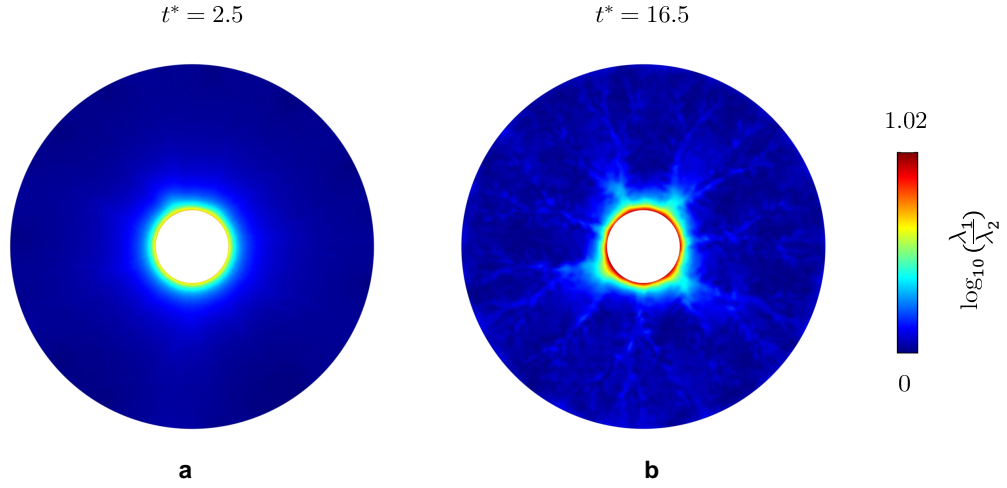
Figure 4.6: Plot of the ratio between the principal stretches λ_1 and λ_2 in logarithmic scale at different dimensionless times $t^* = \eta_f/c_L$.
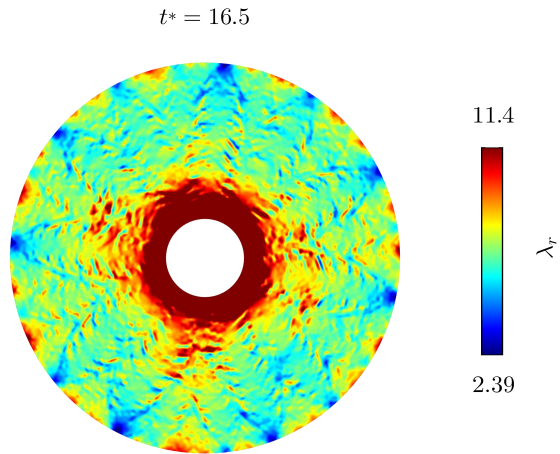

Figure 4.7: Plot of the radial stretch at equilibrium. Values of λ_r higher than 11.4 have been filtered out so that to better appreciate the complex growth pattern.
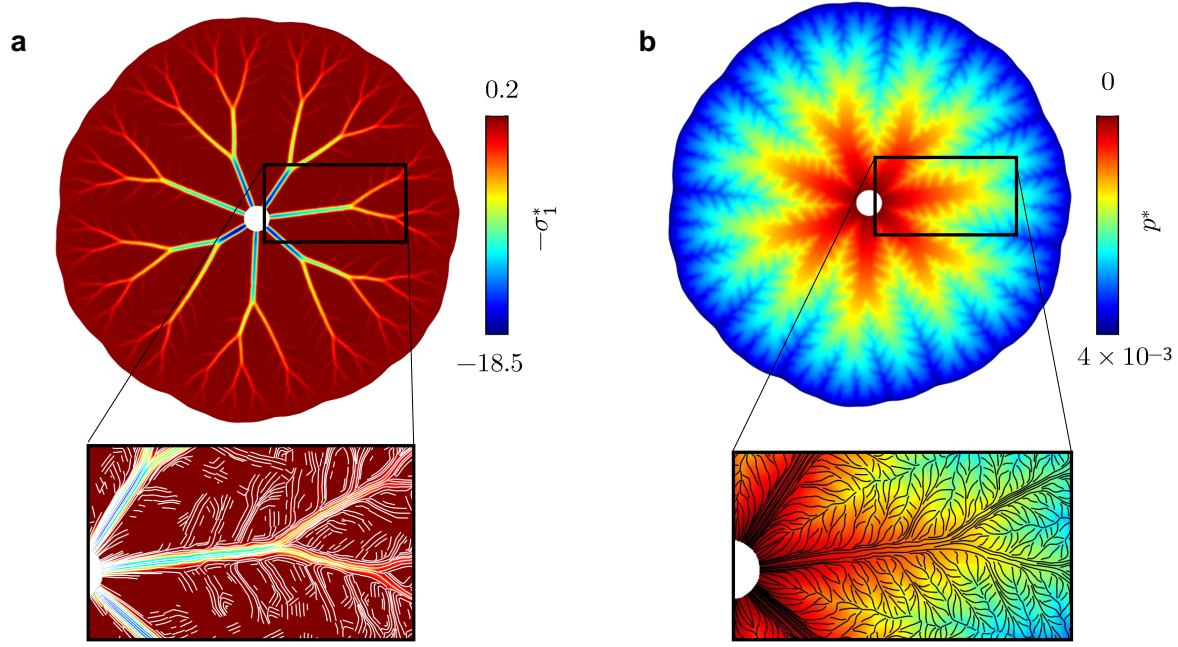
Figure 4.8: (a) Plot of $-\sigma_1^*$, the principal component of $\mathbf{T}_a^*$ at equilibrium together with streamlines tangent to its corresponding eigenvector (inset). (b) Plot of the dimensionless pressure p^* at equilibrium together with streamlines tangent to its corresponding $\mathrm{grad}^*(p^*)$ (inset).
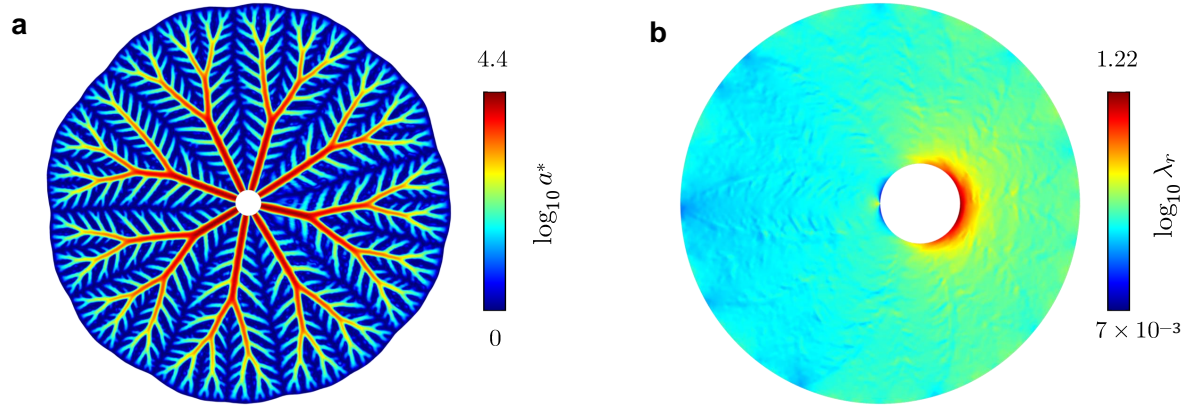

Figure 4.9: Steady state of the growth process starting from the reference domain in Fig. 4.2b. (a) Plot of the dimensionless conductance field $a^* = a/r$ in logarithmic scale. (b) Plot of the radial stretch λ_r in logarithmic scale. The reference domain is discretized with 24458 triangular elements, and the simulations are performed with the following parameters: $\mathsf{N} = 10^{-5}$, $\mathsf{C} = 125$, $\mathsf{A} = 0.0126$, $\mathsf{E} = 10^{-8}$, $\mathsf{K} = 2 \times 10^4$. As for the initial conditions we take $m_0^*(X) = m_0(X)/\sqrt{r} = 0.1$.
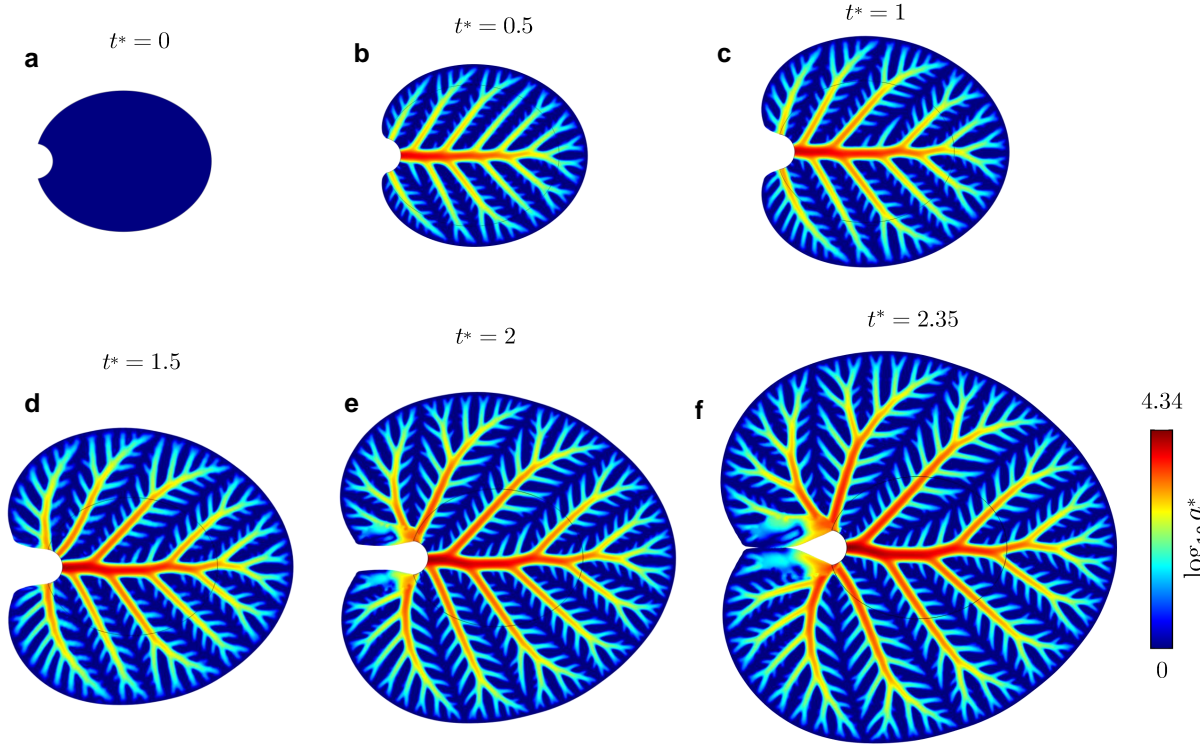
Figure 4.10: Snapshots of the growth of an elliptic leaf starting from the reference domain in Fig. 4.2c at different dimensionless times ($t^* = t/\tau$, with $\tau = \eta_f/c_L$). For each snapshot, we plot the dimensionless conductance field $a^* = a/r$ in logarithmic scale. The reference domain is with 25506 triangular elements, and the simulations are performed with the following parameters: $\mathsf{N} = 10^{-5}$, $\mathsf{C} = 125$, $\mathsf{A} = 0.0126$, $\mathsf{E} = 10^{-8}$, $\mathsf{K} = 2 \times 10^4$. As for the initial conditions we take $m_0^*(X) = m_0(X)/\sqrt{r} = 0.1$.

blade area, the one having a centered petiole minimizes the maximum distance that water has to cover to reach the margin. Because of that, a leaf with circular symmetry may feature a reduced transport cost and thus a greater efficiency. Concerning the growth pattern, in Fig. 4.9 we report the radial stretch. This shows an asymmetric distribution that justifies the evolution toward a leaf with a centered petiole.

Finally, we consider the elliptic reference domain depicted in Fig. 4.2c, resembling a more natural leaf shape. Despite its different topology, the evolution process still tends toward a rounded (*orbicular*) leaf's shape, as shown in Fig. 4.10, where the blade extends backwards with respect to the petiole. The shape reported at the final time in Fig. 4.10 shows some similarities with existing leaves such as the one in Fig. 4.11. Differently from the simulations discussed above, the results reported in Fig. 4.10f do not correspond to a steady state. Indeed, the gradient flow evolution has been stopped as soon as the two rear tails of the leaf touched. Beyond this time, the tails overlap and our model loose its validity since it does not account for leaf's self-interactions. In a real leaf, the two tails would sense the presence of each other and re-adjust their growth accordingly. We hypothesize that the mutual shadowing of the tails could be the reason why leaves do not exhibit large overlapping of the tails. As regards the growth pattern, in Fig. 4.12 we plot the principal stretches along with their direction, noticing some substantial differences with respect to the case

Figure 4.11: Picture of a sample of Viola odorata *exhibiting a heart shaped leaf. (Photo taken from the database* The Bulgarian flora online*)*

reported in Fig. 4.5. In particular, growth exhibits large variations near the petiole: it is almost null near the middle of the petiole and extremely pronounced at its extremities. Moreover, the allometric pattern is inverted if compared to the case in Fig. 4.3, since growth rates at the petiole are smaller than those far from it. Finally, in Fig. 4.13 we report the active stress, showing a interesting difference with respect to that plotted in Fig.4.8. Specifically, the active stress (as well as the pressure gradient) is not always tangential to the veins, as can be appreciated in Fig. 4.13. As detailed in the next Section, the computational results from the last test case reveal some of the limitations of the present model which will be the subject of future developments.
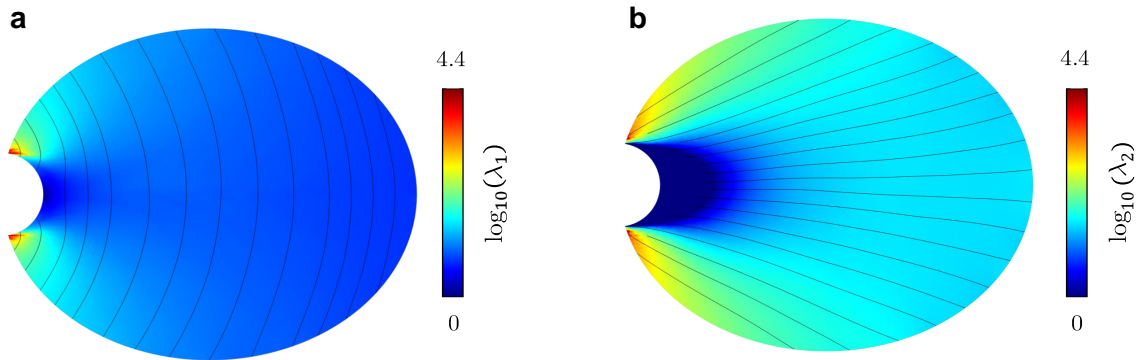

Figure 4.12: Plot of of the principal stretch λ_1 (a) and λ_2 (b) in logarithmic scale at time $t^* = 2.35$.
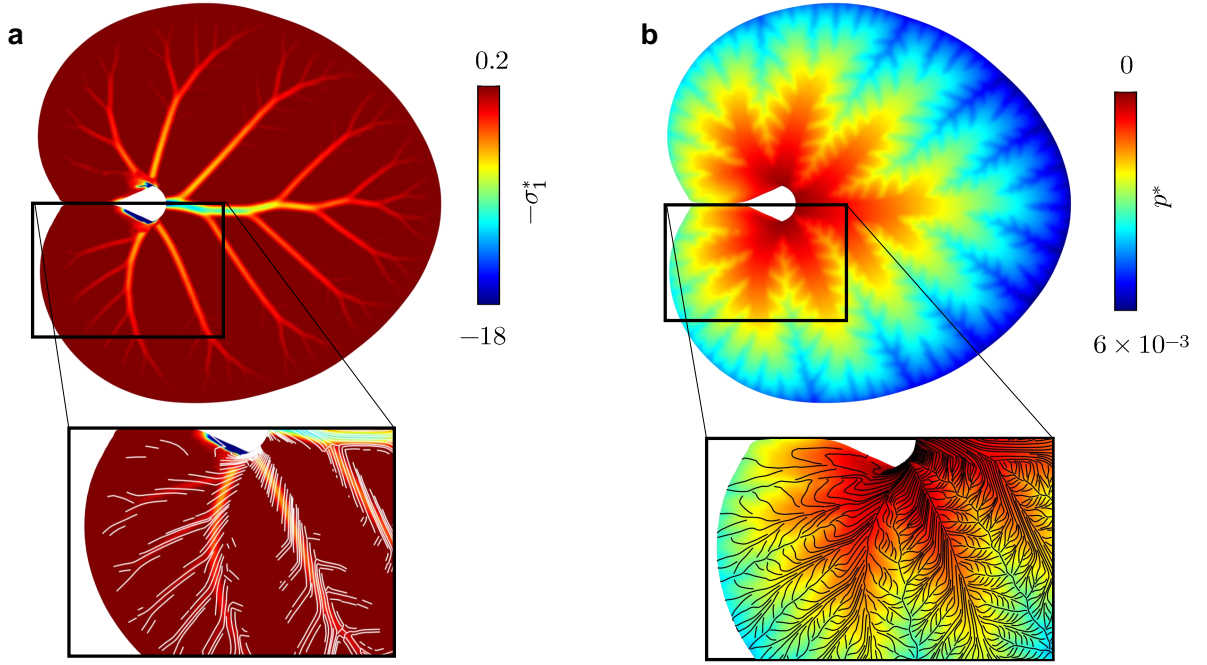
Figure 4.13: (a) Plot of σ_1^*, the principal component of $\mathbf{T}_a^*$ at time $t^* = 2.35$ together with streamlines tangent to its corresponding eigenvector (inset). (b) Plot of the dimensionless pressure p^* at equilibrium together with streamlines tangent to its corresponding $\mathrm{grad}^*(p^*)$ (inset).

4.4 Conclusions

In this Chapter we developed a continuum formulation of the principle exposed in [Xia, 2007] for leaf's growth. In particular, we postulated that leaves evolve according to a gradient flow a functional quantifying the *net* power gained by the leaf due to light absorption. The resulting set of equations have been implemented in a finite element software and tested on reference domains with different topologies showing some qualitative agreement with real leaves.

All the simulations discussed in Section 4.3 feature a growth pattern of the blade leading to round, almost axisymmetric leaf shapes. Therefore, future investigations will point toward a more exhaustive parametric study to explore the range of shapes that the model is able to reproduce. In particular, special attention will be devoted to the role of water evaporation (e_w) and light absorption (c_L). As regards the former, this is prescribed as an external forcing term in the present model. However, it is known that leaves are able to control the rate of evaporation through the opening and closing of stomata to regulate water losses and prevent cavitation phenomena inside the veins. Hence, one may consider extending the model by including a feedback mechanism sensing water pressure for the active control of water evaporation. Moreover, to deal with interactions between separate parts of the leaf the model could be extended to account for the mutual shadowing between such interacting parts, thus regulating overlapping phenomena as those occurring in the test case case of Fig. 4.10. As another step toward a model capable of reproducing a broader range of shapes, we may consider the addition of irreversibility in the evolution of the conductance field. Indeed, as reported in [Laguna et al., 2008], the process of cellular differentiation leading to

vein formations is irreversible. Major developments will be devoted to combine the present model with a mechanical description of the leaf. In fact, as discussed in [Laguna et al., 2008, Ali et al., 2014, al Mosleh and Mahadevan, 2022], mechanical stresses play an important role in feedback regulation mechanisms involved in leaves morphogenesis. Finally, we stress that, among the environmental factors influencing the shape of leaves, our model only consider transport cost and light absorption. Including other aspects like thermal dissipation [Kidner and Umbreen, 2010, Wright et al., 2017], mechanical compliance [Shimoda and Nakata, 2012, Ronellenfitsch, 2021], and stomata regulation [Ding et al., 2020] may lead to a greater variety of shapes.

Bibliography

[Abate and Whitt, 2006] Abate, J. and Whitt, W. (2006). A unified framework for numerically inverting Laplace transforms. *INFORMS Journal on Computing*, 18:408–421.

[Agostiniani et al., 2019] Agostiniani, V., Lucantonio, A., and Lučić, D. (2019). Heterogeneous elastic plates with in-plane modulation of the target curvature and applications to thin gel sheets. *ESAIM: COCV*, 25:24.

[Aharoni et al., 2018] Aharoni, H., Xia, Y., Zhang, X., Kamien, R. D., and Yang, S. (2018). Universal inverse design of surfaces with thin nematic elastomer sheets. *Proceedings of the National Academy of Sciences*, 115(28):7206–7211.

[al Mosleh and Mahadevan, 2022] al Mosleh, S. and Mahadevan, L. (2022). How to grow a flat leaf. *arXiv preprint arXiv:2203.15077*.

[Albi et al., 2016] Albi, G., Artina, M., Foransier, M., and Markowich, P. A. (2016). Biological transportation networks: modeling and simulation. *Analysis and Applications*, 14(01):185–206.

[Albi et al., 2017] Albi, G., Burger, M., Haskovec, J., Markowich, P., and Schlottbom, M. (2017). Continuum modeling of biological network formation. In *Active Particles, Volume 1*, pages 1–48. Springer.

[Ali et al., 2014] Ali, O., Mirabet, V., Godin, C., and Traas, J. (2014). Physical models of plant development. *Annual Review of Cell and Developmental Biology*, 30(1):59–78.

[Alnæs et al., 2015] Alnæs, M., Blechta, J., Hake, J., Johansson, A., Kehlet, B., Logg, A., Richardson, C., Ring, J., Rognes, M. E., and Wells, G. N. (2015). The fenics project version 1.5. *Archive of Numerical Software*, 3(100).

[Alt, 1990] Alt, W. (1990). The lagrange-newton method for infinite-dimensional optimization problems. *Numerical Functional Analysis and Optimization*, 11(3-4):201–224.

[Ambrosi and Guana, 2005] Ambrosi, D. and Guana, F. (2005). Stress-modulated growth. *Mathematics and Mechanics of Solids*, 12(3):319–342.

[Ambrosi and Pezzuto, 2011] Ambrosi, D. and Pezzuto, S. (2011). Active stress vs. active strain in mechanobiology: Constitutive issues. *Journal of Elasticity*, 107(2):199–212.

[Ambulo et al., 2017] Ambulo, C. P., Burroughs, J. J., Boothby, J. M., Kim, H., Shankar, M. R., and Ware, T. H. (2017). Four-dimensional printing of liquid crystal elastomers. *ACS Applied Materials Interfaces*, 9(42):37332–37339.

[Andrini et al., 2020] Andrini, D., Lucantonio, A., and Noselli, G. (2020). A theoretical study on the transient morphing of linear poroelastic plates. *Journal of Applied Mechanics*, 88(3). 031008.

[Armon et al., 2011] Armon, S., Efrati, E., Kupferman, R., and Sharon, E. (2011). Geometry and mechanics in the opening of chiral seed pods. *Science*, 333(6050):1726–1730.

[Arroyo and DeSimone, 2014] Arroyo, M. and DeSimone, A. (2014). Shape control of active surfaces inspired by the movement of euglenids. *Journal of the Mechanics and Physics of Solids*, 62:99–112.

[Bain and Meaney, 2000] Bain, A. C. and Meaney, D. F. (2000). Tissue-level thresholds for axonal damage in an experimental model of central nervous system white matter injury. *Journal of Biomechanical Engineering*, 122(6):615–622.

[Bernal et al., 2007] Bernal, R., Pullarkat, P. A., and Melo, F. (2007). Mechanical properties of axons. *Physical Review Letters*, 99(1):018301.

[Bhatia et al., 2021] Bhatia, N., Runions, A., and Tsiantis, M. (2021). Leaf shape diversity: From genetic modules to computational models. *Annual Review of Plant Biology*, 72:325–356.

[Bilby et al., 1955] Bilby, B. A., Bullough, R., and Smith, E. (1955). Continuous distributions of dislocations: a new application of the methods of non-riemannian geometry. *Proceedings of the Royal Society of London. Series A. Mathematical and Physical Sciences*, 231(1185):263–273.

[Biot, 1941] Biot, M. A. (1941). General theory of three-dimensional consolidation. *Journal of Applied Physics*, 12:155–164.

[Bray, 1984] Bray, D. (1984). Axonal growth in response to experimentally applied mechanical tension. *Developmental Biology*, 102(2):379–389.

[Chada et al., 1997] Chada, S., Lamoureux, P., Buxbaum, R. E., and Heidemann, S. R. (1997). Cytomechanics of neurite outgrowth from chick brain neurons. *Journal of Cell Science*, 110(10):1179–1186.

[Charpiat et al., 2005] Charpiat, G., Faugeras, O., and Keriven, R. (2005). Approximations of shape metrics and application to shape warping and empirical shape statistics. *Foundations of Computational Mathematics*, 5(1):1–58.

[Chester and Anand, 2010] Chester, S. A. and Anand, L. (2010). A coupled theory of fluid permeation and large deformations for elastomeric materials. *Journal of the Mechanics and Physics of Solids*, 58(11):1879–1906.

[Childress, 1981] Childress, S. (1981). *Mechanics of swimming and flying*. Cambridge University Press.

[Christensen and Lo, 1979] Christensen, R. and Lo, K. (1979). Solutions for effective shear properties in three phase sphere and cylinder models. *Journal of the Mechanics and Physics of Solids*, 27(4):315–330.

[Ciarlet et al., 2008] Ciarlet, P. G., Gratie, L., Mardare, C., and Shen, M. (2008). Saint Venant compatibility equations on a surface application to intrinsic shell theory. *Mathematical Models and Methods in Applied Sciences*, 18(02):165–194.

[Cicconofri et al., 2020] Cicconofri, G., Arroyo, M., Noselli, G., and DeSimone, A. (2020). Morphable structures from unicellular organisms with active, shape-shifting envelopes: Variations on a theme by Gauss. *International Journal of Non-Linear Mechanics*, 118(4):103278.

[Coleman and Noll, 1974] Coleman, B. D. and Noll, W. (1974). The thermodynamics of elastic materials with heat conduction and viscosity. In *The Foundations of Mechanics and Thermodynamics*, pages 145–156. Springer Berlin Heidelberg.

[Costa et al., 2018] Costa, A. R., Pinto-Costa, R., Sousa, S. C., and Sousa, M. M. (2018). The regulation of axon diameter: from axonal circumferential contractility to activity-dependent axon swelling. *Frontiers in Molecular Neuroscience*, 11:319.

[Costa et al., 2020] Costa, A. R., Sousa, S. C., Pinto-Costa, R., Mateus, J. C., Lopes, C. D., Costa, A. C., Rosa, D., Machado, D., Pajuelo, L., Wang, X., et al. (2020). The membrane periodic skeleton is an actomyosin network that regulates axonal diameter and conduction. *Elife*, 9:e55471.

[Damioli et al., 2022] Damioli, V., Zorzin, E., DeSimone, A., Noselli, G., and Lucantonio, A. (2022). Transient shape morphing of active gel plates: Geometry and physics. *Soft Matter*.

[Darwin and Darwin, 1896] Darwin, C. and Darwin, F. (1896). *The power of movement in plants*. D. Appleton.

[Das Gupta and Nath, 2015] Das Gupta, M. and Nath, U. (2015). Divergence in patterns of leaf growth polarity is associated with the expression divergence of mir396. *The Plant Cell*, 27(10):2785–2799.

[Datar et al., 2019] Datar, A., Ameeramja, J., Bhat, A., Srivastava, R., Mishra, A., Bernal, R., Prost, J., Callan-Jones, A., and Pullarkat, P. A. (2019). The roles of microtubules and membrane tension in axonal beading, retraction, and atrophy. *Biophysical Journal*, 117(5):880–891.

[Dehghany et al., 2020] Dehghany, M., Naghdabadi, R., Sohrabpour, S., Li, Y., and Hu, Y. (2020). A thermodynamically consistent electro-chemo-mechanical theory for modeling axonal swelling. *Journal of the Mechanics and Physics of Solids*, 145:104113.

[Delfour and Zolésio, 2011] Delfour, M. C. and Zolésio, J.-P. (2011). *Shapes and geometries: Metrics, analysis, differential calculus, and optimization*. SIAM.

[Dennerll et al., 1989] Dennerll, T. J., Lamoureux, P., Buxbaum, R. E., and Heidemann, S. R. (1989). The cytomechanics of axonal elongation and retraction. *Journal of Cell Biology*, 109(6):3073–3083.

[DiCarlo and Quiligotti, 2002] DiCarlo, A. and Quiligotti, S. (2002). Growth and balance. *Mechanics Research Communications*, 29(6):449–456.

[Ding et al., 2020] Ding, J., Johnson, E. A., and Martin, Y. E. (2020). Optimization of leaf morphology in relation to leaf water status: A theory. *Ecology and evolution*, 10(3):1510–1525.

[Dobyns et al., 1993] Dobyns, W. B., Reiner, O., Carrozzo, R., and Ledbetter, D. H. (1993). Lissencephaly: a human brain malformation associated with deletion of the lis1 gene located at chromosome 17p13. *Jama*, 270(23):2838–2842.

[Doi, 2009] Doi, M. (2009). Gel dynamics. *Journal of the Physical Society of Japan*, 78(5):052001.

[Doi, 2011] Doi, M. (2011). Onsager's variational principle in soft matter. *Journal of Physics: Condensed Matter*, 23(28):284118.

[Efrati et al., 2009] Efrati, E., Sharon, E., and Kupferman, R. (2009). Elastic theory of unconstrained non-euclidean plates. *Journal of the Mechanics and Physics of Solids*, 57(4):762–775.

[Efrati et al., 2013] Efrati, E., Sharon, E., and Kupferman, R. (2013). The metric description of elasticity in residually stressed soft materials. *Soft Matter*, 9(34):8187–8197.

[Epstein, 2015] Epstein, M. (2015). Mathematical characterization and identification of remodeling, growth, aging and morphogenesis. *Journal of the Mechanics and Physics of Solids*, 84:72–84.

[Facca, 2016] Facca, E. (2016). *Biologically inspired formulation of Optimal Transport Problems*. PhD thesis, Università degli Studi di Padova.

[Facca et al., 2018] Facca, E., Cardin, F., and Putti, M. (2018). Towards a stationary monge–kantorovich dynamics: The physarum polycephalum experience. *SIAM Journal on Applied Mathematics*, 78(2):651–676.

[Facca et al., 2021] Facca, E., Cardin, F., and Putti, M. (2021). Branching structures emerging from a continuous optimal transport model. *Journal of Computational Physics*, 447:110700.

[Fan et al., 2017] Fan, A., Tofangchi, A., Kandel, M., Popescu, G., and Saif, T. (2017). Coupled circumferential and axial tension driven by actin and myosin influences in vivo axon diameter. *Scientific Reports*, 7(1).

[Ford et al., 2019] Ford, M. J., Ambulo, C. P., Kent, T. A., Markvicka, E. J., Pan, C., Malen, J., Ware, T. H., and Majidi, C. (2019). A multifunctional shape-morphing elastomer with liquid metal inclusions. *Proceedings of the National Academy of Sciences*, 116(43):21438–21444.

[Fuchs et al., 2009] Fuchs, M., Jüttler, B., Scherzer, O., and Yang, H. (2009). Shape metrics based on elastic deformations. *Journal of Mathematical Imaging and Vision*, 35(1):86–102.

[García-Grajales et al., 2017] García-Grajales, J. A., Jérusalem, A., and Goriely, A. (2017). Continuum mechanical modeling of axonal growth. *Computer Methods in Applied Mechanics and Engineering*, 314:147–163.

[Giantesio et al., 2018] Giantesio, G., Musesti, A., and Riccobelli, D. (2018). A comparison between active strain and active stress in transversely isotropic hyperelastic materials. *Journal of Elasticity*, 137(1):63–82.

[Gill et al., 2005] Gill, P. E., Murray, W., and Saunders, M. A. (2005). Snopt: An SQP algorithm for large-scale constrained optimization. *SIAM Review*, 47(1):99–131.

[Goriely, 2017] Goriely, A. (2017). *The Mathematics and Mechanics of Biological Growth*. Springer New York.

[Goriely and Ben Amar, 2005] Goriely, A. and Ben Amar, M. (2005). Differential growth and instability in elastic shells. *Physical Review Letters*, 94:198103.

[Gray, 1953] Gray, J. (1953). *How animals move*. Cambridge University Press.

[Günnel and Herzog, 2016] Günnel, A. and Herzog, R. (2016). Optimal control problems in finite-strain elasticity by inner pressure and fiber tension. *Frontiers in Applied Mathematics and Statistics*, 2:4.

[Gurtin, 1982] Gurtin, M. E. (1982). *An introduction to continuum mechanics*. Academic press.

[Gurtin et al., 2010] Gurtin, M. E., Fried, E., and Anand, L. (2010). *The mechanics and thermodynamics of continua*. Cambridge University Press.

[Guseinov et al., 2020] Guseinov, R., McMahan, C., PÃ©rez, J., Daraio, C., and Bickel, B. (2020). Programming temporal morphing of self-actuated shells. *Nature Communications*, 11(1):1–7.

[Haskovec et al., 2015] Haskovec, J., Markowich, P., and Perthame, B. (2015). Mathematical analysis of a pde system for biological network formation. *Communications in Partial Differential Equations*, 40(5):918–956.

[Hong et al., 2008] Hong, W., Zhao, X., Zhou, J., and Suo, Z. (2008). A theory of coupled diffusion and large deformation in polymeric gels. *Journal of the Mechanics and Physics of Solids*, 56(5):1779–1793.

[Hu and Cai, 2013] Hu, D. and Cai, D. (2013). Adaptation and optimization of biological transport networks. *Physical review letters*, 111(13):138701.

[Jacomy et al., 2006] Jacomy, H., Fragoso, G., Almazan, G., Mushynski, W. E., and Talbot, P. J. (2006). Human coronavirus OC43 infection induces chronic encephalitis leading to disabilities in BALB/c mice. *Virology*, 349(2):335–346.

[Jeon et al., 2017] Jeon, S.-J., Hauser, A. W., and Hayward, R. C. (2017). Shape-morphing materials from stimuli-responsive hydrogel hybrids. *Accounts of Chemical Research*, 50(2):161–169.

[Kidner and Umbreen, 2010] Kidner, C. A. and Umbreen, S. (2010). Why is leaf shape so variable. *International Journal of Plant Developmental Biology*, 4(1):64–75.

[Kierzkowski et al., 2019] Kierzkowski, D., Runions, A., Vuolo, F., Strauss, S., Lymbouridou, R., Routier-Kierzkowska, A.-L., Wilson-Sánchez, D., Jenke, H., Galinha, C., Mosca, G., et al. (2019). A growth-based framework for leaf shape development and diversity. *Cell*, 177(6):1405–1418.

[Klein et al., 2007] Klein, Y., Efrati, E., and Sharon, E. (2007). Shaping of elastic sheets by prescription of non-Euclidean metrics. *Science*, 315(5815):1116–1120.

[Kondaurov and Nikitin, 1987] Kondaurov, V. and Nikitin, L. (1987). Finite strains of viscoelastic muscle tissue. *Journal of Applied Mathematics and Mechanics*, 51(3):346–353.

[Kröner, 1959] Kröner, E. (1959). Allgemeine kontinuumstheorie der versetzungen und eigenspannungen. *Archive for Rational Mechanics and Analysis*, 4(1):273–334.

[Kuchen et al., 2012] Kuchen, E. E., Fox, S., Barbier de Reuille, P., Kennaway, R., Bensmihen, S., Avondo, J., Calder, G. M., Southam, P., Robinson, S., Bangham, A., et al. (2012). Generation of leaf shape through early patterns of growth and tissue polarity. *Science*, 335(6072):1092–1096.

[Laguna et al., 2008] Laguna, M. F., Bohn, S., and Jagla, E. A. (2008). The role of elastic stresses on leaf venation morphogenesis. *PLoS computational biology*, 4(4):e1000055.

[Lang et al., 2017] Lang, G. E., Waters, S. L., Vella, D., and Goriely, A. (2017). Axonal buckling following stretch injury. *Journal of Elasticity*, 129(1):239–256.

[Lee, 1969] Lee, E. H. (1969). Elastic-plastic deformation at finite strains.

[Leronni and Bardella, 2021] Leronni, A. and Bardella, L. (2021). Modeling actuation and sensing in ionic polymer metal composites by electrochemo-poromechanics. *Journal of the Mechanics and Physics of Solids*, 148:104292.

[Liewald et al., 2014] Liewald, D., Miller, R., Logothetis, N., Wagner, H.-J., and SchÃŒz, A. (2014). Distribution of axon diameters in cortical white matter: an electron-microscopic study on three human brains and a macaque. *Biological Cybernetics*, 108(5):541–557.

[Liu et al., 2021] Liu, K., Hacker, F., and Daraio, C. (2021). Robotic surfaces with reversible, spatiotemporal control for shape morphing and object manipulation. *Science Robotics*, 6(53):eabf5116.

[Lu and Hu, 2022] Lu, Y. and Hu, D. (2022). Optimisation of biological transport networks. *East Asian Journal on Applied Mathematics*, 12(1):72–95.

[Lucantonio and DeSimone, 2020] Lucantonio, A. and DeSimone, A. (2020). Computational design of shape-programmable gel plates. *Mechanics of Materials*, 144:103313.

[Lucantonio and Nardinocchi, 2012] Lucantonio, A. and Nardinocchi, P. (2012). Reduced models of swelling-induced bending of gel bars. *International Journal of Solids and Structures*, 49(11-12):1399–1405.

[Lucantonio et al., 2013] Lucantonio, A., Nardinocchi, P., and Teresi, L. (2013). Transient analysis of swelling-induced large deformations in polymer gels. *Journal of the Mechanics and Physics of Solids*, 61(1):205–218.

[Marciniak-Czochra and Mikelić, 2015] Marciniak-Czochra, A. and Mikelić, A. (2015). A rigorous derivation of the equations for the clamped biot-kirchhoff-love poroelastic plate. *Archive for Rational Mechanics and Analysis*, 215(3):1035–1062.

[Miara, 1994] Miara, B. (1994). Justification of the asymptotic analysis of elastic plates, I. the linear case. *Asymptotic analysis*, 9(1):47–60.

[Miehe et al., 2015] Miehe, C., Mauthe, S., and Teichtmeister, S. (2015). Minimization principles for the coupled problem of darcy–biot-type fluid transport in porous media linked to phase field modeling of fracture. *Journal of the Mechanics and Physics of Solids*, 82:186–217.

[Murray, 1926] Murray, C. D. (1926). The physiological principle of minimum work: I. the vascular system and the cost of blood volume. *Proceedings of the National Academy of Sciences*, 12(3):207–214.

[Nardinocchi and Teresi, 2007] Nardinocchi, P. and Teresi, L. (2007). On the active response of soft living tissues. *Journal of Elasticity*, 88(1):27–39.

[Nardinocchi et al., 2013] Nardinocchi, P., Teresi, L., and Varano, V. (2013). The elastic metric: A review of elasticity with large distortions. *International Journal of Non-Linear Mechanics*, 56:34–42.

[Nehari, 1952] Nehari, Z. (1952). *Conformal mapping*. McGraw-Hill, New York.

[Nikić et al., 2011] Nikić, I., Merkler, D., Sorbara, C., Brinkoetter, M., Kreutzfeldt, M., Bareyre, F. M., Brück, W., Bishop, D., Misgeld, T., and Kerschensteiner, M. (2011). A reversible form of axon damage in experimental autoimmune encephalomyelitis and multiple sclerosis. *Nature Medicine*, 17(4):495–499.

[Nojoomi et al., 2018] Nojoomi, A., Arslan, H., Lee, K., and Yum, K. (2018). Bioinspired 3d structures with programmable morphologies and motions. *Nature Communications*, 9(1):3705.

[Noselli et al., 2019] Noselli, G., Beran, A., Arroyo, M., and DeSimone, A. (2019). Swimming Euglena respond to confinement with a behavioural change enabling effective crawling. *Nature Physics*, 15:496–502.

[Ogden, 1997] Ogden, R. W. (1997). *Non-linear elastic deformations*. Courier Corporation.

[Oliveri and Goriely, 2022] Oliveri, H. and Goriely, A. (2022). Mathematical models of neuronal growth. *Biomechanics and Modeling in Mechanobiology*, pages 1–30.

[Onsager, 1931] Onsager, L. (1931). Reciprocal relations in irreversible processes. i. *Physical review*, 37(4):405.

[Ortigosa et al., 2021] Ortigosa, R., Martinez Frutos, J., Mora Corral, C., Pedregal, P., and Periago, F. (2021). Optimal control of soft materials using a Hausdorff distance functional. *SIAM Journal on Control and Optimization*, 59(1):393–416.

[Otto, 2001] Otto, F. (2001). The geometry of dissipative evolution equations: the porous medium equation.

[Oudet and Santambrogio, 2011] Oudet, E. and Santambrogio, F. (2011). A modica-mortola approximation for branched transport and applications. *Archive for rational mechanics and analysis*, 201(1):115–142.

[Ouyang et al., 2013] Ouyang, H., Nauman, E., and Shi, R. (2013). Contribution of cytoskeletal elements to the axonal mechanical properties. *Journal of Biological Engineering*, 7(1).

[Paroni and Tomassetti, 2018] Paroni, R. and Tomassetti, G. (2018). Linear models for thin plates of polymer gels. *Mathematics and Mechanics of Solids*, 23(5):835–862.

[Pezzulla et al., 2018] Pezzulla, M., Stoop, N., Steranka, M. P., Bade, A. J., and Holmes, D. P. (2018). Curvature-induced instabilities of shells. *Physical Review Letters*, 120:048002.

[Podio-Guidugli, 2019] Podio-Guidugli, P. (2019). *Continuum Thermodynamics*. Springer.

[Riccobelli, 2021] Riccobelli, D. (2021). Active elasticity drives the formation of periodic beading in damaged axons. *Physical Review E*, 104(2).

[Riccobelli and Ambrosi, 2019] Riccobelli, D. and Ambrosi, D. (2019). Activation of a muscle as a mapping of stress–strain curves. *Extreme Mechanics Letters*, 28:37–42.

[Riccobelli and Bevilacqua, 2020] Riccobelli, D. and Bevilacqua, G. (2020). Surface tension controls the onset of gyrification in brain organoids. *Journal of the Mechanics and Physics of Solids*, 134:103745.

[Riccobelli et al., 2020] Riccobelli, D., Noselli, G., Arroyo, M., and DeSimone, A. (2020). Mechanics of axisymmetric sheets of interlocking and slidable rods. *Journal of the Mechanics and Physics of Solid*, 141:103969.

[Ronellenfitsch, 2021] Ronellenfitsch, H. (2021). Optimal elasticity of biological networks. *Physical Review Letters*, 126(3):038101.

[Rotsch and Radmacher, 2000] Rotsch, C. and Radmacher, M. (2000). Drug-induced changes of cytoskeletal structure and mechanics in fibroblasts: An atomic force microscopy study. *Biophysical Journal*, 78(1):520–535.

[Sack and Scoffoni, 2013] Sack, L. and Scoffoni, C. (2013). Leaf venation: structure, function, development, evolution, ecology and applications in the past, present and future. *New phytologist*, 198(4):983–1000.

[Sareh et al., 2013] Sareh, S., Rossiter, J., Conn, A., Drescher, K., and Goldstein, R. E. (2013). Swimming like algae: Biomimetic soft artificial cilia. *Journal of The Royal Society Interface*, 10(78):20120666.

[Sawa et al., 2010] Sawa, Y., Urayama, K., Takigawa, T., DeSimone, A., and Teresi, L. (2010). Thermally driven giant bending of liquid crystal elastomer films with hybrid alignment. *Macromolecules*, 43(9):4362–4369.

[Shahaf et al., 2021] Shahaf, A., Moshe, M., and Eran, S. (2021). The multiscale nature of leaf growth fields. *Communications Physics*, 4(1).

[Sharon and Efrati, 2010] Sharon, E. and Efrati, E. (2010). The mechanics of non-euclidean plates. *Soft Matter*, 6(22):5693–5704.

[Shimoda and Nakata, 2012] Shimoda, M. and Nakata, Y. (2012). Application of shape optimization method to artificial leaf design. *Design and Nature VI: Comparing Design in Nature with Science and Engineering*, 4:157.

[Stålhand et al., 2011] Stålhand, J., Klarbring, A., and Holzapfel, G. (2011). A mechanochemical 3d continuum model for smooth muscle contraction under finite strains. *Journal of Theoretical Biology*, 268(1):120–130.

[Stokin et al., 2005] Stokin, G. B., Lillo, C., Falzone, T. L., Brusch, R. G., Rockenstein, E., Mount, S. L., Raman, R., Davies, P., Masliah, E., Williams, D. S., et al. (2005). Axonopathy and transport deficits early in the pathogenesis of alzheimer's disease. *Science*.

[Taber, 1992] Taber, L. A. (1992). A theory for transverse deflection of poroelastic plates. *Journal of Applied Mechanics*, 59(3):628–634.

[Taber and Perucchio, 2000] Taber, L. A. and Perucchio, R. (2000). Modeling heart development. *Journal of Elasticity and the Physical Science of Solids*, 61(1):165–197.

[Tagliaferro and Burke, 2016] Tagliaferro, P. and Burke, R. E. (2016). Retrograde axonal degeneration in parkinson disease. *Journal of Parkinson's disease*, 6(1):1–15.

[Tanaka and Fillmore, 1979] Tanaka, T. and Fillmore, D. J. (1979). Kinetics of swelling of gels. *The Journal of Chemical Physics*, 70(3):1214–1218.

[Tang-Schomer et al., 2009] Tang-Schomer, M. D., Patel, A. R., Baas, P. W., and Smith, D. H. (2009). Mechanical breaking of microtubules in axons during dynamic stretch injury underlies delayed elasticity, microtubule disassembly, and axon degeneration. *The FASEB Journal*, 24(5):1401–1410.

[Timoshenko et al., 1959] Timoshenko, S., Woinowsky-Krieger, S., et al. (1959). *Theory of plates and shells*, volume 2. McGraw-hill New York.

[Tomassetti, 2022] Tomassetti, G. (2022). Modeling the diffusion of a fluid in a strained solid: a comparison between different formats. *Applications in Engineering Science*, 9:100079.

[Tosi, 2018] Tosi, R. (2018). Numerical solution of the three dimensional optimal transport problem.

[Truesdell and Noll, 1965] Truesdell, C. and Noll, W. (1965). The non-linear field theories of mechanics. *Handbuch der Physik*, 2:1–541.

[van Rees et al., 2017] van Rees, W. M., Vouga, E., and Mahadevan, L. (2017). Growth patterns for shape-shifting elastic bilayers. *Proceedings of the National Academy of Sciences*, 114(44):11597–11602.

[Warner and Terentjev, 2003] Warner, M. and Terentjev, E. M. (2003). *Liquid crystal elastomers*. Oxford University Press.

[Wright et al., 2017] Wright, I. J., Dong, N., Maire, V., Prentice, I. C., Westoby, M., Díaz, S., Gallagher, R. V., Jacobs, B. F., Kooyman, R., Law, E. A., et al. (2017). Global climatic drivers of leaf size. *Science*, 357(6354):917–921.

[Xia, 2003] Xia, Q. (2003). Optimal paths related to transport problems. *Communications in Contemporary Mathematics*, 5(02):251–279.

[Xia, 2007] Xia, Q. (2007). The formation of a tree leaf. *ESAIM: Control, Optimisation and Calculus of Variations*, 13(2):359–377.

[Xia, 2015] Xia, Q. (2015). Motivations, ideas and applications of ramified optimal transportation. *ESAIM: Mathematical Modelling and Numerical Analysis*, 49(6):1791–1832.

[Xu et al., 2013] Xu, K., Zhong, G., and Zhuang, X. (2013). Actin, spectrin, and associated proteins form a periodic cytoskeletal structure in axons. *Science*, 339(6118):452–456.

[Yamaue and Doi, 2004] Yamaue, T. and Doi, M. (2004). Theory of one-dimensional swelling dynamics of polymer gels under mechanical constraint. *Physical Review E*, 69:041402.

[Zhang et al., 2017] Zhang, Y., Abiraman, K., Li, H., Pierce, D. M., Tzingounis, A. V., and Lykotrafitis, G. (2017). Modeling of the axon membrane skeleton structure and implications for its mechanical properties. *PLOS Computational Biology*, 13(2):e1005407.

[Zheng et al., 1991] Zheng, J., Lamoureux, P., Santiago, V., Dennerll, T., Buxbaum, R. E., and Heidemann, S. R. (1991). Tensile regulation of axonal elongation and initiation. *Journal of Neuroscience*, 11(4):1117–1125.

Appendix A

Method of solution for the poroelastic plate equations

We follow the approach of [Taber, 1992] to solve for the poroelastic plate equations and assume step loading as specified in Section 1.5. As for the governing equation (1.65), we formally identify its RHS with a forcing term $\mathscr{F} = 2\left(\mathrm{tr}\mathbf{E} + \varepsilon\, x_3 \mathrm{tr}\mathbf{K}\right)$ and write

$$\partial_t \mu - \partial_{33}\mu = -\partial_t \mathscr{F}\,. \tag{A.1}$$

Then, we seek a solution to Eq. (A.1) in the form

$$\mu(\mathbf{x}, x_3, t) = \mu_s(\mathbf{x}, x_3) + \sum_{n=1}^{\infty} A_n(\mathbf{x}, t)\phi_n(x_3), \tag{A.2}$$

where $\mu_s(\mathbf{x}, x_3) = \bar{\mu}_m(\mathbf{x}) + 2\bar{\mu}_d(\mathbf{x})x_3$ is the steady-state solution, $\phi_n(x_3) = \sin[\lambda_n(x_3 + 1/2)]$ are the eigenfunctions of the pure diffusion equation corresponding to the eigenvalues $\lambda_n = n\pi$, and where

$$A_n = c_n G_n + \int_0^t G_n(t - \tau)\partial_t a_n \mathrm{d}\tau\,, \tag{A.3a}$$

$$G_n = e^{-\lambda_n^2 t}\,, \quad a_n = -2\int_{-\frac{1}{2}}^{\frac{1}{2}} (\mathscr{F} + \mu_s)\, \phi_n \mathrm{d}x_3\,. \tag{A.3b}$$

Observe that imposition of the initial condition $\mu = 0$ implies

$$c_n = -2\int_{-\frac{1}{2}}^{\frac{1}{2}} \mu_s \phi_n \mathrm{d}x_3 = \begin{cases} \bar{\mu}_d/(n\pi) & n \text{ even}\,, \\ -\bar{\mu}_m/(n\pi) & n \text{ odd}\,. \end{cases} \tag{A.4}$$

We proceed by taking the Laplace transform of Eq. (A.2) and by computing the thickness resultants N_μ and M_μ according to their definitions as

$$\hat{N}_\mu = \frac{\bar{\mu}_m}{s} - \mathcal{A}\,\mathrm{tr}\hat{\mathbf{E}} + \mathcal{D}\,, \qquad\qquad \hat{M}_\mu = \frac{\bar{\mu}_d}{6s} - \mathcal{C}\,\mathrm{tr}\hat{\mathbf{K}} + \mathcal{E}\,, \tag{A.5}$$

where $\mathcal{A}, \mathcal{C}, \mathcal{D}, \mathcal{E}$ are defined in Table $A.1$. Combination of Eq. (A.5) with the Laplace transforms of Eq. (1.63) and substitution into the Eq. (1.62) yields a problem for the displacement ($\hat{\mathbf{u}}$, $\hat{u}_3$), along with the mechanical boundary conditions.

$$\mathcal{A} = \frac{16s}{\pi^2} \sum_{n=1}^{\infty} \frac{\hat{G}_{2n-1}}{(2n-1)^2} \qquad \mathcal{C} = \frac{s}{\pi^2} \sum_{n=1}^{\infty} \frac{\hat{G}_{2n}}{n^2}$$

$$\mathcal{D} = \frac{2}{\pi} \sum_{n=1}^{\infty} \frac{c_{2n-1}\hat{G}_{2n-1}}{2n-1} \qquad \mathcal{E} = -\frac{1}{2\pi} \sum_{n=1}^{\infty} \frac{c_{2n}\hat{G}_{2n}}{n}$$

Table A.1: Expressions for the functions $\mathcal{A}, \mathcal{C}, \mathcal{D}, \mathcal{E}$

In the stress-free case, transformation of Eq. (A.2) accounting for Eq. (1.74) allows to express $\hat{\mu}$ as in Eq. (1.76) with

$$\hat{\nu}_e(x_3, s) = \frac{1}{s} - \left(1 + \frac{16\eta}{3 + 2\eta} s\hat{N}_{\mu,e}\right) \sum_{n=1}^{\infty} \frac{1}{(2n-1)\pi} \phi_{2n-1}\hat{G}_{2n-1} , \qquad \text{(A.6a)}$$

$$\hat{\nu}_o(x_3, s) = \frac{2x_3}{s} + \left(1 + \frac{96\eta}{3 + 2\eta} s\hat{M}_{\mu,o}\right) \sum_{n=1}^{\infty} \frac{1}{2n\pi} \phi_{2n}\hat{G}_{2n} . \qquad \text{(A.6b)}$$

Finally, Eq. (A.5) along with Eq. (1.74) allow to compute $\hat{N}_{\mu,e}$ and $\hat{M}_{\mu,o}$ as

$$\hat{N}_{\mu,e} = \frac{3 + 2\eta}{3 + 2\eta + 2\eta\mathcal{A}} \left(\frac{1}{s} + \mathcal{D}\right), \qquad \text{(A.7a)}$$

$$\hat{M}_{\mu,o} = \frac{3 + 2\eta}{(3 + 2\eta) + 24\eta\mathcal{C}} \left(\frac{1}{6s} + \mathcal{E}\right). \qquad \text{(A.7b)}$$

Appendix B

Optimal shape design in the space of compatible metrics

Let us consider the following variational problem

$$\min_{f \in M} \mathcal{C}(\mathbf{C}) \,, \tag{B.1}$$

where $M = \{f \in V : d_H(f(\Gamma), \bar{\Gamma}) = 0\}$. To derive the stationarity conditions of the complexity functional $\mathcal{C}$, we compute its Gâteaux derivative:

$$D_f \mathcal{C}[\mathbf{v}] = D_{\mathbf{C}} \mathcal{C}[\nabla \mathbf{v}^\mathsf{T} \mathbf{F} + \mathbf{F}^\mathsf{T} \nabla \mathbf{v}] = \frac{1}{|\omega|} \int_\omega 2\mathbf{F} \, \nabla_{\mathbf{C}} \mathcal{C} \cdot \nabla \mathbf{v} + \frac{1}{|\omega|} \int_\Gamma 2\mathbf{F} \, \mathbf{N} \cdot \nabla \mathbf{v} = 0 \,, \quad \forall \, \mathbf{v} \in T_f M \,, \tag{B.2}$$

where we recall that $\nabla_{\mathbf{C}} \mathcal{C} = \partial_{\mathbf{G}} \chi - \mathrm{Div} \, (\partial_\Xi \chi) \in \mathrm{Sym}_2$ and $\mathbf{N} = \partial_\Xi \chi[\mathbf{n}] \in \mathrm{Sym}_2$. Upon introducing the definitions of $\mathbf{A} := -2\mathbf{F} \, \nabla_{\mathbf{C}} \mathcal{C}$ and $\mathbf{B} := 2\mathbf{F} \, \mathbf{N}$, the equation above can be recast into

$$\int_\omega \mathrm{Div} \, \mathbf{A} \cdot \mathbf{v} - \int_\Gamma (\mathbf{An} \cdot \mathbf{v} - \mathbf{Bn} \cdot \partial_\mathbf{n} \mathbf{v} + \partial_\mathbf{t}(\mathbf{Bt}) \cdot \mathbf{v}) = 0 \,, \quad \forall \, \mathbf{v} \in T_f M \,, \tag{B.3}$$

where $\mathbf{n}$ and $\mathbf{t}$ denote the outward normal and the tangent unit vectors to Γ, respectively. Notice that equation (B.3) is equivalent to

$$\int_\omega \mathrm{Div} \, \mathbf{A} \cdot \mathbf{v} = 0 \,, \quad \forall \, \mathbf{v} \in C_c^\infty(\omega) \subseteq T_f M \,, \tag{B.4}$$

such that

$$\mathrm{Div} \, \mathbf{A} = \mathbf{0} \quad \text{in } \omega \,. \tag{B.5}$$

Then, equation (B.3) becomes

$$\int_\Gamma (\mathbf{An} + \partial_\mathbf{t}(\mathbf{Bt})) \cdot \mathbf{v} - \mathbf{Bn} \cdot \partial_\mathbf{n} \mathbf{v} = 0 \,, \quad \forall \, \mathbf{v} \in T_f M \,, \tag{B.6}$$

which, upon localization, leads to

$$\mathbf{PAn} + \mathbf{P} \partial_\mathbf{t}(\mathbf{Bt}) = \mathbf{0} \,, \quad \mathbf{Bn} = \mathbf{0} \quad \text{on } \Gamma \,, \tag{B.7}$$

where we have exploited the arbitrariness of $\mathbf{v}$ and $\partial_{\mathbf{n}}\mathbf{v}$, and used the representation $\mathbf{v}|_{\Gamma} = \mathbf{Pa}$ for some $\mathbf{a} \in V_{\Gamma}$.

Finally, consider the affine deformation of homogeneous gradient $\mathbf{F}$ sending Γ into $\bar{\Gamma}$ exactly. Since $\mathbf{A}$ is homogeneous and $\mathbf{B} = \mathbf{0}$, equation (B.5) and the second of equations (B.7) are trivially satisfied, whereas the first of equations (B.7) provides again condition (2.18). Hence, the result of Proposition 3 applies literally also in the stress-free context.

Appendix C

Monoparametric active stretch

In the following, we discuss the case of a single active stretch parameter, where the tensor $\mathbf{F}_a$ is given by (3.48). In such a case, the balance equations (3.2) for the remodelling stresses reduce to a single equation, namely $B = C$. Writing the Clausius-Duhem inequality

$$\int_{\mathcal{P}} \dot{\psi} \leq \int_{\mathcal{P}} \mathbf{S} \cdot \dot{\mathbf{F}} + 2 \int_{\mathcal{P} \cap \Omega_{0c}} C \frac{\dot{a}}{a},$$

and performing analogous computations to those in Section 3.2, we find

$$\begin{cases} \mathbf{S} = \partial_{\mathbf{F}_e} \psi_0 \, \mathbf{F}_a^{-\mathsf{T}} - p \mathbf{F}^{-\mathsf{T}}, \\ 2C = \mu_c \tau \dfrac{\dot{a}}{a} - \mathbf{M} \cdot \widehat{\mathbf{I}} + \Gamma, \end{cases} \tag{C.1}$$

where

$$\widehat{\mathbf{I}} = \mathbf{e}_\Theta \otimes \mathbf{e}_\Theta + \mathbf{e}_Z \otimes \mathbf{e}_Z - 2\mathbf{e}_R \otimes \mathbf{e}_R,$$

and Γ is the reactive term enforcing the unilateral constraint $a \leq 1$. Similarly to (3.18), the evolution equation for the active stretch reads

$$\dot{a} = \begin{cases} \dfrac{1}{\mu_c \tau} \left(2B + \mathbf{M} \cdot \widehat{\mathbf{I}} \right) a, & \text{if } a < 1 \text{ or } 2B < -\mathbf{M} \cdot \widehat{\mathbf{I}}, \\ 0, & \text{otherwise.} \end{cases} \tag{C.2}$$

Under the kinematic assumption (3.34), the differential equation (C.2) admits an equilibrium $\bar{a}$. Indeed we have an equilibrium solution with $\bar{a} < 1$ if

$$\varphi(a) = 2\mu_c a^6 - 2B\lambda a^2 - \mu_c \left(\lambda^3 + 1 \right) = 0. \tag{C.3}$$

Since $\varphi(0) < 0$, $\varphi'(a) > 0$ for $B \leq 0$, and $\varphi(a) \to +\infty$ as $a \to +\infty$, there exists one and only one $\bar{a} > 0$ such that $\varphi(\bar{a}) = 0$. Such a root is acceptable if $\bar{a} < 1$, and this holds whenever $\varphi(1) > 0$. It is straightforward to prove the asymptotic stability of $\bar{a}$. Otherwise, if $\varphi(1) \leq 0$, then $2B + \mathbf{M} \cdot \widehat{\mathbf{I}}$ is non-negative for $a = 1$ and the equilibrium solution is $\bar{a} = 1$.

To compute the stress components, we need to explicitly obtain the expression for p. Setting $a_\Theta = a_Z = a$ in (3.35) − (3.36), we get

$$p(r) = \widehat{k}_1, \qquad\qquad\qquad 0 \leq r < r_i,$$

$$p(r) = \widehat{k}_2 + \frac{(a^6 - 1)\mu_c \log(r)}{\lambda a^2}, \qquad\qquad r_i \leq r < r_o.$$

Enforcing the boundary and the interface conditions, (3.30) and (3.6) respectively, we find the two constants

$$\widehat{k}_1 = \frac{\mu_{\mathrm{a}}}{\lambda} + \frac{\mu_{\mathrm{c}}}{\lambda} \frac{\left(a^6 - 1\right)\left[\log(r_{\mathrm{i}}) - \log(r_{\mathrm{o}})\right]}{a^2},$$

and

$$\widehat{k}_2 = \frac{\mu_{\mathrm{c}}\left(a^6 + \log(r_{\mathrm{o}}) - a^6 \log(r_{\mathrm{o}})\right)}{\lambda a^2}.$$

Appendix D

Complements to Chapter 4

D.1 The gradient flow in the Euclidean space

Let us consider $\mathbb{R}^n$, endowed with the standard Euclidean scalar product, and a function

$$f : \mathbb{R}^n \to \mathbb{R}$$
$$\mathbf{x} \mapsto f(\mathbf{x}).$$

We define the gradient flow of f in the variable $\mathbf{x}$ as

$$\dot{\mathbf{x}}(t) = -\nabla f(\mathbf{x}(t)).$$

The symbol ∇f denotes the gradient of f and is defined as the unique vector field satisfying

$$D_{\mathbf{x}} f(\mathbf{x})[\mathbf{v}] = \nabla f(\mathbf{x}) \cdot \mathbf{v} \quad \forall \mathbf{v} \in \mathbb{R}^n, \tag{D.1}$$

where $D_{\mathbf{x}} f$ denotes the differential of f. Observe that, as apparent from Eq. (D.1), the definition of ∇f depends on the choice of the scalar product: a scalar product different from the Euclidean one induces a different notion of gradient, and hence a different evolution for $\mathbf{x}(t)$.

It is easy to see that f is always non-increasing along the trajectories $\mathbf{x}(t)$, indeed

$$\frac{\mathrm{d}}{\mathrm{d}t} f(\mathbf{x}(t)) = D_{\mathbf{x}} f(\mathbf{x})[\dot{\mathbf{x}}] = \nabla f(\mathbf{x}(t)) \cdot \dot{\mathbf{x}} = -|\nabla f(\mathbf{x}(t))|^2 \le 0.$$

This implies that the gradient flow always points toward a local minimum point of f.

Gradient flows can also be characterized through the following variational problem:

$$\dot{\mathbf{x}}(t) = \mathbf{v}(\mathbf{x}(t)),$$

where

$$\mathbf{v}(\mathbf{x}) = \underset{\mathbf{v}}{\operatorname{argmin}} \left\{ D_{\mathbf{x}} f(\mathbf{x})[\mathbf{v}] + \frac{1}{2} |\mathbf{v}|^2 \right\}. \tag{D.2}$$

This fact can be easily shown by exploiting Eq. (D.1). The role of the scalar product (and consequently of the norm it induces) becomes even more explicit when looking at the variational characterization in Eq. (D.2). We finally remark that gradient flows evolving toward maximum

point, can be easily constructed by defining the evolution law $\dot{\mathbf{x}}(t) = \mathbf{v}(\mathbf{x}(t))$ with $\mathbf{v}$ solving the variational problem

$$\mathbf{v}(\mathbf{x}) = \underset{\mathbf{v}}{\mathrm{argmax}} \left\{ D_{\mathbf{x}} f(\mathbf{x})[\mathbf{v}] - \frac{1}{2} |\mathbf{v}|^2 \right\}. \tag{D.3}$$

The theory of gradient flows, as presented here, can be *formally* extended to the infinite dimensional setting where the function f is substituted by a functional, defined on a scalar product space of functions (see [Otto, 2001]). In Chapter 4, we are interested in a maximization problem and hence, in a gradient flow characterized by a variational problem completely analogous to Eq. (D.3).

D.2 Upper bound for $\mathscr{G}$ in the one-dimensional case

The one-dimensional counterpart of the problem introduced in Section 4.2 describes the growth of an interval $\mathcal{I} = [0, \ell]$ according to a growth map $f : \mathcal{I} \to \mathbb{R}$ sending the reference configuration $\mathcal{I}$ into the actual one denoted by $\mathcal{I}_t = [0, \ell_t]$. The derivation of the 1D equations follows from straightforward substitution of two-dimensional operators with two-dimensional ones. For the purposes of this section we simply report the definition of the gain functional and of state an integral version of the mass balance equation. The form simply reads as follows

$$\mathscr{G} = \mathscr{L} - \mathscr{C} = \int_{\mathcal{I}_t} \left(c_L - c^2 (r + m^2) |p'|^2 - \frac{\alpha^2}{\gamma} |m|^{2\gamma} - \varepsilon |m'|^2 \right), \tag{D.4}$$

where the primes denote differentiation with respect to the spatial coordinate x. As regards the mass balance, it reads

$$h(x) - h(y) = \int_{\mathcal{I}_t} e_{\mathrm{w}} \qquad \forall x, y \in \mathcal{I}_t \text{ with } x < y, \tag{D.5}$$

where h is the mass flux which as usual we model through a Fick's law given by $h = -ap'$ with $a = r + m^2$.

It is then possible to prove the following upper bound for the gain functional

Proposition 5. *For every $0 < \gamma < 1$, there exist two positive constants A and B such that*

$$\mathscr{G}(\ell_t, m) \leq A\ell_t - B\ell_t^\sigma,$$

for every m and ℓ_t, and for $\sigma = \frac{3\gamma + 1}{1 + \gamma}$. In particular $\mathscr{G}(\ell_t, m) < +\infty$ for every m and ℓ_t.

Proof. Let $a > 0$ and let $\delta := 2\gamma/(1+\gamma)$. Then, thanks to Young inequality with conjugate exponents q and q', we obtain

$$|aw|^\delta = \frac{1}{\alpha^{\frac{\delta}{\gamma}} c^\delta} |\alpha^{\frac{1}{\gamma}} a^{\frac{1}{2}}|^\delta |ca^{\frac{1}{2}} w|^\delta \overset{\text{Young ineq.}}{\leq} \frac{1}{C_{\alpha,c}} \left(\alpha^{\frac{\delta q'}{\gamma}} \frac{a^{\frac{\delta q'}{2}}}{q'} + c^{\delta q} \frac{a^{\frac{\delta q}{2}} |w|^{\delta q}}{q} \right) \quad \forall w \in \mathbb{R}. \tag{D.6}$$

Now let us choose $q = 2/\delta$ (and consequently $q' = \frac{2}{2-\delta}$) then inequality in Eq. (D.6) becomes

$$\frac{2}{\delta} C_{\alpha,c} |aw|^\delta \leq \frac{\alpha^2}{\gamma} a^\gamma + c^2 a |w|^2, \tag{D.7}$$

where $C_{\alpha,c} = (c\alpha^{\frac{1}{\gamma}})^\delta$. Now, since $1 < \gamma < 0$ we can exploit the sub-additivity of $g(u) = u^\gamma$ and write

$$\frac{2}{\delta}C_{\alpha,c}|aw|^\delta \leq C_{r,\gamma,\alpha} + \frac{\alpha^2}{\gamma}|m|^{2\gamma} + c^2a|w|^2, \tag{D.8}$$

where $C_{r,\gamma,\alpha} = \frac{\alpha^2}{\gamma}r^\gamma$. So, thanks to Eq. (D.8) and recalling the definition of transport cost in Eq. (D.4) we have that

$$\int_{\mathcal{I}_t}\left(\frac{2}{\delta}C_{\alpha,c}|h(x)|^\delta - C_{r,\gamma,\alpha}\right)\mathrm{d}x = \int_{\mathcal{I}_t}\left(\frac{2}{\delta}C_{\alpha,c}|ap'(x)|^\delta - C_{r,\gamma,\alpha}\right)\mathrm{d}x \leq$$

$$\leq \int_{\mathcal{I}_t}\left(\frac{\alpha^2}{\gamma}|m(x)|^{2\gamma} + c^2a|p'(x)|^2\right)\mathrm{d}x \leq \int_{\mathcal{I}_t}\left(\frac{\alpha^2}{\gamma}|m(x)|^{2\gamma} + c^2a|p'(x)|^2 + \varepsilon|m'(x)|^2\right)\mathrm{d}x = \mathscr{C}. \tag{D.9}$$

Moreover, from the mass balance in Eq. (D.5) that

$$h(0) - h(x) = e_\mathrm{w}x \quad \forall x \in [0, \ell_t].$$

In particular, since $h(\ell_t) = 0$ we have $h(0) = e_\mathrm{w}\ell_t$ and so we deduce

$$h(x) = e_\mathrm{w}(\ell_t - x). \tag{D.10}$$

Consequently, we have

$$\int_{\mathcal{I}_t}|h|^\delta = e_\mathrm{w}^\delta\int_{\mathcal{I}_t}|\ell_t - x|^\delta = \frac{e_\mathrm{w}^\delta}{\delta+1}\ell_t^{\delta+1}.$$

So combining Eq. (D.9) with Eq. (D.10) we get

$$\mathscr{C} \geq \int_{\mathcal{I}_t}\left(\frac{2}{\delta}C_{\alpha,c}|h|^\delta - C_{r,\gamma,\alpha}\right) = 2C_{\alpha,c}\frac{e_\mathrm{w}^\delta}{\delta(\delta+1)}\ell_t^{\delta+1} - C_{r,\gamma,\alpha}\ell_t. \tag{D.11}$$

Finally, exploiting the definition of $\mathscr{G}$ and Eq. (D.11) we get

$$\mathscr{G} \leq (c_L + C_{r,\gamma,\alpha})\ell_t - 2C_{\alpha,c}\frac{e_\mathrm{w}^\delta}{\delta(\delta+1)}\ell_t^{\delta+1} = \beta(\ell_t).$$

Let us now search for the maximum of β by imposing

$$\frac{\mathrm{d}\beta}{\mathrm{d}\ell} = (c_L + C_{r,\gamma,\alpha}) - \frac{2}{\delta}C_{\alpha,c}e_\mathrm{w}^\delta\ell_t^\delta = 0.$$

If $\delta > 0$ then $\beta(\ell_t)$ has a maximum for

$$\ell_t^* = \frac{1}{e_\mathrm{w}}\left(\frac{c_L + C_{r,\gamma,\alpha}}{\frac{2}{\delta}C_{\alpha,c}}\right)^{\frac{1}{\delta}},$$

and so $\mathscr{G}(\ell_t, m) \leq \beta(\ell_t^*) < +\infty$ for every ℓ_t and m. $\qquad\square$